Advanced Instrumentation and Flux Mapping Techniques for the Study of the Space Environment

by

Jason A. Gilbert

A dissertation submitted in partial fulfillment
of the requirements for the degree of
Doctor of Philosophy
(Atmospheric and Space Sciences)
in The University of Michigan
2008

Doctoral Committee:

Professor Thomas H. Zurbuchen, Chair
Professor Lennard A. Fisk
Professor George Gloeckler
Professor Timothy A. McKay
Associate Professor Aaron J. Ridley

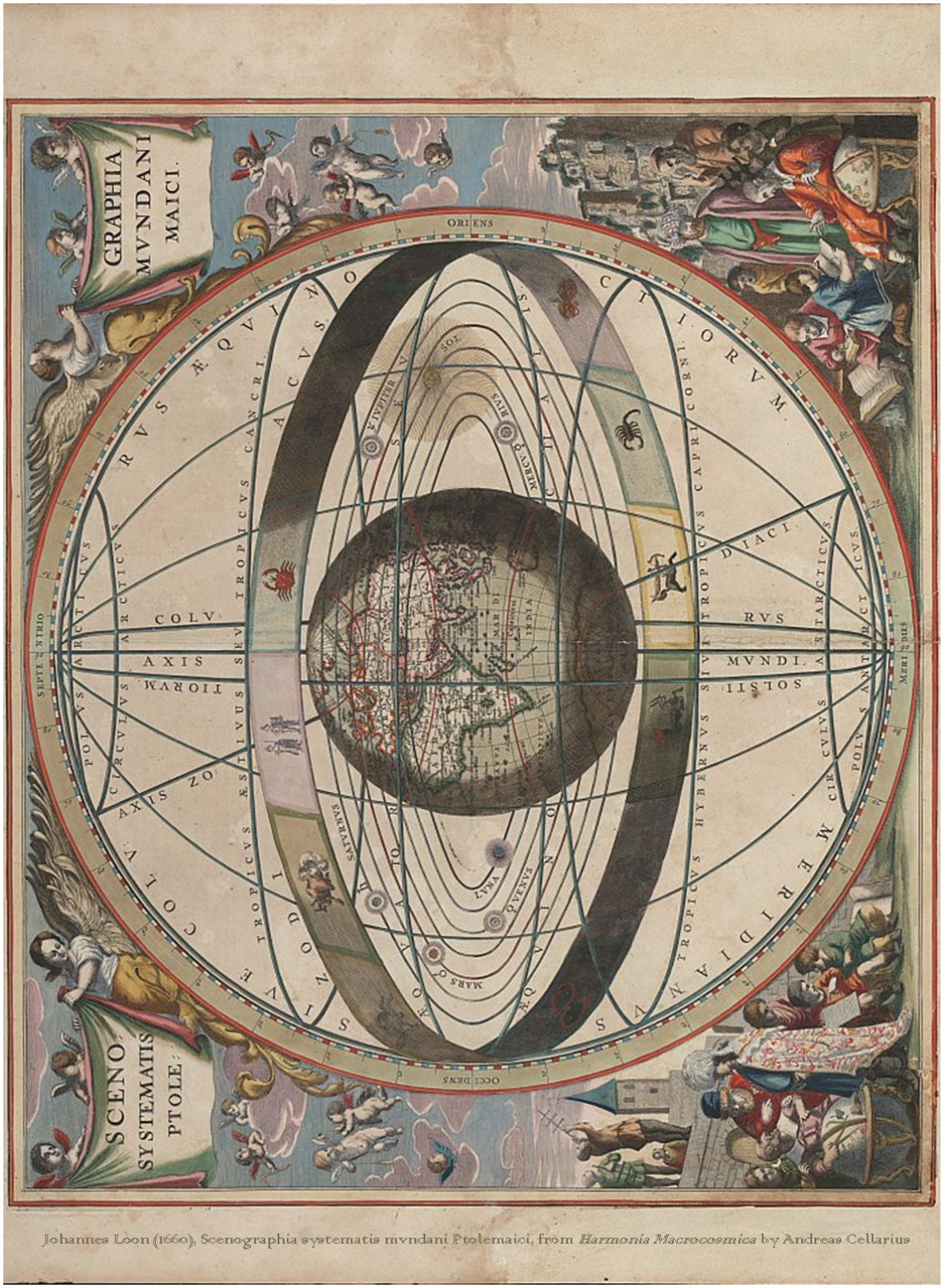

Johannes Loon (1660), Scenographia systematis mvndani Ptolemaici, from *Harmonia Macrocosmica* by Andreas Cellarius

To all the people

ACKNOWLEDGEMENTS

Gratitude is due to my lovely wife Victoria, who motivated me through all the tough times and gave me unwaivering support, and my children, whose smiling faces were always there to greet me, even when lab work kept me away until the early hours of the morning.

Thanks to Aaron Ridley, K. C. Hansen, and Jim Raines for assistance with field line tracing and other such programming challenges, Philip Roe and Bram van Leer for their advice on computational numerical techniques, and C. Nick Arge of the Air Force Research Laboratory/Space Vehicles Directorate and Sarah McGregor of Boston University for providing potential-field source-surface model data derived from the Mount Wilson Solar Observatory.

Thanks to all who helped out with the development of IonSpec. George Gloeckler for the concept and advice. Kara Vargo for contributing to the development of the IonSpec analytical model and analysis code, as well as her masterful 3D modeling of the entire vacuum chamber. Chuck Navarre for machining the instrument to exact specifications, and the students over the years who have offered help with CAD or simulations.

The experiments in the laboratory would not have been possible if not for the help of Bob Lundgren, and the workload was made a little lighter when I could share it with lab colleagues Matt Panning and Dan Gershman. Steve Rogacki who helped with the necessary lab electronics, and Mike Long who was there to build cables or what ever else was needed at a moment's notice. Thanks to all.

I thank the members of my dissertation committee for their feedback and constructive advice on how to make this dissertation better — Thomas Zurbuchen, Len Fisk, George Gloeckler, Tim McKay, and Aaron Ridley. I am especially grateful for the many discussions with Len and Thomas concerning whatever esoteric piece of the science we were interested in that week.

I also thank the National Aeronautics and Space Administration, who supported this research under grants NNG05GN09H and NNG04GJ66G, and by the Targeted Research and Technology (TR&T) program.

But most of all, I need to thank the Lord, who helped me get through impossible situations and unrealistic deadlines while still keeping my sanity intact. Mostly.

TABLE OF CONTENTS

LIST OF FIGURES

Figure

LIST OF TABLES

Table

LIST OF APPENDICES

Appendix

LIST OF ABBREVIATIONS

ACE Advanced Composition Explorer

ACR anomalous cosmic ray

AMPTE Active Magnetospheric Particle Tracer Explorers

AU Astronomical Unit

CAD computer-aided design

CAPS Cassini Plasma Spectrometer

CCE Charge Composition Explorer

CELIAS Charge, Element, and Isotope Analysis System

CEM channel electron multiplier

CHEM Charge-Energy-Mass

CHEMS Charge-Energy-Mass Spectrometer

CIR corotating interaction region

CME coronal mass ejection

CR Carrington rotation

CCMC Community Coordinated Modeling Center

ELS Electron Spectrometer

ESA electrostatic analyzer

FIP first ionization potential

FIPS Fast Imaging Plasma Spectrometer

FPGA field-programmable gate array

FWHM full width at half maximum

GCR galactic cosmic ray

HCS heliospheric current sheet

ICE International Cometary Explorer

IMS Ion Mass Spectrometer

IRM Ion Release Module

LEF linear-electric-field

MASS High Mass Resolution Spectrometer

MCP microchannel plate

MESSENGER Mercury: Surface, Space Environment, Geochemistry, Ranging

MHD magnetohydrodynamic

MTOF Mass Time-of-Flight

PATH Particle Acceleration in the Turbulent Heliosphere

PEPE Plasma Experiment for Planetary Exploration

PFSS potential field source surface

PICSPEC Pickup Ion Composition Spectrometer

SEP solar energetic particle

SOHO Solar and Heliospheric Observatory

SSD solid-state detector

SEPICA Solar Energetic Particle Ionic Charge Analyzer

STICS Suprathermal Ion Composition Spectrometer

SULEICA Suprathermal Energy Ionic Charge Analyzer

SWICS Solar Wind Ion Composition Spectrometer

TOF time-of-flight

ULECA Ultra-Low-Energy Charge Analyzer

UV ultraviolet

WSA Wang-Sheeley-Arge

ABSTRACT

Advanced Instrumentation and Flux Mapping Techniques for the Study of the Space Environment

by

Jason A. Gilbert

Chair: Thomas H. Zurbuchen

The study of particle populations such as the solar wind, pickup ions, and energetic particles, provides clues to the physical processes that govern the space environment. Some of these particle populations are not well understood due to their low densities and the low-sensitivity of instruments that are not specifically designed to search for them. With a new technique for mapping the solar magnetic field on which energetic particles travel, as well as improved instrumentation with the sensitivity necessary to measure low-density particle populations, the research outlined here will provide a new, powerful set of tools for studying the space environment. The Diffusive Equilibrium Mapping technique takes any footpoint of open magnetic flux on the solar surface and calculates where it reaches in the heliosphere, assuming pressure equilibrium. This method can model magnetic flux configurations that include open flux distributed outside of coronal holes, which may contribute to the source of streamer solar wind. Certain limitations on plasma mass spectrometers are investigated and overcome in the IonSpec design, which is capable of measuring an energy-per-charge passband of $(E/q)_{\max} = 3(E/q)_{\min}$ in a single voltage step. IonSpec has a larger integration time, geometric duty cycle, and energy-geometrical factor than similar

instruments and is capable of measuring the elemental abundances and ionic charge composition of all major solar wind and pickup ion species. In addition, a novel modification to cylindrically symmetric linear-electric-field time-of-flight analyzers allows for the focusing of secondary electrons emitted by the impact of isochronous ions. By identifying secondary electron peaks using their impact position, a single anode can be used to record both straight-through and isochronous flight times without a loss in the high-resolution isochronous measurement from a low signal-to-noise ratio. The new mapping technique and novel instrument designs will enable studies of the space environment that were previously not possible.

CHAPTER I

Introduction

The weather in space can have substantial effects on everything within the Sun's influence, including Earth. Most of the effects of space weather are mitigated by Earth's atmosphere and magnetic field, which form a barrier that much of the plasma in space cannot penetrate. Spacecraft and astronauts, however, risk exposure to potentially harmful radiation. Space weather can directly affect Earth's atmosphere, such as near Earth's poles where the magnetic field is shaped in such a way that the solar wind can interact with the upper atmosphere and create the aurora. Space weather can be dangerous, as storms from the Sun damage spacecraft and cause power outages on Earth. To protect astronauts and spacecraft from harm, an understanding of the fundamental physics behind space weather is vital. There are many unknown pieces to the puzzle, but through research and experimentation the picture is slowly being pieced together. As mankind looks toward further exploration of the Moon and the planets, the ability to forecast and protect humans from the effects of space weather become even more important.

This research examines new techniques and tools that can be used to study crucial pieces of the space weather puzzle. The emphasis is on ions found in the space environment: the solar wind (keV), pickup ions (10–100 keV), and energetic particles (100 keV–GeV). Each of these particle populations is created by a specific set of

processes, described briefly in Chapter II, and all have trajectories through space that are closely related to the magnetic field of the Sun and the heliosphere. Within the Alfvén radius (10–20 $R_\odot$), where the kinetic energy of the solar wind is weaker than the energy density of the Sun's magnetic field, the solar wind is guided by the field's shape and corotates with the Sun. Beyond this radial distance, the electrically charged and highly conductive solar wind controls and shapes the magnetic field, drawing it radially outward into the heliosphere. Energetic particles travel along the lines of magnetic flux that extend from the solar surface to the outermost reaches of the solar system. To a large degree, if the shape and path of the Sun's magnetic field can be accurately mapped, the trajectories of these particles could be inferred. However, such mapping techniques have been elusive, or inaccessible to the broad community. Chapter III explains a new mathematical mapping technique for the open magnetic flux of the Sun — magnetic flux that extends into the heliosphere so that it can be treated as being anchored at only one point in the Sun rather than a closed loop with both footpoints in the solar surface. This technique calculates where open magnetic flux on the solar surface will expand in the heliosphere and allows the direct testing of scenarios in which open magnetic flux is distributed throughout regions of predominantly closed flux — one of the possible sources of the streamer solar wind.

Particles that travel through space and are affected by the Sun's magnetic flux occasionally reach one of many spacecraft sent out to study them. Much of what is currently known about the space environment has come from data collected by specialized instruments on board these spacecraft. Among the various types of particle and field instrumentation are ion mass spectrometers, which can provide detailed measurements of a charged particle's energy, mass, charge, and even direction of travel. These measurements allow direct conclusions to be reached about the distribution functions of these particles, a measure of the probability that they will be in

a certain place at a certain time with a certain velocity. The theory behind advanced ion mass spectrometers used in space is outlined in Chapter IV, along with some specific parameters that are used to evaluate the functionality of such instruments. The next two chapters focus on the two main subsystems of such ion mass spectrometers: the electrostatic analyzer and the time-of-flight analyzer. Chapter V describes how a new design for an electrostatic analyzer was simulated, built, and tested with the goal of creating an instrument with more collecting power than those currently in use. It will allow for better measurements and improved statistics of particles like pickup ions and suprathermal ions, which are scarce but which play an important role in space weather. All high-energy particles are believed to be accelerated from this suprathermal component, yet little is known about its spatial evolution and temporal behavior. An improvement was also made to a current design of linear-electric-field time-of-flight analyzers (Chapter VI) that allows the instrument to have fewer parts and thus less mass, but does not diminish the resolution — a problem that has affected prior attempts at optimizing this design. This investigation into new designs and improvements for plasma instrumentation provides better tools to aid in the search for some of the missing pieces to the puzzle of space weather and its underlying physical processes.

CHAPTER II

Particle Transport and Acceleration

2.1 Introduction

For reference, some common equations and brief overviews of the three categories of particles will be given in this chapter. The Maxwell equations (2.1a)–(2.1d), the continuity equation for charge density and current density (2.2), the Lorentz force equation (2.3), Newton's second law of motion (2.4), and the magnetohydrodynamic (MHD) approximation of Ohm's Law (2.5) are each useful for basic plasma physics. Thorough derivations for these and related equations can be found in several textbooks, including *Gombosi* (1998) and *Jackson* (1999).

$$\nabla \cdot \mathbf{E} = \frac{\rho_e}{\epsilon_0} \qquad \text{Gauss's Law} \tag{2.1a}$$

$$\nabla \times \mathbf{E} = -\frac{\partial \mathbf{B}}{\partial t} \qquad \text{Faraday's law of induction} \tag{2.1b}$$

$$\nabla \cdot \mathbf{B} = 0 \qquad \text{Gauss's law for magnetism} \tag{2.1c}$$

$$\nabla \times \mathbf{B} = \mu_0 \mathbf{J} + \mu_0 \epsilon_0 \frac{\partial \mathbf{E}}{\partial t} \qquad \text{Ampère's law} \tag{2.1d}$$

$$\nabla \cdot \mathbf{J} = -\frac{\partial \rho_e}{\partial t} \qquad \text{continuity equation} \qquad (2.2)$$

$$\mathbf{F} = q\left(\mathbf{E} + \mathbf{v} \times \mathbf{B}\right) \quad \text{(N)} \qquad \text{Lorentz force} \qquad (2.3)$$

$$\mathbf{F} = m\mathbf{a} \quad \text{(N)} \qquad \text{Newton's 2nd law of motion} \qquad (2.4)$$

$$\mathbf{J} = \sigma\left(\mathbf{E} + \mathbf{v} \times \mathbf{B}\right) \quad \text{(A m}^{-2}\text{)} \qquad \text{Ohm's law} \qquad (2.5)$$

In these equations, ϵ_0 is the electric constant (also called the permittivity of free space), μ_0 is the magnetic constant (also called the permeability of free space), σ is the electrical conductivity, treated here as a constant, q is the charge, ρ_e is the charge density, m is the mass, $\mathbf{J}$ is the electric current density, and $\mathbf{E}$ and $\mathbf{B}$ are the electric and magnetic fields. $\mathbf{F}$, $\mathbf{v}$, and $\mathbf{a}$ represent force, velocity, and acceleration.

In MHD, the fields are induced by plasma motion, so the fields vary on the same time and length scales as the plasma variables. If high frequency variations in the electric field are not included, and only the non-relativistic regime is considered, the displacement current in Ampère's law can be neglected, leading to Equation 2.6.

$$\nabla \times \mathbf{B} = \mu_0 \mathbf{J} \qquad \text{MHD Ampère's law} \qquad (2.6)$$

By substituting Equation 2.1b and the curl of Equation 2.6 into the curl of Equation 2.5, $\mathbf{E}$ and $\mathbf{J}$ can be eliminated to derive the magnetic induction equation (2.7). The first term on the right describes the resistive diffusion of the magnetic field in the plasma while the second term describes the convection of the magnetic field by the plasma.

$$\frac{\partial \mathbf{B}}{\partial t} = \frac{1}{\sigma \mu_0} \nabla^2 \mathbf{B} + \nabla \times (\mathbf{v} \times \mathbf{B}) \qquad \text{magnetic induction equation} \qquad (2.7)$$

Since Equation 2.1c states that the divergence of the magnetic field vector $\mathbf{B}$ is

zero, $\mathbf{B}$ can be written in terms of a vector potential $\mathbf{A}$:

$$\mathbf{B} = \nabla \times \mathbf{A} \quad \text{(T)}. \tag{2.8}$$

By substituting Equation 2.8 into Equation 2.1b, Faraday's law of induction can be written as a quantity with a vanishing curl. Such a quantity can be rewritten as the gradient of a scalar function, the scalar potential Φ, leading to an equation for $\mathbf{E}$ in terms of the potentials $\mathbf{A}$ and Φ:

$$\mathbf{E} = -\nabla\Phi - \frac{\partial \mathbf{A}}{\partial t} \quad \text{(V m}^{-1}\text{)}. \tag{2.9}$$

For electrostatics, all derivatives with respect to time are zero. In this case, the divergence of Equation 2.9 combined with Equation 2.1a will give the Poisson equation, or in the absence of charges, the Laplace equation:

$$\nabla^2\Phi = -\frac{\rho_e}{\epsilon_0}, \qquad \text{Poisson's equation} \tag{2.10}$$

$$\nabla^2\Phi = 0. \qquad \text{Laplace's equation} \tag{2.11}$$

Due to the historical precedent of the symbols used in these and other common equations, a symbol may have different meanings depending on the equation in which it is used (i.e., 'E' can represent 'electric field' or 'energy'). Even though the meaning of the symbol can usually be discerned from the context of the equation, an attempt has been made to use distinct symbols throughout this dissertation, or use subscripts to clarify a symbol's meaning when necessary. In the specific case of 'E', the bold font $\mathbf{E}$ is used to represent the electric field vector and $|\mathbf{E}|$ to represent the magnitude of the electric field. The plain font E is always used here to represent energy.

Particle transport and acceleration are important topics of research in heliophysics. An understanding of the composition and nature of the gas and plasma found in

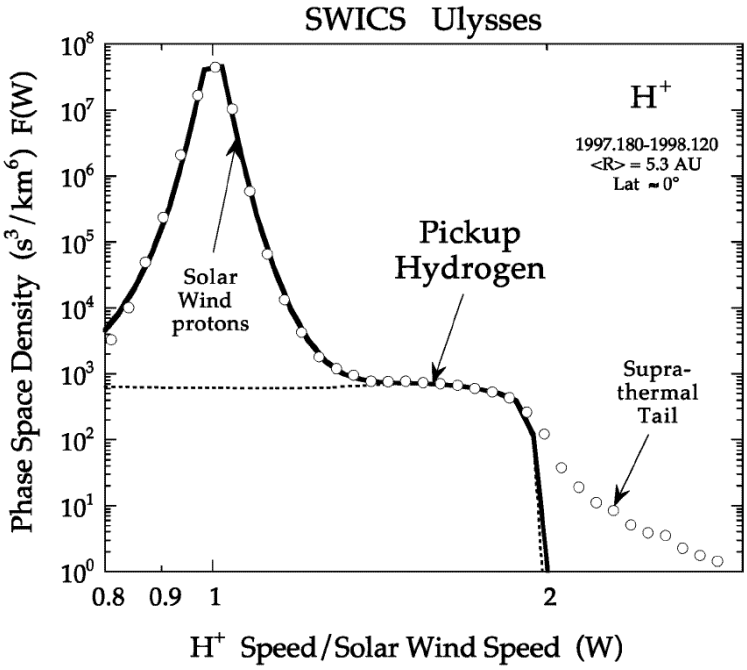

Figure 2.1: Example of proton distributions for the quiet solar wind near 5 AU. Shown are the bulk distribution of the solar wind, the interstellar pickup ions that drop off at twice the solar wind speed, and the high-energy protons that make up the suprathermal tail. Figure from *Gloeckler and Geiss* (2001).

space is vital to the forecasting of space weather. This research focuses on ways to investigate three categories of particles: the solar wind (§ 2.2), pickup ions (§ 2.3), and energetic particles (§ 2.4), as shown in Figure 2.1. The following is intended to provide sufficient background for the scope of this dissertation research.

2.2 The Solar Wind

2.2.1 Current Knowledge

While he was not the first to postulate its existence, the physics of the solar wind was first explained by Eugene Parker in 1958 (*Parker*, 1958). Beginning with subsonic speeds close to the Sun, plasma accelerates away from the solar surface and reaches supersonic speeds in the corona. It continues to expand in a radial direction outward until it interacts with the material in interstellar space at the edge of the heliosphere,

the Sun's sphere of influence. The wind draws the solar magnetic field along with it, creating spiral-shaped field lines as the Sun rotates (*Parker*, 1959). Mankind's understanding of the processes that govern the solar wind has increased as spacecraft have taken in situ measurements, but there are still some properties that remain unexplained, such as the precise origin of certain types of wind, as discussed below.

The solar wind travels a distance of one Astronomical Unit (AU) before reaching Earth's orbit, where most of the current measurements have been taken (Table 2.1). It is generally divided into two components, commonly referred to as the "fast" and "slow" solar wind. Originally, these terms were used to differentiate the wind by the speed with which it traveled, but more recent studies have shown that the two types of wind are more efficiently distinguished by their charge state composition (e.g., O^{7+}/O^{6+}) since the plasma can change speeds as it flows through space (*Geiss et al.*, 1995b; *Gloeckler et al.*, 2003). Rather than the terms "fast" and "slow", more appropriate labels are descriptive of the wind's origin: "coronal hole" and "streamer" wind. These two types of wind are generated by different processes and have different compositions, temperatures, speeds, and origins.

	Coronal Hole Wind	Streamer Wind
bulk speed (km s^{-1})	750	400
thermal speed (km s^{-1})	32	35
H^+ density (cm^{-3})	2.5	8.7
frozen-in temperature (K)	8 x 10^5	1.4–1.6 x 10^6

Table 2.1: Average characteristics of the solar wind at 1 AU. The temperature is derived from the freeze-in temperature of C^{6+}/C^{5+}, which freezes in near the solar wind source altitude. Data compiled from *von Steiger et al.* (1995); *Gloeckler and Geiss* (1998); *Ipavich et al.* (1998); *McComas et al.* (2000); *Feldman et al.* (2005).

As solar wind ions escape from the photosphere and travel up through the corona, they experience collisions with energetic electrons that ionize them to different degrees. As they travel farther through the corona, continuously accelerating, the density of coronal electrons decreases and the particles experience fewer collisions. When

the timescale for ionization or recombination becomes longer than the timescale of the solar wind to expand through a density scale height, the charge state of the ion is said to be "frozen in," branding the ion with the coronal region and electron temperature of its origin (*Hundhausen et al.*, 1968). The streamer wind has a distinct characteristic of being enriched in elements with a low ($\leq$ 10 eV) first ionization potential (FIP) by a factor of 3–4 over the photospheric value. The coronal hole wind does not show this density enhancement, and measurements have revealed abundances of low-FIP elements that match ratios in the photosphere (*von Steiger and Geiss*, 1993). The streamer wind also has a higher and more variable freeze-in temperature than the coronal hole wind. One explanation for this describes solar plasma trapped and heated in large coronal loops that are eventually opened by interchange reconnection, releasing the plasma (*Gosling et al.*, 1995; *Fisk et al.*, 1998, 1999).

The coronal hole wind originates in the open flux regions of the Sun, which contain low-density plasma and concentrations of magnetic flux that are all the same polarity. During solar minimum these regions are clustered around the poles of the Sun, while during solar maximum they appear at all latitudes. Plasma in open flux regions is also released from flux loops, but the high concentration of open flux increases the probability that the loops will open before they can heat and fractionate the plasma. The anti-correlation between freeze-in temperature and solar wind speed shown in Table 2.1 can be interpreted in a simplistic way as a sign of different sized loops. The long-lived loops that produce the streamer wind will expand and rise slowly into the corona, where the temperatures are hotter, before being opened (*Fisk et al.*, 1998; *Fisk and Schwadron*, 2001a). The short-lived loops that yield the coronal hole wind are opened while they are still small and close to the cooler surface (*Fisk et al.*, 1999; *Fisk*, 2003; *Wimmer-Schweingruber*, 2003).

2.2.2 The Streamer Wind Puzzle

The precise origin of the streamer wind is a topic of some disagreement in the scientific community (*Zurbuchen*, 2007; *Riley*, 2007). It is agreed that the streamer wind must escape the Sun via lines of open magnetic flux, but the precise location of the footpoints of these lines has not yet been determined. Simplified models of the Sun divide it into regions of open and closed magnetic flux and assign only the regions of high concentrations of open flux as the sources of all solar wind (*Altschuler and Newkirk*, 1969; *Schatten et al.*, 1969). These models constrain the slower, streamer wind to the boundaries of the open flux concentrations in coronal holes, however, the composition of the plasma in these areas is not consistent with streamer wind observations. Efforts have been made to include active regions into the list of possible sources for the streamer wind (*Neugebauer et al.*, 2002), and progress is being made in matching the composition. Other models involve plasma that is released from loops outside of coronal holes, in the quiet regions of the Sun. These models are explored in more detail with a new mapping technique for the open flux of the Sun (Chapter III).

The composition of the solar wind gives clues to its origin, and new mass spectrometers with higher resolution will allow better analysis of complicated structures found within it, such as corotating interaction regions and coronal mass ejections. The latter are particularly important because they contribute up to $\sim$16% of the solar wind's mass during solar maximum (*Jackson and Howard*, 1993). The development of instruments such as IonSpec (Chapter V) and the new techniques for time-of-flight mass spectrometry (Chapter VI) will greatly assist in this pursuit.

2.3 Pickup Ions

2.3.1 Current Knowledge

A minor, but important, component of the plasma in the solar system is a class of particles known as "pickup ions". Pickup ions are formed when neutral gas and dust are ionized by collisions with solar wind ions or by photoionization. They are then picked up and carried out by the solar wind as it travels toward the edges of the solar system (*Axford*, 1972, 1973). The sources of these neutral particles include material from the local interstellar cloud that enters the solar system as the Sun drifts through it at 26 km s^{-1}, as well as inner sources such as comets, planets, and solar wind particles that are absorbed and re-emitted by dust. Instruments such as the Suprathermal Energy Ionic Charge Analyzer (SULEICA) on the Active Magnetospheric Particle Tracer Explorers (AMPTE)–Ion Release Module (IRM) satellite, the Ultra-Low-Energy Charge Analyzer (ULECA) on the *International Cometary Explorer (ICE)* (*Ipavich et al.*, 1986), the Solar Wind Ion Composition Spectrometer (SWICS) on the *Ulysses* mission (*Gloeckler et al.*, 1992), the Charge, Element, and Isotope Analysis System (CELIAS) suite on the *Solar and Heliospheric Observatory (SOHO)* (*Hovestadt et al.*, 1995), and the *Mercury: Surface, Space Environment, Geochemistry, Ranging (MESSENGER)*–Fast Imaging Plasma Spectrometer (FIPS) (*Koehn et al.*, 2002) have all captured and measured pickup ions in the inner heliosphere. Their measurements provide, among other things, a remarkable glimpse into the composition of interstellar cloud material that has made its way close to the Sun (*Geiss et al.*, 1994b, 1995a; *Gloeckler and Geiss*, 1996). Pickup ions are thought to form the main component of anomalous cosmic rays (ACRs) (*Fisk et al.*, 1974; *Gloeckler et al.*, 2000b), and are easily distinguished from ions of solar origin because they have low charge states, different spatial distributions, and distinct velocity distributions. Figure 2.2 shows measurements of pickup ions taken by the *Ulysses*–SWICS instrument.

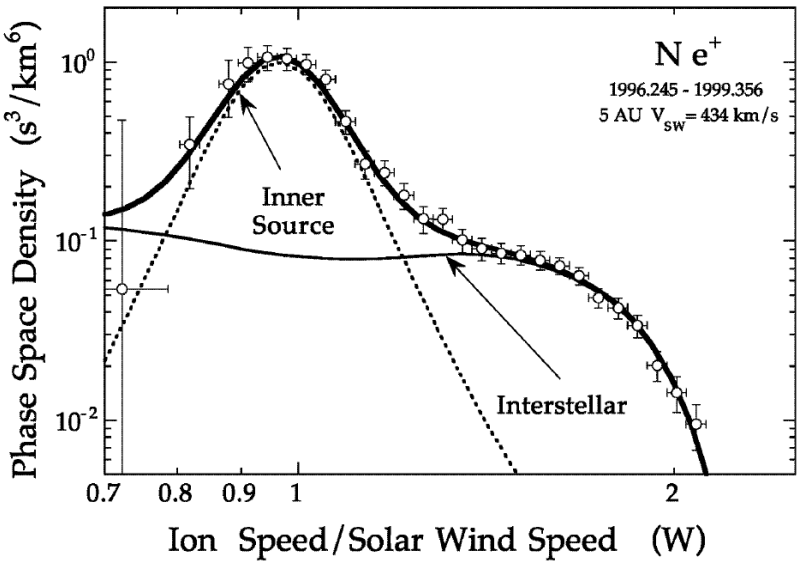

Figure 2.2: Measurements of pickup ions in the heliosphere. The inner-source ions tend to adiabatically cool around $W = 1$, where W is the ratio of the pickup ion speed to the solar wind bulk speed. There is a cutoff in density of interstellar pickup ions at $W = 2$, with a tail at higher W of accelerated ions. Figure adapted from *Gloeckler and Geiss* (2001).

Following common usage of notation (e.g., *Gloeckler and Geiss*, 1998), the pickup ion speed $V_{\rm ion}$ relative to the speed of the ambient bulk solar wind $V_{\rm sw}$ is written as

$$W = \frac{V_{\rm ion}}{V_{\rm sw}}. \tag{2.12}$$

The highly energetic and hot ($\sim 10^6$ K) environment of the Sun will strip off multiple electrons from atoms as they escape its surface, as described previously. Pickup ions (Helium excluded) tend to be singly charged since they are generated away from the Sun, in the heliosphere. Once a pickup ion is created, it is immediately carried outward by the solar wind far enough away from the Sun that the odds of a second ionization are negligible. An exception to this charge state characteristic is Helium, which has a large ionization cross section and can be found as a doubly charged pickup ion (*Gloeckler and Geiss*, 1998).

The spatial distribution of inner-source pickup ions depends on their distance

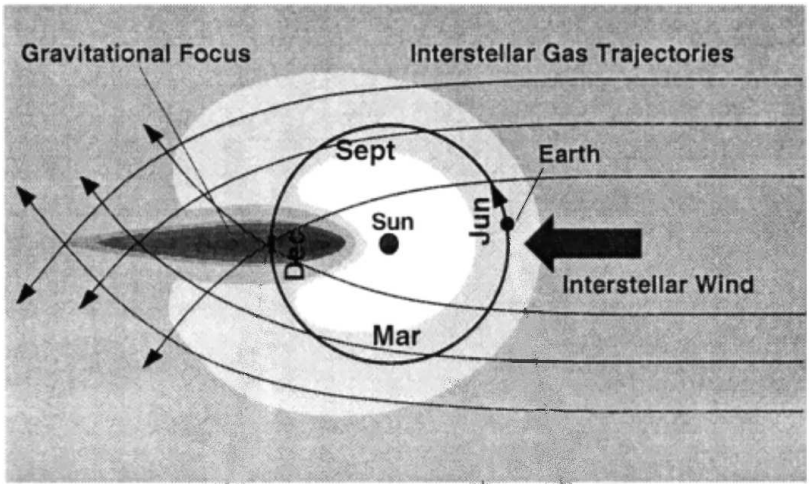

Figure 2.3: The Interplanetary Focusing Cone. Interstellar gas experiences gravitational focusing as it travels past the Sun, leading to a density enhancement downstream of the Sun. Figure adapted from *Möbius et al.* (1999).

from their source, with the ion density decreasing farther from the source (*Vasyliunas and Siscoe*, 1976; *Cheng*, 1986; *Neugebauer et al.*, 1987; *Geiss et al.*, 1994a). Model calculations show that ions produced from interstellar gas will have maximum abundances with distances from the Sun that vary depending on the ionization rate of the particles (i.e., some elements (He) can make it closer to the Sun than others (H, O, N) before becoming ionized) (*Thomas*, 1978; *Holzer*, 1989). Another factor that determines the spatial distribution of interstellar pickup ions is the angle of the observation relative to the solar apex — the direction that the Sun travels through space (*Vasyliunas and Siscoe*, 1976; *Bzowski and Ruciński*, 1996). Interstellar gas experiences a gravitational focusing as it passes by the Sun, leading to a downstream density increase — the so-called Interplanetary Focusing Cone (Figure 2.3) (*Möbius et al.*, 1999; *Kallenbach et al.*, 2000). The higher density of neutral particles in the cone (mostly He atoms) leads to a higher density of interstellar pickup ions forming in this region.

When a pickup ion is created it is nearly stationary with respect to the solar wind ($W \ll 1$) in the spacecraft frame of reference. It is immediately caught up by the

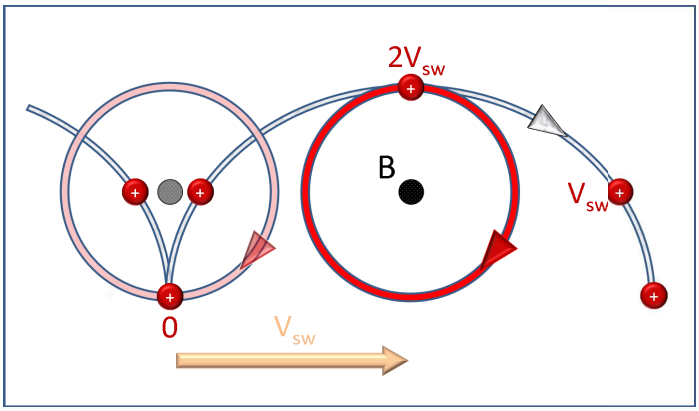

Figure 2.4: Illustration of the pickup ion velocity range. The magnetic field **B** (directed out of the page) travels at the speed of the frozen-in solar wind $V_{\rm sw}$. As pickup ions gyrate around the magnetic field line, their speed varies between $W = 0$ and $W = 2$.

magnetic field in the supersonically expanding solar wind and begins to accelerate. The newly generated ion will both experience and create MHD turbulence in the solar wind flow, causing a scattering of its pitch angle and creating a shell-like distribution of pickup ion velocities when plotted in velocity space (*Holzer and Leer*, 1973; *Isenberg*, 1986; *Fahr and Ruciński*, 2002). This pickup shell is centered at $V_{\rm sw}$ with a radius of $V_{\rm sw}$. Due to the way the ions orbit around lines of heliospheric magnetic flux, which are traveling at $V_{\rm sw}$, they can be found with relative speeds ranging from $W = 0$ to as high as $W = 2$ in the unperturbed solar wind (Figure 2.4). When the velocity distributions of the solar wind and pickup ions are examined in more detail, suprathermal tails are found that follow a power law form with a spectral index of -5 (*Fisk and Gloeckler*, 2006). In acceleration regions such as shock waves, the intensities of the accelerated ions increase, but they are present in even undisturbed conditions (*Gloeckler*, 2003). As pickup ions travel with the solar wind, they are adiabatically cooled, which causes them to lose energy. This becomes apparent for inner-source pickup ions in particular because no new pickup ions are added to the population once the solar wind has left the region of the source. The velocity distribution becomes narrower, converging with a cutoff speed approaching $W = 1$ instead

of $W = 2$ (*Gloeckler and Geiss*, 1998).

The first interstellar pickup ion species to be discovered was $^4He^+$ (*Möbius et al.*, 1985). Since that time, many more species have been found, including H^+ (*Gloeckler et al.*, 1993), O^+, N^+, and $^{20}Ne^+$ (*Geiss et al.*, 1994b), C^+ (*Geiss et al.*, 1995a), $^3He^+$, $^4He^{2+}$ (*Gloeckler and Geiss*, 1996), Mg^+, and Si^+ (*Gloeckler et al.*, 2000a). Pickup ions produced from atoms with a high FIP, such as H, He, and Ne, tend to come from interstellar sources that penetrate deep into the heliosphere before being ionized. Interstellar atoms with a lower FIP, such as C, Si, Mg, and Fe, are more easily ionized so will not enter as far into the heliosphere before they lose an electron and become picked up and carried outward by the solar wind. The low-FIP pickup ions detected by *Ulysses* are believed to have been generated within the inner heliosphere, in the so-called inner source (*Geiss et al.*, 1995a; *Schwadron and Gloeckler*, 2007).

One significant result from $^3He^+$ pickup ion data is the new lower limit on the amount of missing matter in the early Universe: the amount of ^3He production in stars was found to be less than what models predicted, as shown in *Gloeckler and Geiss* (1996). Because pickup ions allow the measurement of distant neutral sources, they can be used for other fundamental research, such as insights into the space weathering effects of the Sun on planets, comets, Kuiper belt objects, and asteroids. Pickup ions offer a unique opportunity to measure a direct sample of the present-day galaxy.

2.3.2 Unresolved Issues

There are some inner-source pickup ions (O^+, C^+) for which the exact method of creation is unknown. A number of possible sources are summarized in *Allegrini et al.* (2005), including small comets, dust-dust collisions, dust that captures and neutralizes solar wind ions that are then re-ionized and picked up by the wind (*Gloeckler et al.*, 2000a), and solar wind neutralization (*Wimmer-Schweingruber and Bochsler*, 2003).

Additional in situ data could be used in conjunction with the knowledge gained from existing instruments to help narrow down the possible sources of inner-source pickup ions.

The breakthrough measurements of the rare $^3He^+$ pickup ion consisted of only a couple of counts per year (*Gloeckler and Geiss*, 1996) by the SWICS instrument on the spacecraft *Ulysses*. An instrument with a larger data-collecting rate would improve the statics for this and other measurements by providing a larger sample size of data. One of the objectives of the research discussed in this dissertation was to develop and test an instrument with a design similar to the instrument that has discovered many of the known pickup ions, SWICS, but with a greater collecting power (Chapter V).

2.4 Energetic Particles

2.4.1 Current Knowledge

Energetic particles carry signatures that reveal the large-scale properties of the Sun, heliosphere, and galaxy. They also make up the most hazardous component of space weather, both to humans and spacecraft, due to their ability to penetrate objects, causing material degradation and mutations. There is an entire spectrum of energetic particles found in the heliosphere, as shown in Figure 2.5. Three main categories can be formed from this spectrum: energetic particles produced by the Sun, particles in the heliosphere that are accelerated to high energies, and galactic cosmic rays that originate outside of the solar system.

A broad range of particles ejected from the Sun are grouped together as solar energetic particles (SEPs). Historically, they have been classified as either impulsive (lasting from minutes to hours) or gradual (lasting from hours to days) events, but the difference between those categories is becoming blurred as new measurements are

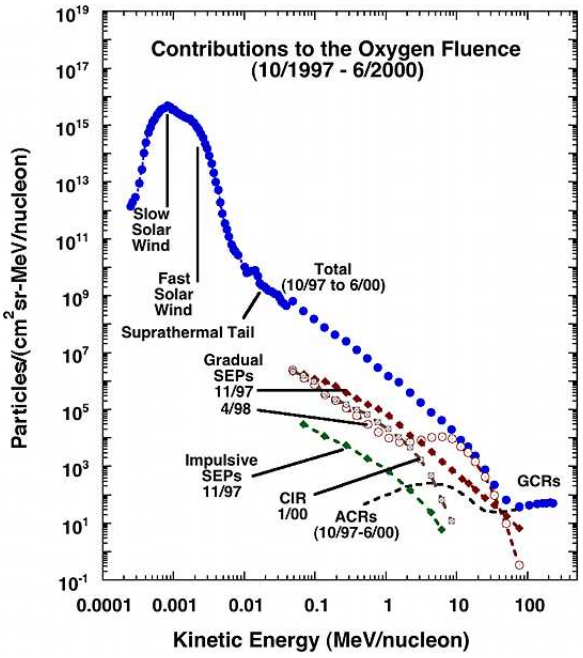

Figure 2.5: The energy spectrum of energetic particles in the heliosphere. Shown here are spectra of energetic oxygen nuclei as measured by four instruments on board *ACE*, as well as solar events, corotating interaction regions, and cosmic rays. Figure from *Mewaldt et al.* (2007).

revealing more about the nature of SEPs (*Klecker et al.*, 2006). The exact nature of impulsive events is still a topic of active research, but the consensus seems to indicate that they are accelerated in solar flares that may or may not be associated with narrow (or wide), fast coronal mass ejections (CMEs) (*Reames*, 1999; *Kahler et al.*, 2001; *Tan and Yan*, 2008). Impulsive events send out particles with charge states that indicate an origin of 2–7 x 10^6 K, and with energy per nucleon in the MeV range (*Luhn et al.*, 1984). They tend to be enhanced in heavy ions, have higher charge states of these ions, and have an elevated ^{3}He/^{4}He ratio (*Hurford et al.*, 1975; *Anglin et al.*, 1973). Gradual events are created by the fastest ∼1–2% of CMEs (which are sometimes accompanied by solar flares) (*Reames*, 1999). As a CME erupts into the heliosphere, it rapidly plows through the solar wind, driving a shock ahead of it. Particles are accelerated up to the MeV/nucleon range by magnetic turbulence on either side of the shock, gaining energy either by diffusive shock acceleration when

the shock normal and the heliospheric magnetic field are quasi-parallel, or by a $\mathbf{v} \times \mathbf{B}$ drift in the case of a quasi-perpendicular shock (*Decker and Vlahos*, 1986; *Reames*, 1999).

Particles in the heliosphere, whether of solar origin or not, can be accelerated to high energies via a variety of mechanisms. During the solar minimum phase of the Sun's 11-year cycle, the solar magnetic field is dipole shaped with inward magnetic flux at one pole and outward magnetic flux at the other. The different polarities are separated by the heliospheric current sheet (HCS), which is located near the solar equator during solar minimum. The streamer wind has been found to escape the Sun near the HCS, while the coronal hole wind rises from coronal holes far from the HCS. When the Sun's magnetic dipole axis is tilted with respect to its rotation axis, high speed coronal hole wind can be found streaming through the ecliptic. This tilt along with other possible asymmetries in the field gives the current sheet a warped appearance such that a stationary observer near the ecliptic will see alternating streams of wind from coronal holes and the HCS-associated streamers. The observer is bathed in alternating flows of streamer and coronal hole wind as the HCS and coronal holes respectively rotate into view. The coronal hole wind travels at higher speeds on average and overtakes the streamer wind emitted previously, plowing forcefully through it (*Barnes and Simpson*, 1976; *Pizzo*, 1978; *Riley*, 2007). These areas of interaction between coronal hole and streamer wind corotate with the Sun and are appropriately called corotating interaction regions (CIRs). Their strength increases with increasing distance from the Sun as more coronal hole wind piles up from behind, and they can last for several solar rotations (Figure 2.6).

At the edges of CIRs, shock waves form and propagate both toward and away from the Sun. Pickup ions and particles found in the suprathermal tail of the solar wind velocity distribution have speeds high enough to be injected into a diffusive shock acceleration mechanism at the CIR shock. Diffusive shock acceleration, or

other mechanisms, cause particles injected into these shocks to gain energy until they eventually are released (*Barnes and Simpson*, 1976; *Fisk and Lee*, 1980; *Gloeckler et al.*, 2000b). Particles accelerated by CIRs were observed by the *Ulysses* spacecraft as it flew over the poles of the Sun, revealing that some formerly unknown transport mechanism was guiding them away from the magnetic field lines associated with the ecliptic-bound CIR. Explanations for this particle transport include the Fisk model of systematic field line migration (*Fisk*, 1996), and the random-walk field line motion proposed by *Kóta and Jokipii* (1998). Measurements of their elemental abundances have shown that some CIR particles have compositions matching the coronal hole wind, as opposed to the SEP events that are similar to streamer wind features (*Geiss et al.*, 1995b). This can be understood by realizing that nearly all of the MeV ions measured by spacecraft near Earth are coronal hole wind ions that are accelerated in the distant CIR's reverse shock. There is also a component of interstellar pickup ions that are accelerated in CIR shocks, leading to high abundances of H^+ and He^+ in the energetic particles (*Gloeckler et al.*, 1993, 1994).

In the energy range of ∼10–50 MeV/nucleon are a group of particles classified as anomalous cosmic rays. The journey of these ACRs into the heliosphere is impeded by the flow of the high-speed solar wind and by CIRs (*Reames*, 1999), similar to the modulation patterns observed in galactic cosmic rays. Their composition is similar to interstellar pickup ions, and *Fisk et al.* (1974) proposed that the ACR origin was from pickup ions that were carried by the solar wind and accelerated to higher energies. The rare component of ACRs, including such elements as C, Mg, Si, S, and Fe, may originate from inner-source pickup ions (*Gloeckler et al.*, 2000b). The location of this acceleration was initially thought to be at the the termination shock of the heliosphere (*Pesses et al.*, 1981; *Fisk*, 1986), shown in Figure 2.7, but when the two *Voyager* spacecraft crossed the termination shock, they found that the intensity of ACRs did not peak there. The acceleration of ACRs must occur either somewhere else

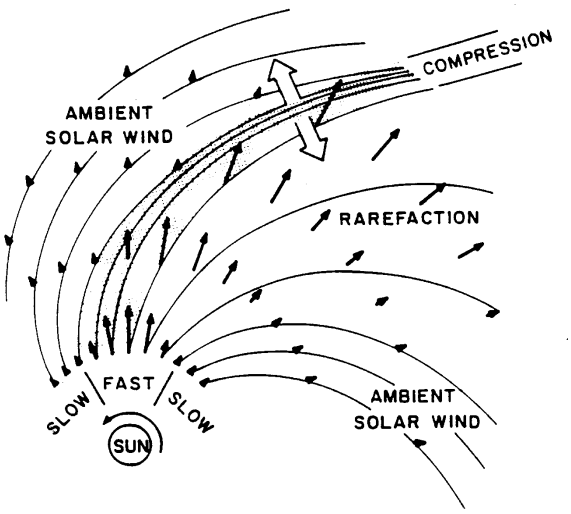

Figure 2.6: Illustration of a corotating interaction region. As the Sun rotates, coronal hole wind overtakes the streamer wind emitted previously and a CIR forms. Acceleration takes place on the leading and trailing edges of the region as well as in between, accelerating particles to higher energies. Figure adapted from *Pizzo* (1978).

on the termination shock, or deeper in the heliosheath, beyond the termination shock (*Stone et al.*, 2005). *Fisk and Gloeckler* (2007) propose that compressional turbulence in the heliosheath beyond the termination shock may accelerate the pickup ions by means of stochastic acceleration, sending them back into the heliosphere as ACRs.

The particles with the highest energies, galactic cosmic rays (GCRs), are about 83% protons (H^+), 13% alpha particles (He^{2+}), and 3% energetic electrons (e^-) with energies extending upward from $E > 10^7$ eV (*Mewaldt et al.*, 1984; *Gombosi*, 1998; *Hörandel*, 2008). They form far from the solar system and travel through interstellar space to reach the heliosphere. In the outer heliosphere the magnetic field strength is on the order of 1 nT, so 1 GeV particles will have gyroradii (Equation 2.14) on the order of an AU.

$$\Omega_c = \frac{|q|B_0}{m} \quad (\mathrm{s}^{-1}) \qquad \text{gyrofrequency} \tag{2.13}$$

$$r = \frac{v_\perp}{\Omega_c} \quad (\mathrm{m}) \qquad \text{gyroradius} \tag{2.14}$$

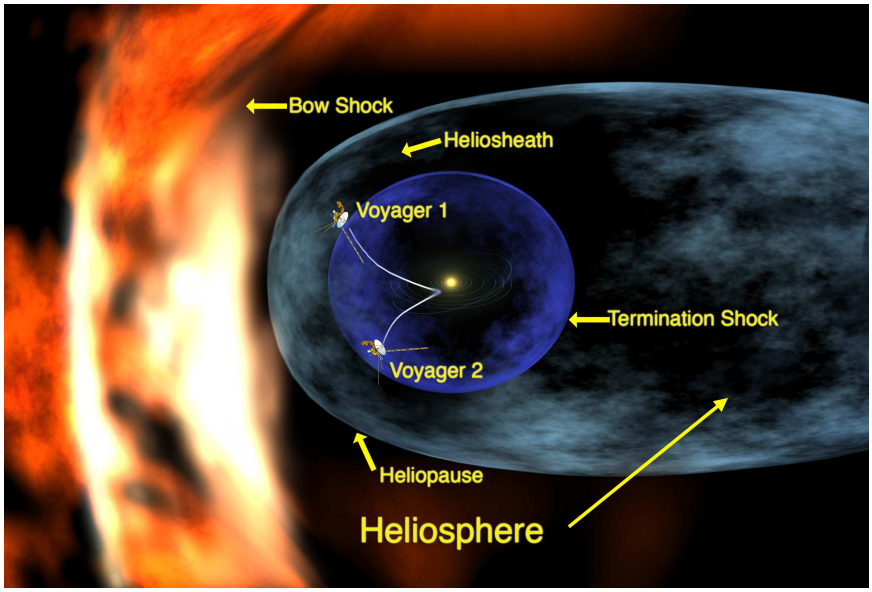

Figure 2.7: The regions of the heliosphere. Also shown are the *Voyager I* and *II* spacecraft, which now have both crossed the termination shock. Graphic credited to NASA/Walt Feimer.

GCRs with higher energies can have gyroradii larger than the size of the heliosphere, so modulation by the solar field does not have much of an effect on them, and their energy spectra follows a power law relation (Figure 2.8). The intensity of GCRs with energies in the MeV range show a periodic variation that is anti-correlated with the sunspot cycle (*Forbush*, 1954), indicating that solar activity has a modulation effect. Pitch-angle scattering of the GCRs due to turbulence in the heliospheric magnetic field prevents some of the particles from traveling deep into the heliosphere (*Gombosi*, 1998).

2.4.2 Unanswered Questions

There is still some important work to be done with regards to energetic particles. For example, the exact cause of impulsive events is still an area of active research. An understanding of these events will come in conjunction with knowledge regarding the relationship between CMEs and solar flares. The location and nature of ACR acceleration is also still under investigation, and it is hoped that the *Voyager* missions

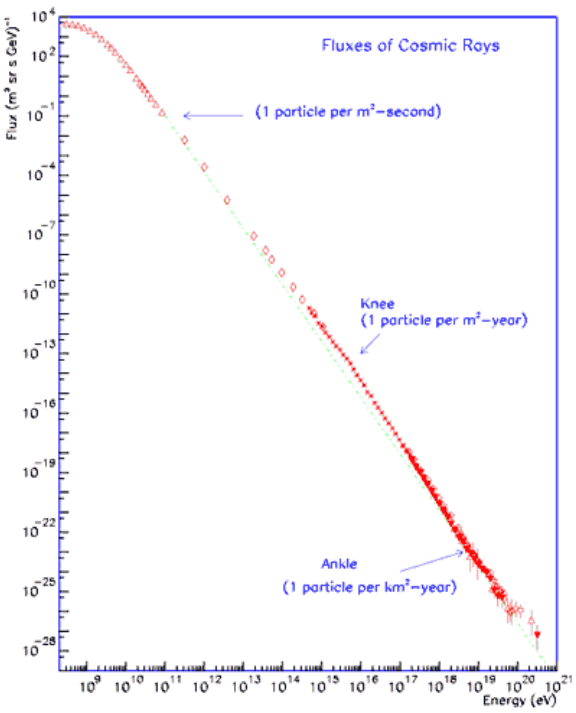

Figure 2.8: The cosmic ray spectrum measured at the top of the atmosphere. Energies in the GeV range follow a power law relation, with the slope changing at the 'knee' and 'ankle'. Figure from *Shellard* (2001).

will continue to reveal clues on their journey.

The solar wind is a source of much acceleration, and the key to understanding energetic particles may be in the suprathermal range of the solar wind's energy spectrum. The core problems of particle acceleration relate to how particles are injected into shocks, and the processes by which they leave their thermal core. New instrumentation with higher collecting power and a broader energy passband would allow additional measurements to help solve these puzzles. The suprathermal range in particular is addressed by a new style of mass spectrometer, the development of which is explained in Chapter V.

CHAPTER III

Trajectory Mapping

3.1 Introduction

Open magnetic field lines are portions of the solar magnetic field that are carried out to the heliosphere by the solar wind and are the pathway through which energetic particles escape from the corona. An important objective of solar and heliospheric research is to map these open field lines back to their locations of origin on the solar surface; but due to its topological diversity, its time evolution on multiple scales, and the poorly understood coronal heating processes, there is a great deal of difficulty involved for those who attempt to model the magnetic field of the Sun. A model must be able to predict how closed flux, such as solar loops and streamers, relate to open flux. It also must provide a way for time-stationary plasma to accelerate to supersonic speeds, transition from regions dominated by collisions to a collisionless regime, and describe an environment of low plasma β (the ratio of plasma pressure to magnetic pressure) near the Sun and higher plasma β far from the Sun (*Parker*, 1958; *Schunk and Nagy*, 2000). There are a number of different approaches to modeling the magnetic field of the Sun, including MHD and potential field models.

The first of these types of models describes the coronal magnetic field by solving the MHD equations to steady state. MHD models are extremely useful and are considered by many to be the ideal tool for describing the coronal and heliospheric

environment. The models face some difficulty, however, since the computational resources required for a detailed global model are often prohibitive and since the process of coronal heating is currently not understood well enough to be modeled accurately. Even with these limitations, there have been many productive studies carried out using these types of models (e.g., *Lionello et al.*, 2005; *Roussev et al.*, 2003; *Suess et al.*, 1999; *Manchester et al.*, 2004). The models have recently become available to a broader community through modeling centers such as the Community Coordinated Modeling Center (CCMC).

The main focus of this research deals with the second type of model, the potential field source surface (PFSS) model. The details of this model can be found in studies by *Altschuler and Newkirk* (1969) and *Schatten et al.* (1969), but are summarized here. In a standard PFSS model, a spherical surface is chosen at some distance $r = R_{\rm ss}$ from the center of the Sun and is assigned to be the source surface of the solar wind. The source surface is imposed to simulate effects not included in the model, such as the velocity field and gas pressure. Between the solar surface and the source surface ($R_\odot < r < R_{\rm ss}$), the corona is assumed to be current free ($\nabla \times \mathbf{B} = 0$). When global currents are neglected, a potential field can be calculated and traced using solutions of the Laplace equation (2.11) in terms of Legendre polynomials (*Altschuler and Newkirk*, 1969) or by using a Green's function solution to the Maxwell equations (*Schatten et al.*, 1969). The potential is assumed to be zero at the source surface, forcing the magnetic field into the radial direction, but still allowing its magnitude to vary in latitude and longitude. Beyond the source surface, localized currents are assumed to exist as the solar wind drags and bends the magnetic field.

There are different possibilities for an inner boundary condition, including a radial or nonradial magnetic field. By assuming that the observations of the photospheric magnetic field are made at a sufficient depth that the field is oriented radially (*Wang and Sheeley*, 1992), the inner boundary condition can be set as such and the equations

found in the work of *Altschuler and Newkirk* (1969) can be used to approximate the vector magnetic field in the entire current-free region. The field distribution in this region represents an implicit force balance between magnetic tension and magnetic pressure, subject to the constraint imposed by the radial field condition on the source surface. While the source surface modifies the field in the current-free region in a way similar to introducing gas pressure forces, MHD simulations have shown that these imposed pressure forces are not necessarily equivalent to the ram pressure and internal pressure of the solar wind (*Riley et al.*, 2006). Potential field solutions are useful from a computational perspective, as they are easy to implement and do not require the computational resources that a full MHD model requires.

A great deal of research has been performed using potential field models, and the results have proven useful, especially in the context of space weather predictions (e.g., *Arge and Pizzo*, 2000; *Liewer et al.*, 2004; *Zhao and Hoeksema*, 1995; *Wang et al.*, 2000), but there are approximations and limitations in the PFSS model that must be recognized when interpreting the results (see *Luhmann et al.*, 2002, and references therein). One is that the model assumes an idealized potential field in a volume that may have nonpotential regions. By utilizing this current-free condition, some information from nonpotential active regions, for example, may be lost at high resolution. The input data also limit the accuracy of this (and any) model, since measurements are only taken near the central meridian. Typically, a full solar rotation is required to capture a global picture of the coronal magnetic field, but by the time a full rotation is completed, some short-lived features on the Sun will have changed. Another limitation comes from the crucial lack of time dependence. Since they are static, potential field models cannot account for evolutionary effects, such as magnetic reconnection, differential rotation, or magnetic field diffusion. A PFSS model also falls short in accounting for the possibility of open flux distributed in low concentrations outside of coronal holes, because this scenario would demand nonzero currents. Note

that in this dissertation the term "coronal hole" is used in the heliospheric sense only — a source region of the high speed coronal hole wind with cool charge states — and the term "coronal hole boundary" refers to a boundary between coronal hole and streamer wind. These limitations make it impossible to account for coronal loops that heat plasma and release it when they are opened by a passing open field line (*Fisk et al.*, 1998), which is a form of interchange reconnection (*Gosling et al.*, 1995; *Fisk and Schwadron*, 2001b; *Crooker et al.*, 2002). A process such as this can only be modeled in a time-dependent setting and provides the primary mechanism for escape of streamer wind plasma in some theories (e.g., *Fisk et al.*, 1998). There have been several modifications of the PFSS model to correct some of its shortcomings, such as including the effects of localized current sheets (*Wang and Sheeley*, 1995; *Zhao and Hoeksema*, 1994; *Schatten*, 1971) and the use of nonspherical source surfaces (*Schulz et al.*, 1978). The model proposed here is a physics-based magnetic field expansion model that addresses a specific condition revealed by the *Ulysses* mission, with broad applications for and beyond the PFSS model (*Gilbert et al.*, 2007b).

The *Ulysses* spacecraft made pioneering observations of the heliospheric field at all heliospheric latitudes and found that there was relatively little latitudinal gradient in the radial component (B_r) of the interplanetary magnetic field (*Balogh et al.*, 1995; *Smith and Balogh*, 1995). This indicates that although open magnetic flux is unevenly distributed at the surface of the Sun, B_r becomes uniformly distributed at some distance in the outer corona. As the solar wind carries magnetic flux from the surface of the Sun into the heliosphere, the flux concentrations tend to spread in solid angle due to magnetic pressure forces, which cause the radial magnetic flux to equilibrate (*Suess and Smith*, 1996; *Suess et al.*, 1996). PFSS models predict latitudinal and longitudinal gradients in the magnitude of B_r that must be corrected to accurately model the *Ulysses* observations.

In *Gilbert et al.* (2007b), a mathematical mapping tool was developed that can be

used in conjunction with standard potential field models, or more generalized models, and that will lead to a heliospheric field without latitudinal gradients. This tool is referred to as Diffusive Equilibrium Mapping, and is introduced with a detailed derivation and conceptual explanations in § 3.2. In § 3.3 the discussion focuses on applications of the technique as applied in conjunction with PFSS models; and § 3.4 addresses the applicability of this method beyond PFSS models, such as the application proposed by *Fisk et al.* (1998), which predicts open field lines from topologically closed regions on the Sun.

3.2 Mathematical Mapping Tool

Before proceeding with the mathematical derivation of the mapping technique, it is useful to discuss it from a conceptual perspective. This technique does not result in an actual trace of a field line through three-dimensional space; the "trace" is a purely mathematical reference to connect the final and initial points. The final heliospheric location in latitude and longitude of any initial photospheric open flux is a physical result and should be interpreted as such. The technique is based on the idea that magnetic pressure forces will cause magnetic flux to relax to a state of equilibrium in the heliosphere.

Imagine a spherical surface with concentrations of purely radial, open magnetic flux located in certain localized areas but not anchored in place, as shown in Figure 3.1(a). The frozen-in field lines should be expected to move with some velocity on the surface as the influence of magnetic pressure causes the field to relax toward equilibrium. A velocity field $\mathbf{u}_\perp$, which is perpendicular to the radial direction, can be used to follow the displacement of the magnetic field lines until they reach pressure equilibrium, as shown in Figures 3.1(b)–(d). The field lines move on a sphere of constant radius, and once the field line motion has stopped, the final latitudes and longitudes of the equilibrated flux can be recorded.

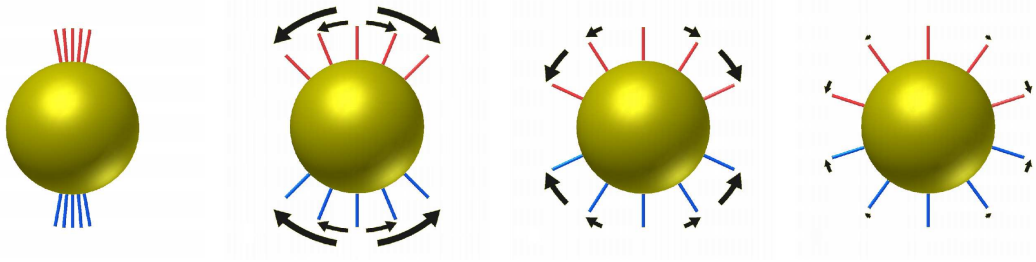

Figure 3.1: Conceptual example of field line diffusion. (a) Start with concentrations of radial, stiff open magnetic flux extruding from the photosphere that are not anchored in place so they are free to diffuse around on the surface. (b)–(d) As the open flux relaxes to a state of pressure equilibrium, the speed of field-line motion can be characterized at each time step with the expansion velocity $\mathbf{u}_\perp$, indicated by the black arrows. Figure from *Gilbert et al.* (2007b).

If the magnetic flux was constrained by the same forces throughout the heliosphere, the magnetic topology would look like Figure 3.1(a) everywhere. But since it is not constrained, the magnetic pressure creates a force that causes the flux to expand in latitude and longitude, as illustrated in Figures 3.1(b)–(d). In reality, this expansion does not occur on the surface of the Sun, but at higher altitudes. If each time step is mapped onto a successively larger radial shell, the velocity field can help reveal a three-dimensional view of which footpoint at the Sun connects to which endpoint in the heliosphere. Figure 3.2 takes the expansion shown in the four images of Figure 3.1 and superimposes them, with each successive sphere being placed at a farther radial distance. The same footpoints were connected from one sphere to the next to give a visual mapping of the flux motion. The result is a representation of the initial concentrations of open flux on the photosphere and the final locations of open flux in the heliosphere, with a mathematical trace connecting the two for visual clarity.

The velocity field that follows field line movement in this conceptual description is referred as the "expansion velocity" (*Gilbert et al.*, 2007b). It is not a physical velocity for plasma flow, or even of field line movement, but is actually related to gradients in the magnetic field, as is shown later. The expansion velocity is a mathematical

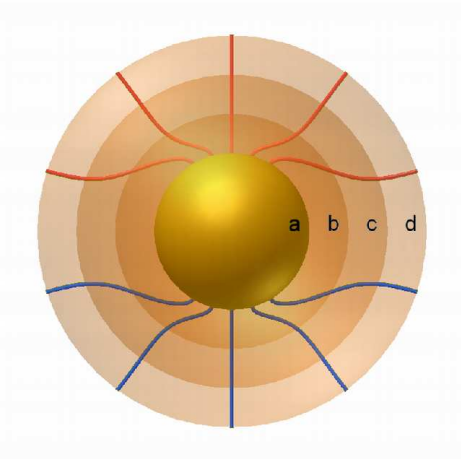

Figure 3.2: Superposition of the four images from Figure 3.1. Each successive sphere is placed at a farther radial distance, and a line is drawn following the expansion velocity field, which indicates the movement of a footpoint from one sphere to the next. This allows one to see the initial photospheric locations of open flux and their equilibrated locations in the heliosphere with a mathematical trace connecting the two for visual clarity. Figure from *Gilbert et al.* (2007b).

construct that can be found from the configuration of the magnetic field at each time step and can be used to help connect the photospheric and heliospheric positions of a given field line. Following assumptions similar to those of the PFSS model, the field is taken to be essentially radial both at the photosphere and at some distance away from the photosphere and varies only tangentially to the radial component, $B_r(\theta, \phi)$. As the field lines relax toward equilibrium they expand as a single, coherent fluid with no inherent shear motions. Without shear motions, which would tend to increase the magnetic helicity, each field line will remain next to its neighbor. In the model, the current sheet acts as a boundary through which no flux can cross, and its location and shape are projected onto the initial sphere and kept fixed in position. With these assumptions, the displacement of the field lines from the original location to their equilibrium position is unique, independent of how one executes the expansion.

The expansion velocity $\mathbf{u}_\perp$ is always normal to the radial direction. The require-

ment of no shear motion can be expressed mathematically as

$$\nabla \times \mathbf{u}_\perp = 0. \tag{3.1}$$

When the magnetic flux reaches pressure equilibrium, no further motions occur. This sets a constraint on the expansion velocity:

$$\text{when } \nabla_\perp B_r(\theta, \phi) = 0 \text{ there must be } \mathbf{u}_\perp = 0.$$

This constraint leads to a relationship between $\mathbf{u}_\perp$ and the radial component of $\mathbf{B}$:

$$\mathbf{u}_\perp = -\xi \frac{\nabla_\perp B_r}{B_r}. \tag{3.2}$$

Here ξ is a constant coefficient characterizing the relation between $\mathbf{u}_\perp$ and B_r. It describes the speed at which mathematical diffusion takes place, and since ξ does not describe a physical diffusion, its value is arbitrary (see Appendix A for a more detailed analysis). Notice that when Equation 3.2 is substituted into Equation 3.1, the requirement of no shear motion is fulfilled:

$$\nabla \times \mathbf{u}_\perp = -\xi \frac{\nabla \times \nabla_\perp B_r}{B_r} + \frac{\xi}{B_r^2} \nabla_\perp B_r \times \nabla_\perp B_r - \frac{1}{B_r} \nabla \xi \times \nabla_\perp B_r = 0. \tag{3.3}$$

The ideal MHD induction equation, which includes the contributions of currents, can be found from Equation 2.7. The length scale is large enough in ideal MHD that the convective term dominates over the resistive diffusion term, so the plasma can be assumed to be perfectly conducting ($\sigma \to \infty$) and the effects of resistive diffusion can be neglected. The ideal MHD equation is

$$\frac{\partial \mathbf{B}}{\partial t} = \nabla \times (\mathbf{u} \times \mathbf{B}), \tag{3.4}$$

which can be restated from its usual form using vector identities:

$$\frac{\partial B}{\partial t} = -\nabla \cdot (\mathbf{uB}) + (\mathbf{B} \cdot \nabla)\,\mathbf{u} + \mathbf{u}\,(\nabla \cdot \mathbf{B})\,. \tag{3.5}$$

The magnetic field does not diverge, as shown by Equation 2.1c, so the third term on the right vanishes. Only the radial component of $\mathbf{B}$ is of concern here, and the expansion velocity has no radial dependence, so the second term on the right also vanishes. The equation now becomes

$$\frac{\partial B_r}{\partial t} = -\nabla_\perp \cdot (\mathbf{u}_\perp B_r)\,, \tag{3.6}$$

where the '$\perp$' subscript refers to the azimuthal and polar coordinates, perpendicular to the radial direction. The relation for $\mathbf{u}_\perp$ from Equation 3.2 can now be substituted into Equation 3.6:

$$\frac{\partial B_r}{\partial t} = -\nabla_\perp \cdot \left[\left(-\xi \frac{\nabla_\perp B_r}{B_r}\right) B_r\right], \tag{3.7}$$

$$\frac{\partial B_r}{\partial t} = -\nabla_\perp \cdot (\xi \nabla_\perp B_r)\,. \tag{3.8}$$

If ξ is taken to be constant, the result is a diffusion equation that describes the evolution of the magnetic flux:

$$\frac{\partial B_r}{\partial t} = \xi \nabla_\perp^2 B_r. \tag{3.9}$$

The problem is set up on the spherical surface surrounded by the current sheet, whose location and shape are projected onto the surface. The magnetic flux is assumed not to diffuse across the current sheet, i.e., $\nabla_\perp B_r(\theta, \phi) = 0$ at the current sheet. The initial conditions require $B_r(\theta, \phi)$ to be assigned at $t = 0$, with concentrations of open flux stipulated by PFSS model footpoints, or any other method that can

predict the locations of open flux. All closed flux regions can be assigned a negligible flux of proper heliospheric polarity, or flux in any other general configuration. With this initial setup Equation 3.9 can be solved.

Equation 3.9 will take any initial configuration of magnetic flux and relax the concentrations of field lines until they are in equilibrium. At each time step, the expansion velocity field $\mathbf{u}_\perp$ can be calculated from Equation 3.2 and the total displacement of each field line can be determined using

$$\mathbf{d} = \int_0^\infty \mathbf{u}_\perp dt. \tag{3.10}$$

The total displacement, $\mathbf{d}\,(\theta, \phi)$, is the displacement from the initial configuration to the final configuration, where the field is uniform. To see a more conceptual representation of how the photosphere would connect to the heliosphere, simply map the $\mathbf{u}_\perp$ at each time step onto successively incrementing radial shells and interpolate between them. Once the relaxation technique has reached equilibrium, the final location of the open flux will be attained. This technique makes no predictions as to the polarity of the field or the radial distance required to reach equilibrium. The displacement defined in Equation 3.10 should not be interpreted as a trace of the physical path of a field line. Rather, it is a convenient method of finding the locations of equilibrated field lines in the heliosphere and linking them to their starting points on the solar surface.

3.3 Applications for PFSS Models

This mapping technique is best illustrated with an example of a solar magnetic field that has all of the open flux footpoints located in the polar regions (Figure 3.3), consistent with PFSS models during solar minimum. With this layout as the initial configuration and using the boundary conditions as described above, the relaxation

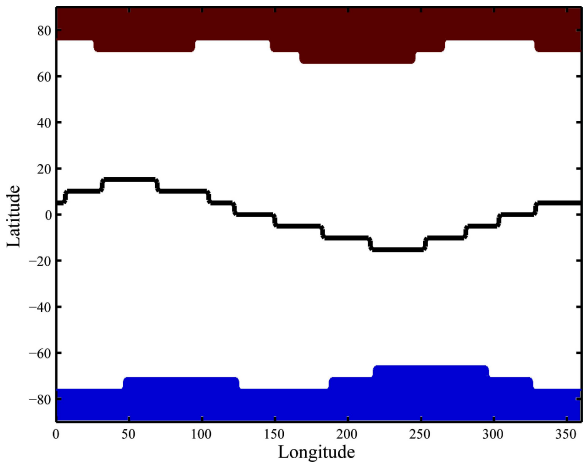

Figure 3.3: Sample initial configuration of the open photospheric magnetic field. Concentrations of open flux are located in the regions surrounding the poles, and the location and shape of the current sheet is projected onto the solar surface, where all open flux is assumed to be radial. Figure from *Gilbert et al.* (2007b).

technique can be applied until the field reaches equilibrium.

The diffusion is carried out according to Equation 3.9 on a sphere of $r = R_{\odot}$ using the numerical scheme described in Appendix A. The magnetic field diffuses in all directions along the surface of the sphere, with the Neumann boundary condition that there is no diffusion across the current sheet. Once the relaxation is complete, the expansion velocities are calculated using Equation 3.2, and the displacement is mapped onto a radially expanding surface using Equation 3.10, with each time step mapping onto a successively larger radial surface. For a three-dimensional display of the mapping, it is necessary to assign a radial component to the expansion velocity, since the diffusion is only occurring in two dimensions. This component can be obtained by choosing a radial step size and dividing by the size of the time step. Since this technique does not determine the radial distance for which equilibrium is achieved (the diffusion takes place on a unit sphere), the radial step size can be arbitrarily chosen. The result of this sample mapping technique can be seen in Figure 3.4. It should be remembered that these are not traces of the actual magnetic field line, but merely a mathematical mapping that connects the physical starting point on the solar

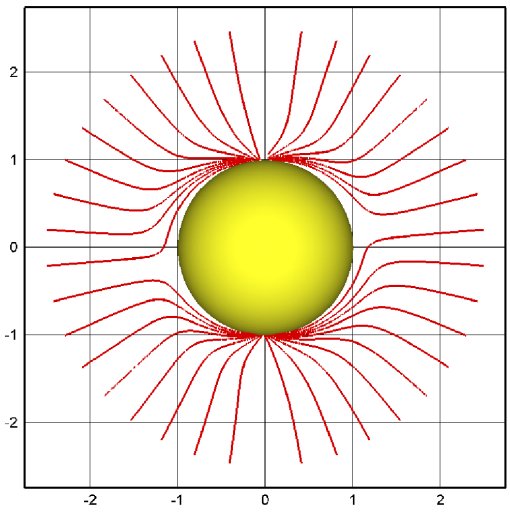

Figure 3.4: Expansion of the sample case shown in Figure 3.3. The open flux relaxes to a state in which the field lines are evenly distributed in latitude, with the current sheet as a boundary. The starting and ending points of each line represent physical locations in the heliosphere, and the line traced between them is a mathematical construct. No predictions are made as to the radial position of equilibrium, but for comparison the mapping is scaled to fit within 2.5 $R_\odot$. Figure from *Gilbert et al.* (2007b).

surface to its equilibrated physical location in the heliosphere. Nothing between those two endpoints has any physical significance in this model, so the field line "traces" in that region cannot be used to interpret observed phenomena, such as coronal loop structures, coronal waves, etc. Although no specification is made as to the radial distance that equilibrium is achieved, the latitudinal and longitudinal locations at the final equilibrium position are rigorously calculated.

The PFSS model has proven useful for finding the location and shape of the heliospheric current sheet and the locations of open flux concentrations on the solar surface (*Hoeksema and Suess*, 1990). For this reason, it will be used as an example of a possible input to the new mapping technique. Because of its limitations, however, the PFSS model cannot produce the latitudinally independent field configuration observed by *Ulysses*. For purposes of illustration, Carrington rotations (CRs) 1911 (solar minimum) and 1964 (solar maximum) were used.

A comparison is shown between a standard PFSS model and one that is modified by the Diffusive Equilibrium Mapping technique in Figure 3.5 for data taken during solar minimum (CR 1911). The standard model used here is the PFSS routine from the Wang-Sheeley-Arge (WSA) model (*Arge et al.*, 2004) using data from the Mount Wilson Solar Observatory. In this model, a 2.5° x 2.5° grid resolution was used with spherical harmonics truncated above multipole $l = 72$. For all comparisons in this study, the open flux footpoints from the PFSS model were used as starting points for the new mapping technique. Although the technique makes no determination of the radial distance in which equilibrium is obtained, the results were scaled to use a value of 2.5 $R_{\odot}$ for the purpose of comparing with the potential field model's source surface. When starting from the same endpoint in the heliosphere and tracing back to the photosphere, the two different techniques give different footpoint locations, as shown in Figure 3.5(a). Using the same footpoints on the Sun, field lines also were traced into the heliosphere using both models. It can be seen in Figure 3.5(b) that in the new technique the forces of magnetic pressure cause the concentrations of open photospheric flux to expand much more broadly in the heliosphere than a PFSS model predicts. The relaxed field lines map to different locations in the heliosphere than those predicted by the PFSS model, which will lead to a different set of expansion factors.

Magnetic expansion factors are a measure of the divergence of a flux tube from its photospheric source into the corona. These factors are calculated by taking the ratio of field strengths at the photosphere and the source surface, as traced along a field line (*Levine et al.*, 1977; *Wang and Sheeley*, 1990). There have been many studies performed in recent years to test the empirical relationship between expansion factors and solar wind speed, and the results have shown varying degrees of success (e.g., *Arge et al.*, 2004; *Whang et al.*, 2005). However, the use of magnetic expansion factors does not always lead to accurate predictions of solar wind speeds, as pointed out in the

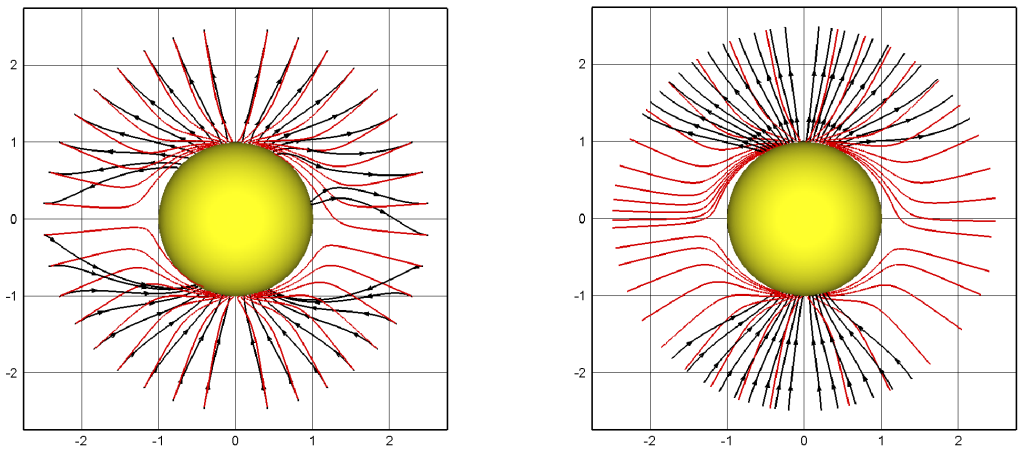

(a) (b)

Figure 3.5: Comparison between the PFSS model (*black*) and the new mapping technique (*red*) for CR 1911. Only the endpoints of the field lines in this model should be interpreted as physically significant. When starting (a) from the same endpoint in the heliosphere and tracing back to the photosphere or (b) from the same footpoints on the Sun and mapping to the heliosphere, it is clear that the two models are quite different. When the influence of magnetic pressure is explicitly taken into account, the concentrations of open photospheric flux expand much more broadly in the heliosphere than a PFSS model predicts. Figure from *Gilbert et al.* (2007b).

investigation of *Poduval and Zhao* (2004). An equilibrated field, such as that detected by *Ulysses* and mapped in this model, will lead to calculated expansion factors that do not vary greatly in latitude, which vitiates the apparent inverse relation to solar wind speed.

3.4 Generalized Applications

The most important strength of the Diffusive Equilibrium Mapping technique is its applicability to generalized field conditions. For example, it can be applied to any field configuration, including ones that allow for open flux outside of coronal holes and active region coronal holes (*Fisk et al.*, 1998; *Zurbuchen et al.*, 2000; *Woo et al.*, 2004; *Neugebauer et al.*, 2002); field structures that are hereafter referred to as

"distributed flux." Many of these models are motivated by the observed characteristic differences between coronal hole and streamer wind. It has been suggested that this can be understood in the context of a component of open flux which evolves in a transient fashion, and is not located in open flux regions commonly predicted by PFSS calculations (e.g., *Luhmann et al.*, 2002; *Neugebauer et al.*, 2002). The existence of such open flux will affect the heliospheric location of coronal hole boundaries, since their solid angle expansion will be restricted. Such an evolutionary open magnetic flux component has been very difficult to treat using PFSS and MHD models. It will lead to currents, which are forbidden in the first method. The latter method requires the use of time-dependent models that can treat interactions of open and closed flux. Such models are numerically challenging, but progress is being made (see *Lionello et al.*, 2005). To include the contributions of distributed flux, its magnitude can be found by subtracting the amount of open flux predicted by the input model from the total open flux determined in the heliosphere. The PFSS model does not account for distributed open flux, but its existence has been discussed previously (e.g., *Fisk*, 2005).

The existence of distributed open flux in areas of the Sun dominated by large, closed magnetic loops will affect the expansion of open flux concentrations, as illustrated in the test case shown in Figure 3.6. In this example, the locations of open flux concentrations (*red*) are the same as displayed in Figure 3.3, while additional open flux (*blue*) was distributed smoothly and uniformly around the remaining surface of the Sun. After relaxing to equilibrium, the additional open flux results in coronal hole boundaries located at higher latitudes than they were in Figure 3.4, where no open flux was added. This has important implications in solar wind theory: streamer wind detected at low latitudes would be frozen-in to field lines that map to areas of distributed flux, rather than the boundaries of the open flux concentrations at the poles. When comparing the two cases, it is clear that this extra flux will lead to a

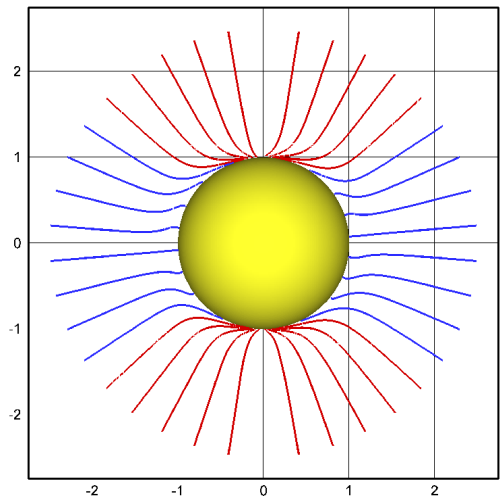

Figure 3.6: Mapping of field lines for the test case shown in Figure 3.3, with distributed open flux (*blue*) spread uniformly outside of the polar concentrations (*red*). The existence of open flux in these outer regions will have an effect on the heliospheric locations of coronal hole boundaries, which are pushed to higher latitudes. Streamer wind detected at low latitudes would be frozen-in to field lines that map to areas of distributed flux. Figure from *Gilbert et al.* (2007b).

measurable difference in the locations of coronal hole boundaries.

If in situ measurements are made of a coronal hole boundary in the heliosphere (e.g., by differences in composition or other dynamic properties of the solar wind) and the footpoints of this coronal hole boundary are located on the solar surface, then the amount of distributed open flux can be determined using this mapping technique. By adjusting the amount of open flux added on the photosphere in "closed" regions, the relaxation technique can be fine-tuned until the modeled coronal hole boundaries match the locations observed in the heliosphere.

A demonstration of this type of application is shown in Figures 3.7–3.9. The locations of open flux footpoints on the photosphere, as determined by the WSA–PFSS model for CR 1964, are given in Figure 3.7. Blue and red contour lines indicate negative and positive magnetic polarity, respectively. Without the addition of any distributed flux in areas outside of these open regions, the flux tubes will expand

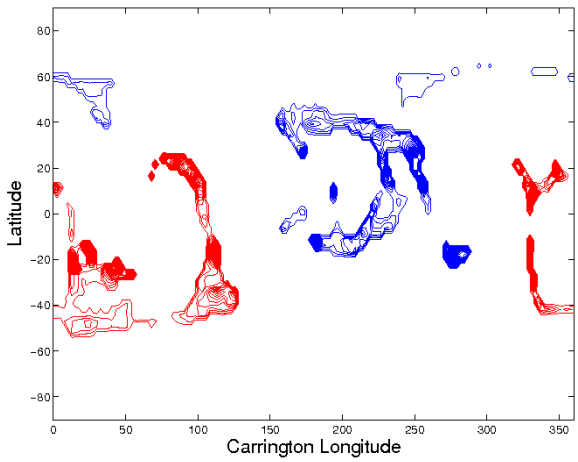

Figure 3.7: Photospheric configuration of open magnetic flux for CR 1964, as determined by the WSA–PFSS model. Red contour lines indicate positive (outward) magnetic polarity. Figure from *Gilbert et al.* (2007b).

in solid angle until their boundaries approach each other and, where the tubes have opposing polarities, form the heliospheric current sheet. Such is the case in a standard potential field model. If distributed flux is added, however, the expansion of the tubes is restricted and their boundaries are not allowed to reach the current sheet. Figure 3.8 shows the heliospheric location of the boundaries when a certain percentage of the total open flux is distributed uniformly in "closed" regions, the amount and polarity of which are given in the contour labels.

Figure 3.9 shows the case in which initial conditions consisted of distributed open flux as 70% of the total open flux on the photosphere. Overlaid on these relaxed heliospheric boundaries is a collection of solar wind data from the *Advanced Composition Explorer (ACE)* (near the equator) and *Ulysses* spacecraft, with trajectories shown in black. All measurements were taken along the spacecraft trajectories, but the color bars were drawn above and below the trajectories for display purposes. The green and orange vertical lines indicate streamer and coronal hole wind, respectively, separated at a speed of 450 km s^{-1}. The yellow vertical lines indicate detection of a CME (*Zhao and Zurbuchen*, 2008). In general, it is expected that the coronal holes would be sending out coronal hole wind and that the streamer wind would be

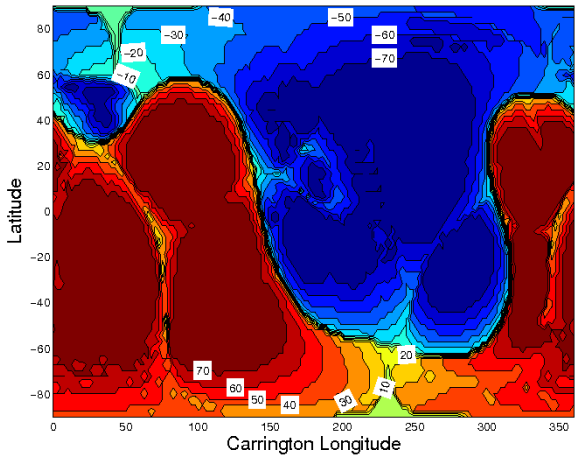

Figure 3.8: Open magnetic flux from Figure 3.7, mapped into the heliosphere. The contours indicate where the boundaries stopped expanding for different degrees of initial distributed flux. The contour labels indicate the percentage and the polarity of total open flux that was located in distributed flux regions. More distributed flux outside of coronal holes on the photosphere will result in smaller coronal holes in the heliosphere. Figure from *Gilbert et al.* (2007b).

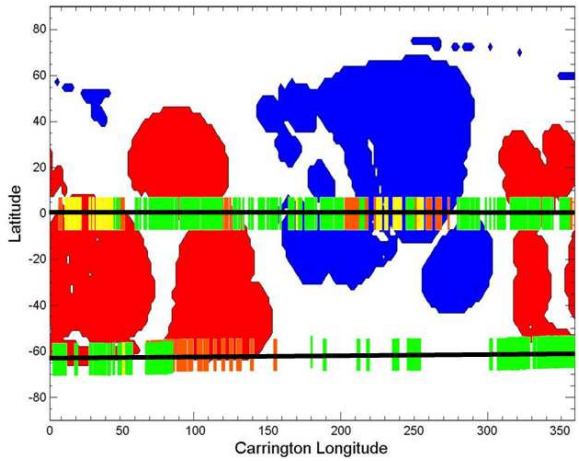

Figure 3.9: Solar wind data from *ACE* and *Ulysses* plotted over simulated heliospheric coronal hole boundaries. Spacecraft trajectories are shown in black, with the field polarity marked below as negative (*blue*) and positive (*red*). In this simulation, 70% of the total photospheric open flux was distributed in regions outside of coronal holes, thus inhibiting the expansion of the coronal hole boundaries. Plasma measurements are shown above the black lines as coronal hole wind (*orange*), streamer wind (*green*) and CME plasma (*yellow*). Figure from *Gilbert et al.* (2007b).

found outside of coronal holes, surrounding the boundary between positive and negative magnetic flux. If one adheres to the theory that the streamer wind is carrying out frozen-in distributed flux, one could fine-tune the amount of distributed flux in the initial configuration until the observed boundaries between streamer and coronal hole wind matched with the modeled coronal hole boundaries, thus quantifying the amount of distributed flux that these theories would require to match observations. As with all models, the final results will depend on the information given as input, so care should be taken when computing the initial footpoints of open flux. Both the quality and resolution of the input data will have a significant effect on the final result.

In Figure 3.9, it appears from the observations that streamer wind is, in some areas, coming from regions of strong photospheric open flux concentrations. One would expect that coronal hole wind would be coming from these coronal holes. This discrepancy illustrates that there are other processes taking place which are overlooked in this simple demonstration. It should be mentioned that for this example, no distinction was made between open flux originating from polar coronal holes and open flux coming from active regions; all was classified as flux that releases the coronal hole wind. Active region open flux has been investigated as one possible source of streamer wind (*Gosling et al.*, 1981; *Neugebauer et al.*, 2002), and thus should be differentiated from coronal hole flux for a more thorough study. It should also be noted that there are large discrepancies between the open flux footpoints predicted by models overall and the observed coronal holes (in terms of emission in the corona) during the general time of solar maximum used here (*de Toma et al.*, 2005). To quantify the amount of distributed flux on the photosphere, care must be taken to find Carrington rotations in which the data are more reliable and where the models used to locate footpoints are more in agreement with coronal observations.

Also ignored in this model are the detailed effects of reconnection, including in-

terchange reconnection (*Crooker et al.*, 2002). It is assumed that the open flux concentrations on the photosphere expand over the top of distributed open flux and that the flux does not reconnect with underlying loops. This expansion is consistent with solar wind observations, where the solar wind from coronal holes is uniformly fast and has charge states that reflect the cool, small loops at the coronal hole base (*Geiss et al.*, 1995b; *Schrijver et al.*, 1998; *Feldman et al.*, 2005). Another consequence of this picture is that the open flux from regions outside of coronal holes will be bent considerably as it emerges, due to the force of over-arching coronal hole flux. Such bends may not persist, and interchange reconnection or canopy diffusion with underlying loops will cause the distributed open flux to become radial in the locations not covered by a coronal hole flux canopy. The heliospheric locations of this distributed open flux will still be the same as those predicted by the Diffusive Equilibrium Mapping technique, but the reconnections near the Sun will cause the photospheric footpoints to change their locations from their original positions to ones located radially beneath the heliospheric locations. There will, of course, be a degree of uncertainty in the exact photospheric location of a footpoint, constrained by the size of the coronal loop with which the field line has reconnected. Further explanation of this purely radial component of distributed open flux can be found in the paper by *Fisk and Zurbuchen* (2006).

This discussion also omits time-dependent effects, such as the motions due to differential rotation and large-scale diffusion, as they are considered to be slower than the velocities required to equilibrate the magnetic field. Indeed, since the velocities that cause equilibrium result from a frame change, they can be made arbitrarily large. Physically, the field is in equilibrium and the velocities due to differential rotation and actual diffusion are superimposed on the equilibrium position.

3.5 Conclusions

Shown here is a new method to trace open magnetic field lines from the photosphere to the heliosphere. Solar wind measurements have provided requirements and constraints that any physics-based model must be able to address. This mapping technique assumes boundary values consistent with heliospheric observations in that the open flux is pressure balanced, and hence the radial component of the heliospheric field is latitudinally independent.

Open flux that relaxes to equilibrium in the model eliminates the need for current-free conditions or on an arbitrary outer boundary, such as a source surface. When compared to a standard PFSS model, there are significant differences in the final locations of coronal hole boundaries. Expansion factors calculated using a uniform field at the outer boundary will have little variation with latitude, so the apparent inverse relation to solar wind speed is not present.

Locations of endpoints in the heliosphere are rigorously calculated in this method, so it can be used as a correction to standard PFSS models to give an equilibrated mapping of the endpoints of magnetic field lines in the heliosphere. If a measurement of a coronal hole boundary were made in the heliosphere, this technique could be used to determine the amount of expansion required to put the boundary at that location and to determine if any distributed open flux exists that will affect the expansion.

A strength of this mapping technique is that it is general enough to be applied to any configuration of photospheric open flux, including one that incorporates distributed open flux — flux located in areas of the Sun that are predicted to be fully closed by many current models. The amount of distributed open flux will have an effect on the heliospheric locations of coronal hole boundaries. Distributed flux can be added at the input of the model and the magnitude fine-tuned until the modeled boundaries match with observed solar wind boundaries. The addition of distributed flux is constrained only by the total amount of open flux detected in the heliosphere.

If the streamer wind comes from regions that contain distributed open flux then there must be a substantial percentage of the total flux located in these areas, perhaps over 50% of the total photospheric open flux at solar maximum.

Regarding the limitations of a static model such as this one: to accurately determine the source regions of the streamer wind, factors other than magnetic field magnitude, such as elemental composition (including the FIP effect), charge state composition, and reconnection must be taken into account (*von Steiger et al.*, 2000; *Geiss et al.*, 1995b; *Fisk*, 2003; *Neugebauer et al.*, 2002; *Fisk and Schwadron*, 2001a). This technique provides a useful tool for the mapping of particles that should be used in conjunction with appropriate measurement techniques, as discussed in Chapter IV.

CHAPTER IV

Ion Mass Spectrometry

4.1 Introduction

In the constant battle for improved knowledge of the heliosphere, one of the most powerful arsenals of space plasma physics is that of mass spectrometers. These instruments are often unique designs, planned and tested over a period of years before being sent on missions to the far reaches of space. While mass spectrometry is a broad area with many applications in other fields (chemistry, geology, and medicine to name a few), this chapter will touch on the main points of mass spectrometry as it applies to space applications. A brief overview of charged-particle optics and how it relates to the design of electrostatic analyzers (ESAs) (§ 4.2.1), which sort particles by their energy-per-charge (E/q), is followed by a discussion of time-of-flight (TOF) analyzers (§ 4.2.2), which are used to find a particle's mass-per-charge (m/q). A few examples of analyzers that have successfully been developed and flown in space are reviewed in § 4.3. An instrument's ability to gather and measure particles is specified by measures of performance such as the geometrical factor and the geometric duty cycle (§ 4.4). Previous space instruments have provided a wealth of information concerning the heliospheric environment. New discoveries often lead to new questions and provide opportunities to advance mass spectrometry in space (§ 4.5).

4.2 Charged-Particle Optics

4.2.1 Electrostatic Deflection

An ESA is designed to take advantage of the physics of charged-particle optics. In the absence of magnetic fields ($\mathbf{B} = 0$), an ion in an electrostatic field will experience a deflection, or "refraction", whose radius of curvature is proportional to the ion's E/q. The force experienced by an ion in an electrostatic field is the Lorentz force (2.3), which accelerates the ion in a direction parallel to the field. The force will change the direction of the ion's trajectory until it is either parallel or anti-parallel to the electric field, depending on whether the ion has a positive or negative charge, respectively. An ion with a velocity perpendicular to an electric field will undergo centripetal motion and deflect in a curved trajectory with an electrostatic radius of refraction found by equating a centripetal force $\mathbf{F_c}$ (4.1) to the Lorentz force (2.3).

$$\mathbf{F_c} = m\mathbf{a} = \frac{m\left(v\sin\theta\right)^2}{r}\left\langle-\hat{\mathbf{r}}\right\rangle \tag{4.1}$$

$$\frac{m\left(v\sin\theta\right)^2}{r}\left\langle-\hat{\mathbf{r}}\right\rangle = q\mathbf{E} \tag{4.2}$$

$$\Rightarrow r = \frac{m\left(v\sin\theta\right)^2}{q\left|\mathbf{E}\right|}$$

$$\Rightarrow r = \frac{2}{|\mathbf{E}|}\frac{E}{q}\sin^2\theta \tag{4.3}$$

The angle between the electric field $\mathbf{E}$ and the ion's velocity $\mathbf{v}$ is represented here by θ. When the ion is traveling parallel to the electric field (i.e., $\theta = 0$) there is no centripetal force and the ion travels in a straight line, accelerated by the Lorentz force. When the velocity of the ion is perpendicular to $\mathbf{E}$ (i.e., $\theta = \pi/2$), the ion will experience pure centripetal motion. Equation 4.3 states mathematically that the radius of refraction becomes larger with increasing E/q, and smaller as the strength of the electric field $|\mathbf{E}|$ increases.

A simplified illustration of the radius of refraction for charged particles is given

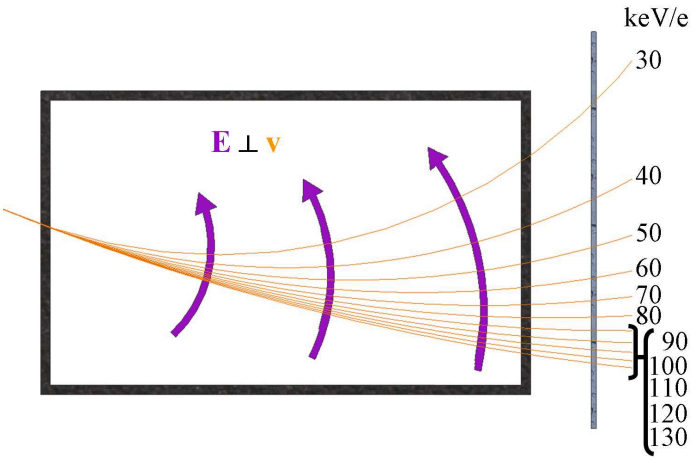

Figure 4.1: An example of the radius of refraction for charged particles. Ions passing through an electric field, with $\mathbf{E} \perp \mathbf{v}$ everywhere, will be deflected with a radius given by Equation 4.3. The trajectories of ions with the same initial position and entrance angle, but different E/q values, are drawn here as circles of varying radii. Note the non-uniform spread in exit trajectories due to the alignment of circles with a common tangent.

in Figure 4.1. As ions pass through the electrostatic field, their trajectories become curved. If $\mathbf{E}$ is perpendicular to the velocity at all times ($\theta = \pi/2$), the ion will travel in a circular track with a radius given by Equation 4.3. Traces of the trajectories for ions with increasing E/q values are shown, with all ions having the same entrance angle and initial position at the left of the figure. The electric field is approximated to be perpendicular to the ion trajectories at all points. When the ions exit the field and arrive at a detector, drawn as a vertical line on the right, their positions are spread out unevenly. After examining the illustration it becomes clear that the spacing is due to the alignment of circles that share a common tangent.

In general, ion optics instruments have complicated geometries with electrostatic fields that change in strength and direction throughout the instrument. That, along with the effects of fringe fields near the edges of charged deflection plates, will cause the radius of refraction to gradually change as the ion travels through the instrument. Such scenarios are difficult to calculate analytically, but ion optics simulation

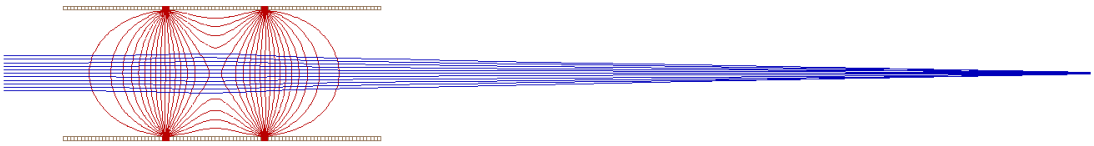

Figure 4.2: Simulation of an Einzel lens using SIMION. The contours of electrostatic potential are shown in red, the ion trajectories in blue, and the charged deflection plates in gray.

programs can help reveal how ions will behave. The program used for this research is SIMION 3D, version 7.0, developed by the Idaho National Engineering and Environmental Laboratory (*Dahl*, 2000). Using the design and voltage settings for a given instrument as boundary conditions, SIMION solves the Laplace equation (2.11) using finite difference methods to calculate the electrostatic potential throughout the simulation volume. To find the trajectory of an ion, SIMION computes the forces acting on it and uses them to determine the ion's acceleration. These parameters lead to a prediction of the ion's position and velocity at the next time step, the size of which is continually adjusted to maximize accuracy while minimizing the number of integration steps per trajectory (*Dahl*, 2000). An example is the SIMION simulation of an Einzel lens (Figure 4.2), which was used in the experiments detailed in Chapters V and VI. The electrostatic potential contours are shown in red, the ion trajectories shown in blue, and the charged deflection plates are shown in gray.

The ESA sorts charged particles by their E/q with the use of static electric fields generated by charged deflection plates. With specific geometries and voltage settings, a target E/q species can be guided through the ESA and into the next section of the instrument. The voltages on the ESA's charged deflection plates can be adjusted to allow particles with different E/q values to pass through the analyzer. In combination with a TOF system (§ 4.2.2) the ESA can be used for a more complete analysis of ions.

4.2.2 Time of Flight

There are several different types of analyzers used for recording the flight time of particles (e.g., *Hamilton et al.*, 1990; *McComas and Nordholt*, 1990; *Gloeckler et al.*, 1992). Two types that are related to instruments discussed in this dissertation are the linear triple-coincidence TOF and the cylindrically symmetric linear-electric-field (LEF) TOF. The former include analyzers such as the design employed on the Charge-Energy-Mass (CHEM) sensor (*Gloeckler et al.*, 1985), SWICS (*Gloeckler et al.*, 1992), the Suprathermal Ion Composition Spectrometer (STICS) (*Gloeckler et al.*, 1995), and the Charge-Energy-Mass Spectrometer (CHEMS) (*Krimigis et al.*, 2004). The latter include analyzers such as the Ion Mass Spectrometer (IMS) (*Young et al.*, 2004b) and the Plasma Experiment for Planetary Exploration (PEPE) (*Young et al.*, 2007).

TOF analyzers measure the time t that it takes the ion to travel a certain distance. If a solid-state detector (SSD) is used to detect the ions at the end of the TOF measurement, the residual energy $E_{\rm res}$ of the ion can also be measured. These quantities can be used to find the ion's mass m, charge state q, and initial energy E, as shown in Equations 4.4–4.8.

$$m = 2\left(\frac{t}{d}\right)^2\left(\frac{E_{\rm res}}{\alpha}\right) \quad \text{(amu)} \tag{4.4}$$

$$\frac{m}{q} = 2\left(\frac{t}{d}\right)^2\left(V_a + \frac{E_{\rm int}}{q}\right) \quad \text{(amu e}^{-1}\text{)} \tag{4.5}$$

$$q = \frac{(E_{\rm res}/\alpha)}{V_a + E_{\rm int}/q} \quad \text{(e)} \tag{4.6}$$

$$E = q\left(\frac{E}{q}\right) \quad \text{(keV)} \tag{4.7}$$

$$v_{\rm ion} = 439.3\left[(E/q)\,/\,(m/q)\right]^{1/2} \quad \text{(km s}^{-1}\text{)} \tag{4.8}$$

These equations are applicable in the first kind of TOF system mentioned above, the linear triple-coincidence TOF shown in Figure 4.3. For this type of analyzer, the

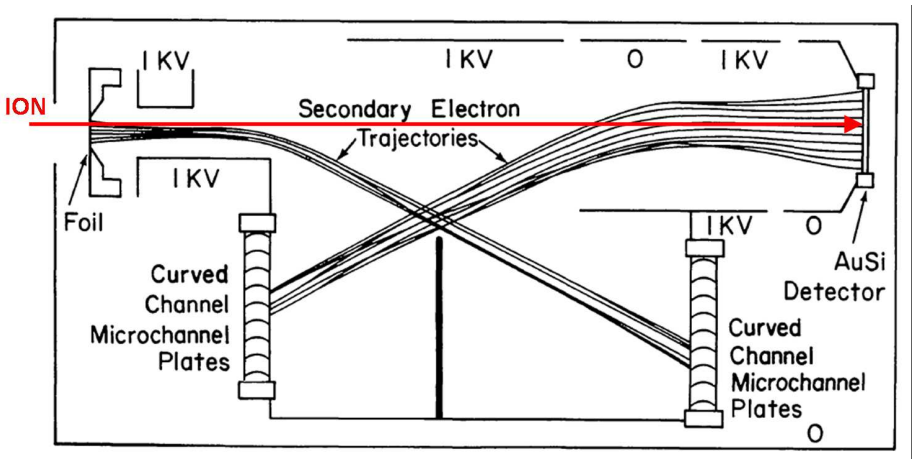

Figure 4.3: Particle trajectories through a linear triple-coincidence time-of-flight analyzer. The ion (*red*) first passes through a carbon foil, causing secondary electrons to be emitted that trigger a start signal when they impact an MCP. After traversing the TOF region, the ion impacts a detector that measures its energy and emits secondary electrons that trigger a stop signal. Figure adapted from *Gloeckler et al.* (1992).

flight time is calculated over a straight-through flight path between carbon foil and detector of distance d. The efficiency α of the SSDs, the post-acceleration voltage V_a that the ion experiences before entering the TOF region, and the energy the ion has when it is internal to the TOF telescope $E_{\rm int}$ are also included (*Gloeckler et al.*, 1992). A post-acceleration voltage is necessary in this type of system so the particles will have energy sufficient to trigger the SSD, which can have an energy threshold of ∼15–30 keV (*Gloeckler et al.*, 1992; *Wüest*, 1998).

The other type of analyzer mentioned above, cylindrically symmetric LEF TOF, is capable of making high mass resolution measurements that depend only on a particle's mass and are unaffected by any variations in the particle's energy. The theory behind cylindrically symmetric LEF TOF, also called isochronous TOF, will be summarized here, with an investigation into improvements to the design discussed in Chapter VI. Some of the first isochronous TOF analyzers to use linear electric fields in space were the V-shaped analyzers such as those used on *Wind*–High Mass Resolution Spectrometer (MASS) (*Hamilton et al.*, 1990) and the Mass Time-of-Flight (MTOF)

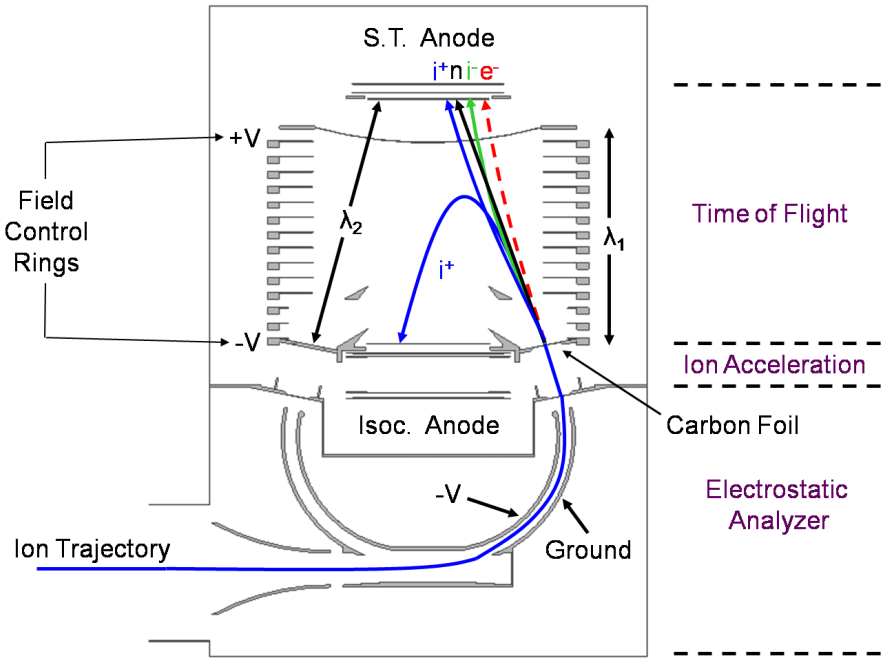

Figure 4.4: Particle trajectories through a cylindrically symmetric linear-electric-field time-of-flight analyzer. The particles and their charge states are shown here as neutrals (*black*), negative ions (*green*), and electrons (*red*) impacting the 'straight-through' anode, and positive ions (*blue*) impacting the 'isochronous' anode. Positive ions whose residual energies are below a certain threshold will undergo a harmonic oscillation with an isochronous time of flight, while particles with energies above the threshold will impact the straight-through anode.

sensor on the *SOHO/CELIAS* experiment (*Hovestadt et al.*, 1995). The isochronous technique can measure m/q to high resolution ($m/\Delta m = 100$) so a separation of isotopes is possible. The adaptation of cylindrically symmetric isochronous TOF analyzers for use with external ion sources, such as those seen by spacecraft, was described by *Managadze* (1986), and variants of the design can be found in *Möbius et al.* (1990) and *McComas and Nordholt* (1990).

A detailed description of the principles involved with the type of TOF analyzer used in this research is given by *McComas and Nordholt* (1990) and *Young et al.* (2004b). As seen in Figure 4.4, after guidance from a tophat ESA (*Carlson et al.*, 1982), an ion passes through a thin (nominal $\sim$0.5 μg cm^{-2}) carbon foil at the entrance

to the TOF cylinder. This causes electrons to be ejected from the foil and travel up to a straight-through MCP, where they trigger a start signal for the time-of-flight calculation. The ion experiences Coulomb collisions in the foil that affect its trajectory, energy, and charge state. The parameters that this particle will have once it exits the foil depend on its initial speed and species, as well as the thickness of the carbon foil itself (*Funsten et al.*, 1993a,b). The different particle charge states with their trajectories are colored in Figure 4.4 as neutral (*black*), negative ion (*green*), positive ion (*blue*), and electron (*red*). Upon exiting the foil, the particle enters the TOF region and immediately encounters an electric field, which increases linearly with distance, $|\mathbf{E}| = kz$, where z is the axial direction and k represents the electrical and geometrical properties of the analyzer. The particle travels through the TOF system and impacts one of the two microchannel plates (MCPs), triggering a stop signal for the time of flight. The Lorentz force that the ion experiences while in the TOF region, $q\mathbf{E}$, causes a positive ion's velocity to slow and eventually reverse direction following the motion of a simple harmonic oscillator. A more generalized equation can be obtained by noting that $q = \pm Z_q e$, where Z_q is the magnitude of the charge number of the ion, e is the elementary charge, and the sign is determined by the charge of the ion. The equation of motion for charged particles in a linear electric field is

$$\mathbf{F} = m\mathbf{a} = q\mathbf{E} \tag{4.9}$$

$$m\mathbf{a} = q\,|\mathbf{E}|\,(-\hat{\mathbf{z}}) \tag{4.10}$$

$$m\ddot{z} = -qkz, \tag{4.11}$$

where k can be found by integrating the electric field across the TOF region, which

has length λ_1.

$$\mathbf{E} = -\nabla\Phi \tag{4.12}$$

$$kz(-\hat{\mathbf{z}}) = -\frac{\mathrm{d}\Phi}{\mathrm{d}z}(\hat{\mathbf{z}}) \tag{4.13}$$

$$k\int_0^{\lambda_1} z\mathrm{d}z = \int_{V_1}^{V_2} \mathrm{d}\Phi \tag{4.14}$$

$$\frac{k\lambda_1^2}{2} = V_2 - V_1 = \Delta V \tag{4.15}$$

$$\Rightarrow k = \frac{2\Delta V}{\lambda_1^2} \quad (\mathrm{V\ m^{-2}}) \tag{4.16}$$

The flight times of each of these particles can be found by integrating the equation of motion (4.11) along the flight path. The particle will exit the foil with either positive, negative, or neutral charge, each with its own flight path. When a positively charged proton passes through the carbon foil, it is neutralized about 70% of the time (*Young et al.*, 2004b). For a neutral particle entering the TOF region the electric fields will have no effect, so the flight time can be found using a straightforward calculation of kinetic energy. Let E_{int} be the energy of a particle once it has passed through the carbon foil and entered the TOF region. E_{int} includes any energy gains or losses from the ion's initial energy, acceleration prior to reaching the foil, and collisions in the foil. If the path length from the carbon foil to the MCP in front of the straight-through detection anode is given by λ_2, then the time of flight t_{n} for a neutral particle of mass m can be found by Equation 4.19.

$$E_{\mathrm{int}} = \frac{1}{2}mv^2 \tag{4.17}$$

$$= \frac{1}{2}m\left(\frac{\lambda_2}{t_{\mathrm{n}}}\right)^2 \tag{4.18}$$

$$\Rightarrow t_{\mathrm{n}} = \lambda_2\sqrt{\frac{m}{2E_{\mathrm{int}}}} \quad (\mathrm{s}) \tag{4.19}$$

The fraction of particles that keep a single positive charge after passing through the foil increases with increasing energy and depends strongly on the species. In general, ions will keep a single positive charge after the foil about 10–30% of the time, and less than 2% of them will become doubly charged (*Young et al.*, 2004b). If the ion is positively charged with an E_{int}/q within the range where its trajectory can be reversed by the LEF, its time of flight can be found by solving Equation 4.11 for z.

$$m\ddot{z} = -Z_q e k z \tag{4.20}$$

$$z = \sqrt{\frac{2E_{\text{int}}}{Z_q e k}} \sin\left(\sqrt{\frac{Z_q e k}{m}} t\right) \tag{4.21}$$

$$\omega = \sqrt{\frac{Z_q e k}{m}} \quad (\text{s}^{-1}) \tag{4.22}$$

Here the amplitude of z is a function of E_{int}/q and the frequency of oscillation is characterized by ω. The ion enters the chamber and undergoes half of an oscillation before returning to the same plane, where it is used to trigger a measurement. The time $t_{\text{LEF pos}}$ required for this trajectory is equal to half of the period, and is dependent on the mass-per-charge m/q of the ion.

$$t_{\text{LEF pos}} = \frac{1}{2}\frac{2\pi}{\omega} = \pi\sqrt{\frac{m}{Z_q e k}} \quad (\text{s}) \tag{4.23}$$

A positive ion may have an E_{int}/q high enough that the LEF will slow it down but not reverse the ion's direction before it manages to strike the straight-through MCP. The time of flight for these particles $t_{\text{ST pos}}$ can be found from Equation 4.21, substituting the length of the straight-through flight path λ_2 for z.

$$t_{\text{ST pos}} = \sqrt{\frac{m}{Z_q e k}} \sin^{-1}\left(\sqrt{\frac{k\lambda_2^2}{2\left(E_{\text{int}}/Z_q e\right)}}\right) \quad (\text{s}) \tag{4.24}$$

Particles pass through the foil with a negative charge about 2% of the time (*Bürgi et al.*, 1993; *Young et al.*, 2004b). A negatively charged ion will accelerate through the LEF region with a flight time $t_{\rm neg}$ that can be found from Equation 4.11 by setting $q = -Z_q e$ and solving for t when $z = \lambda_2$.

$$z = \sqrt{\frac{E_{\rm int}}{2Z_q e k}} \left(e^{i\omega} - e^{-i\omega}\right) \quad \text{(m)} \tag{4.25}$$

$$t_{\rm neg} = \sqrt{\frac{m}{Z_q e k}} \ln \left\{ \frac{\lambda_2 \sqrt{k} + \sqrt{k\lambda_2^2 + 2E_{\rm int}/(Z_q e)}}{\sqrt{2E_{\rm int}/Z_q e}} \right\} \quad \text{(s)} \tag{4.26}$$

The preceding equations are for a simplified scenario, where a particle will encounter an unchanging linear electric field from carbon foil to MCP. More accurate calculations of flight times must take into account the travel time of electrons that trigger the start signal, and must use a combination of the above equations to describe a particle's flight both when it's in the LEF region and when it exits, moving into a region of electric field pointed in the opposite direction before reaching the straight-through MCP.

4.3 Examples of Current Instrument Design

Various types of ESA and TOF systems have been used in space, each with their own advantages. Some notable ones that led to the development of the IonSpec ESA (Chapter V) include the CHEM instrument (*Gloeckler*, 1977; *Gloeckler et al.*, 1985), which was flown on the the *Charge Composition Explorer (CCE)* spacecraft (one of three spacecraft in the *AMPTE* mission), and the SWICS instrument (*Gloeckler et al.*, 1992), versions of which can be found on board the *Ulysses*, *Wind*, and *ACE* missions. The LEF TOF system (Chapter VI) is often associated with an ESA design called the tophat (*Carlson et al.*, 1982), an example of which is found on the Cassini Plasma Spectrometer (CAPS)–IMS instrument on *Cassini* (*Young et al.*, 2004b).

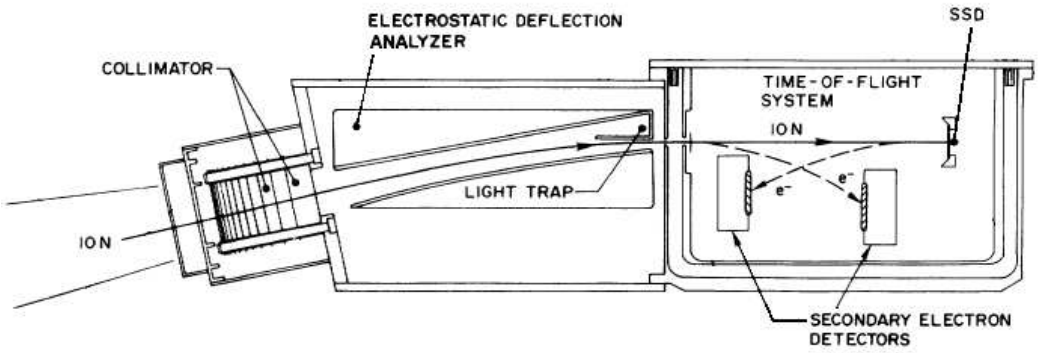

Figure 4.5: The electrostatic analyzer and time-of-flight system for the *AMPTE–CCE*–CHEM instrument. Ions pass through a collimator into the electrostatic deflection system where a particle with a specific E/q is guided to the exit slit. The ions then enter a time-of-flight system equipped with solid state detectors, allowing for a measurement of mass, charge, and energy. Figure adapted from *Gloeckler et al.* (1985).

The CHEM instrument went into space in August 1984 and was the first to combine an ESA with a time-of-flight-versus-energy system (*Gloeckler*, 1977; *Gloeckler et al.*, 1985). It had the ability to measure each of the quantities in Equations 4.4–4.8 and also the incident angle of incoming ions. CHEM explored Earth's magnetosphere and magnetosheath, measuring particles in the energy range of 0.3–315 keV/e. A schematic of the ESA and TOF of CHEM (Figure 4.5) shows a multi-slit collimator that only allows properly aimed ions into the electrostatic deflection system. Voltages are set on the deflection plates to create an electrostatic field between them, which bends the ions' trajectories so those with a specific energy-per-charge E/q can pass through an exit slit. By periodically adjusting the voltages, the entire desired energy range can be covered. Ions experience a voltage drop ($\sim$30 kV max) that accelerates them after leaving the ESA, and they traverse a triple-coincidence linear TOF system. In the TOF analyzer, an ion passes through a carbon foil, generating secondary electrons that trigger a start signal, with an energy-dependent yield of about 1–5 secondary electrons per ion (*Ritzau and Baragiola*, 1998). After traveling a distance of 10.5 cm it impacts the SSD, revealing its energy and causing other secondary electrons

to be emitted for the stop signal. The signals give the time of flight that, together with the distance traveled, allows the calculation of the ion's speed. By requiring all three detectors (the anodes behind the start and stop MCPs, and the SSD) to be triggered for a measurement to count, the background noise is reduced significantly. The 3D shape of CHEM can be visualized by rotating the image in Figure 4.5 by 40° on an axis centered in the TOF region (*Gloeckler et al.*, 1985; *Gloeckler and Hamilton*, 1987).

The SWICS instrument (Figure 4.6) is similar in design to CHEM, but is rotated about the symmetry axis by 69° and further includes a dedicated channel for protons (*Gloeckler et al.*, 1992). The first SWICS was launched on board the *Ulysses* mission in 1990, with SWICS instruments later launched on the *Wind* and *ACE* missions as well (*Gloeckler et al.*, 1995; *Stone et al.*, 1998). These instruments have provided breakthrough measurements of many particle populations, including the first measurements of most of the known interstellar and interplanetary pickup ions, and the elemental and charge state composition of the solar wind (*Kallenbach et al.*, 2000; *Wimmer-Schweingruber*, 2003). The orbit of *Ulysses* took it over the poles of the Sun, allowing for the first measurements of the polar coronal hole wind and the high-latitude magnetic field (*Forsyth et al.*, 1996). Because of the spacecraft's unique orbit out of the ecliptic plane, the *Ulysses*–SWICS instrument has had the ability to compare the coronal hole and streamer solar wind in ways not previously possible. Much of the information related to the solar wind and pickup ions discussed in Chapter II came from measurements made by SWICS.

Another type of ESA is the toroidal tophat analyzer (*Carlson et al.*, 1982), such as the IMS (Figure 4.7) and Electron Spectrometer (ELS) of the *Cassini*–CAPS instrument suite (*Young et al.*, 2004b). A tophat design offers the possibility of a full 360° polar field of view and has a large geometrical factor (*Young et al.*, 1988). Ions enter the ESA and are guided between two concentric toroidal plates. A voltage

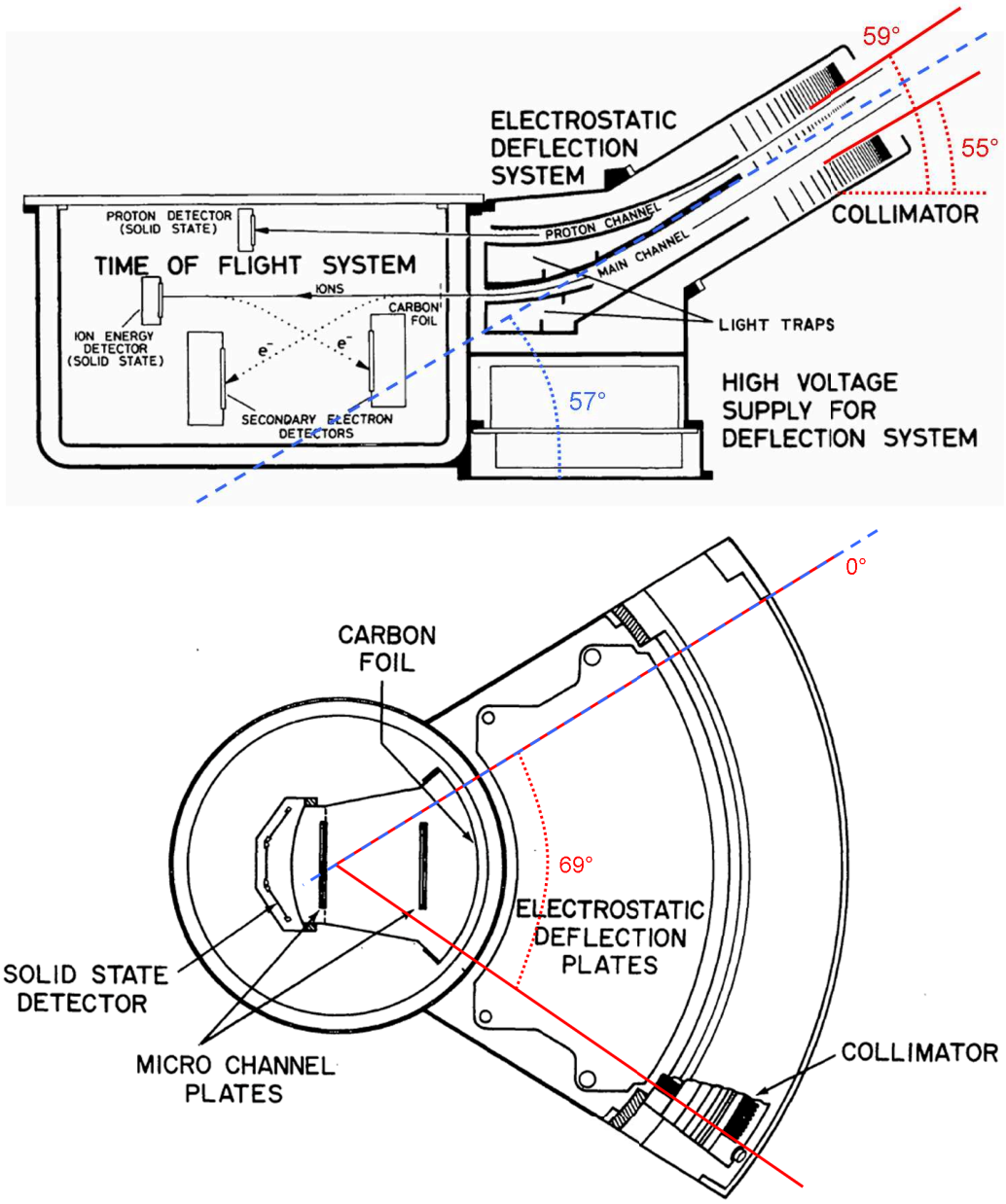

Figure 4.6: ESA and TOF systems of the SWICS instrument. The functionality is the same as for CHEM, but with the addition of a dedicated channel for protons. The collimator accepts ions that enter within the angles $55° \leq \theta \leq 59°$ and $0° \leq \phi \leq 69°$. The axis of rotation for *Ulysses*–SWICS ($\theta = 57°$, $\phi = 0°$) is shown with a blue dashed line. Side-view and top-view figures are adapted from *Gloeckler et al.* (1992).

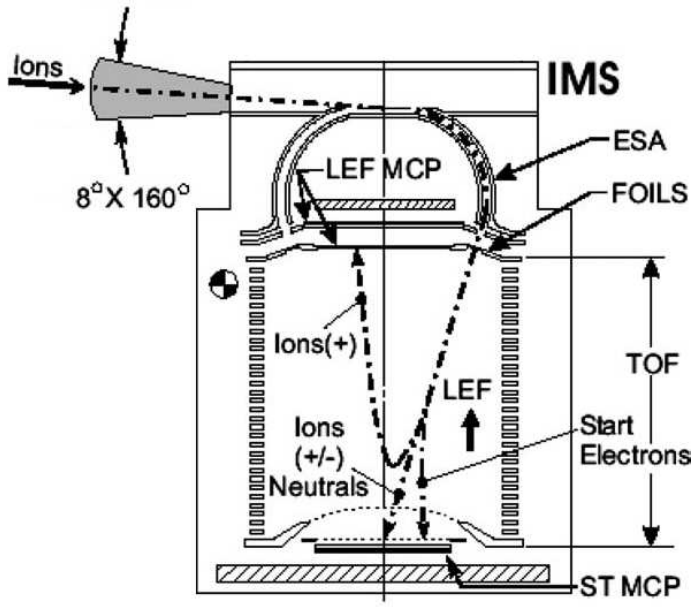

Figure 4.7: An example of a tophat ESA: the *Cassini*–CAPS IMS sensor. Along with the tophat ELS, the IMS instrument is designed to measure low-energy ($\leq$ 50 keV/e) particles emanating from Saturn, its moons, and its rings. Figure adapted from *Young et al.* (2004b).

drop across the plates allows incoming particles to be filtered, with only the desired E/q species passing all the way through. Upon exiting the ESA, the particle enters a cylindrically symmetric LEF TOF analyzer. With an energy range of 1–50 keV/e and an energy resolution of 17%, the IMS has provided new information on the plasma environment of Saturn, its moons, and its rings (*Sittler et al.*, 2006).

The FIPS instrument on the *MESSENGER* mission to Mercury has a unique, low-mass ESA design with a nearly hemispherical ($\sim$1.4π sr) instantaneous field of view (*Koehn et al.*, 2002; *Andrews et al.*, 2007), as shown in Figure 4.8. The ESA is composed of charged hemispherical plates that step through different voltage settings to deflect ions, and sets of flat collimators that improve the angular resolution and aid with rejection of ultraviolet (UV) rays. The suppression of UV light was an important consideration in the design of FIPS since it would be operating in full sunlight near Mercury. The hourglass shape of the ESA was specifically designed to allow ions to

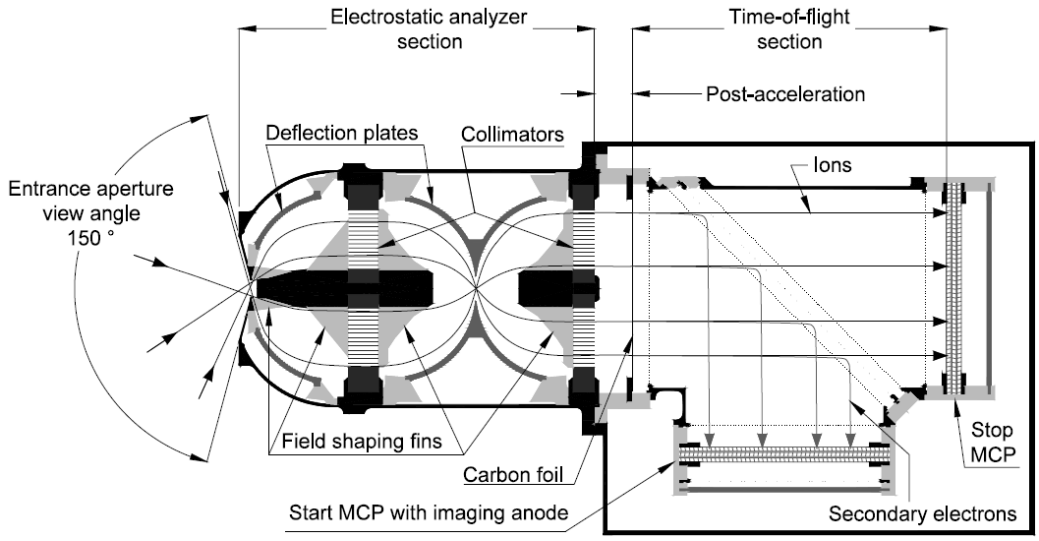

Figure 4.8: The ESA for the *MESSENGER*–FIPS instrument. Ions enter from the left and are deflected through a series of curved plates and collimators before entering the TOF section on the right. Figure from *Andrews et al.* (2007).

pass through while providing the necessary UV suppression (*Andrews et al.*, 2007).

4.4 Instrument Properties

Certain metrics are useful for characterizing and comparing the effectiveness and collecting power of particle instruments. These include the geometrical factor, which takes into account the physical shape and configuration of the instrument, and the geometric duty cycle, which is an estimate of the fraction of the time the instrument will be collecting data at a given voltage setting.

4.4.1 Geometrical Factor I

The gathering ability and sensitivity of plasma instruments can be characterized by using the energy-geometrical factor per pixel G_E , which is defined by *Funsten and*

McComas (1998) as

$$C = Dj\,\epsilon\,E_C\,G_E \quad (\text{counts s}^{-1}). \tag{4.27}$$

In Equation 4.27, C is the count rate in a pixel, D is the geometric duty cycle of the instrument, j is the differential plasma flux ($\text{cm}^{-2}\ \text{s}^{-1}\ \text{sr}^{-1}\ \text{eV}^{-1}$), ϵ is the detector efficiency, E_C is the central energy of the energy passband (eV), and G_E is given by *Gosling et al.* (1984) as

$$G_E = A_e \left\langle \Delta\alpha \frac{\Delta E}{E} \right\rangle \int_{\Delta\beta} \cos\beta\,\mathrm{d}\beta \quad (\text{cm}^2\ \text{sr}). \tag{4.28}$$

To illustrate how to find the geometrical factor for an instrument, it is useful to look at a tophat electrostatic analyzer (Figure 4.9). The area of the entrance aperture A_e is measured by its area normal to the incoming particle flux, and can be written as

$$A_e = X_0^{'} \Delta R \quad (\text{cm}^2), \tag{4.29}$$

where $X_0^{'}$ is the full width at half maximum (FWHM) of the detector's response, measured by sweeping an incident beam linearly across the aperture in the $X^{'}$ direction. It could also be approximated by using the length of the aperture, as projected on a plane normal to the incoming particle flux. The distance between the analyzer plate electrodes is given by ΔR.

If the tophat has a full 360° polar acceptance angle, then the polar angle resolution $\Delta\beta$ can be used to replace the integral in Equation 4.28 since, as pointed out by *Young et al.* (1988), the original derivation was for slit apertures rather than curved tophat apertures. The integrated azimuthal-energy response for a tophat analyzer can be approximated by assuming all of the particle trajectories between the analyzer

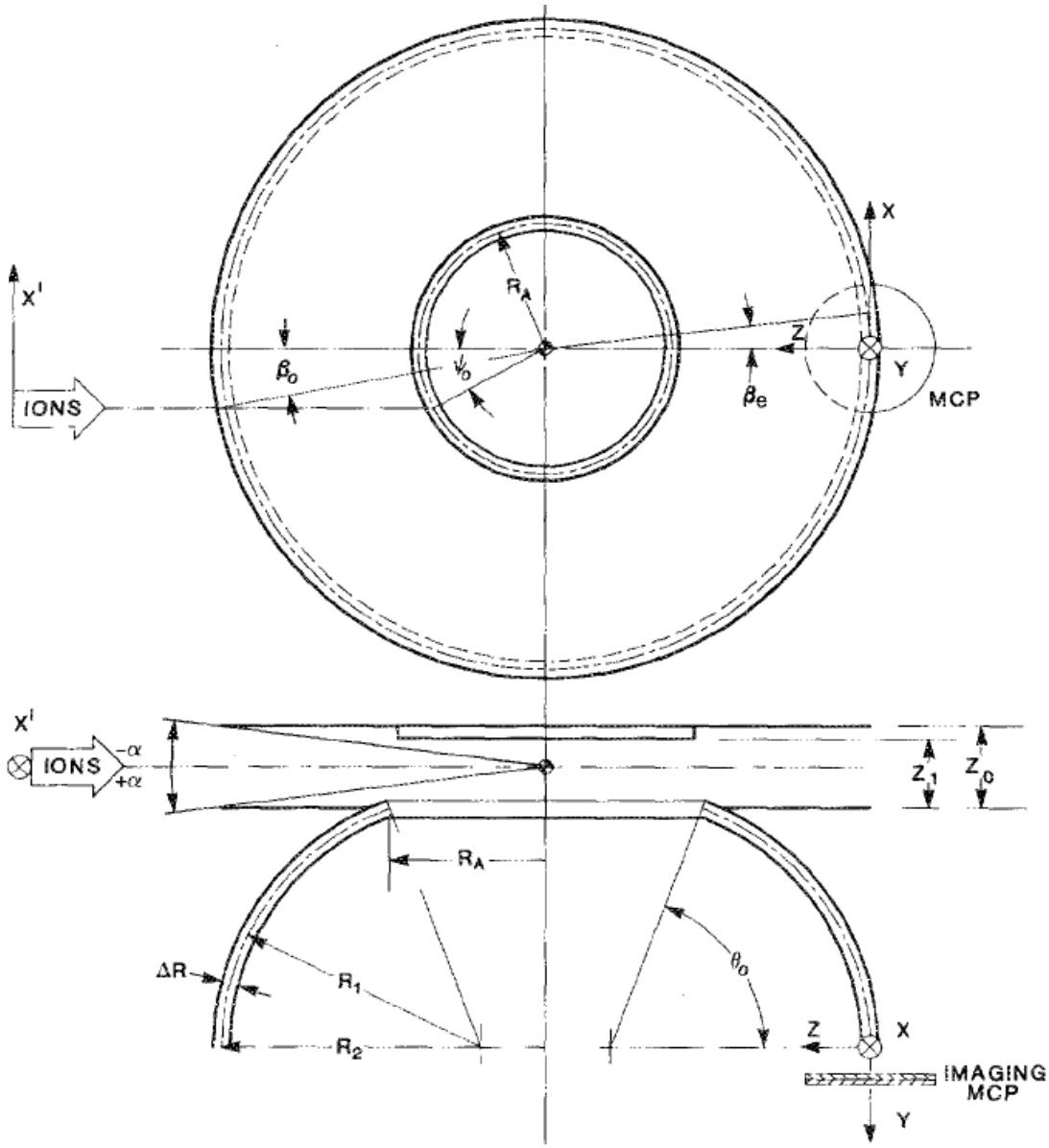

Figure 4.9: A tophat electrostatic analyzer. The azimuthal angle α, polar angle β, analyzer bending angle θ_0, and distance between analyzer plate electrodes ΔR are shown. This figure is taken from *Young et al.* (1988).

plate electrodes are perfectly circular, with 50% transmission. By averaging between two analytical approximations for the transmission, *Gosling et al.* (1978) gives the integrated azimuthal-energy response as

$$\left\langle \Delta\alpha \frac{\Delta E}{E} \right\rangle \approx \frac{\csc^3(\theta_0/2)}{4K^2} \left(\frac{7}{8} + \cos\frac{\theta_0}{2} \right) \quad \text{(rad)}. \tag{4.30}$$

Here, θ_0 is the analyzer bending angle shown in Figure 4.9 and K is the analyzer constant:

$$K = \frac{R_0}{\Delta R}, \tag{4.31}$$

where R_0 is the average radius between the inner and outer analyzer plate electrodes and is proportional to X_0'. Since $A_e \propto R_0^2/K$ and $\left\langle \Delta\alpha \frac{\Delta E}{E} \right\rangle \propto 1/K^2$, the energy-geometrical factor's dependence on the analyzer constant (*Gosling et al.*, 1984) and the average radius of the analyzer plate electrodes is:

$$G_E \propto \frac{R_0^2}{K^3}. \tag{4.32}$$

G_E is proportional to the square of the optical scaling of the instrument. By scaling a larger instrument down to a smaller version, with all proportions held constant, only the area of the entrance aperture will decrease (*Funsten and McComas*, 1998) and the analyzer constant will be left unchanged.

4.4.2 Geometrical Factor II

While Equation 4.27 can be used to find the count rate per pixel, it is useful to have a derivation in terms of physical quantities, such as the particle density n, the particle velocity $\mathbf{v}$, and the particle's thermal temperature T. These are all found in the velocity distribution function of the particle, which, for a Maxwell-Boltzmann

distribution, is written as:

$$f_{\mathbf{v}} = n\left(\frac{m}{2\pi kT}\right)^{\frac{3}{2}} e^{-\left(\frac{m(\mathbf{v}-\mathbf{u})^2}{2kT}\right)} \text{ (particles s}^3 \text{ cm}^{-6}\text{)}. \tag{4.33}$$

In Equation 4.33, m is the particle's mass, k is the Boltzmann constant, and $\mathbf{u}$ is the bulk velocity of the plasma. If the entrance aperture's area is written in vector form $\mathbf{A}$, with the direction of the vector perpendicular to the plane of the aperture, then the differential count rate dC for a small phase space volume detected by the instrument can be written as

$$\mathrm{d}C = \epsilon \mathbf{A} \cdot \mathbf{v} f \mathrm{d}v^3. \tag{4.34}$$

The velocity space can be written out in its components, leading to

$$\mathrm{d}C = \epsilon \mathbf{A} \cdot \mathbf{v} f v^2 \sin\theta_v \, \mathrm{d}\theta_v \mathrm{d}\phi_v \mathrm{d}v. \tag{4.35}$$

With the assumption that f does not change within a pixel, the angle between $\mathbf{A}$ and $\mathbf{v}$ can be written as $\angle Av$ (it may not be equal to θ_v or ϕ_v).

$$\begin{aligned} \mathrm{d}C &= \epsilon A v \cos\left(\angle Av\right) f v^2 \sin\theta_v \, \mathrm{d}\theta_v \mathrm{d}\phi_v \mathrm{d}v \\ \Rightarrow \Delta C &= \epsilon A \cos\left(\angle Av\right) f v^3 \sin\theta_v \, \Delta\theta_v \Delta\phi_v \Delta v \end{aligned} \tag{4.36}$$

The energy resolution η of the instrument can be derived by starting with the

equation for kinetic energy-per-charge:

$$\frac{E}{q} = \frac{1}{2}\frac{m}{q}v^2 \tag{4.37}$$

$$\Rightarrow \frac{\mathrm{d}\left(\frac{E}{q}\right)}{\mathrm{d}v} = \frac{m}{q}v$$

$$\Rightarrow \mathrm{d}\frac{E}{q} = \frac{m}{q}v\ \mathrm{d}v$$

$$\Rightarrow \frac{\mathrm{d}\left(\frac{E}{q}\right)}{\frac{E}{q}} = \frac{\frac{m}{q}v\ \mathrm{d}v}{\frac{1}{2}\frac{m}{q}v^2}$$

$$\Rightarrow \frac{\Delta\left(\frac{E}{q}\right)}{\frac{E}{q}} = \eta = \frac{2}{v}\Delta v \tag{4.38}$$

$$\Rightarrow \Delta v = \frac{\eta v}{2}. \tag{4.39}$$

Plugging this into Equation 4.36 gives the differential count rate per pixel:

$$\Delta C = \epsilon A \cos\left(\angle Av\right) f v^3 \sin\theta_v\ \Delta\theta_v \Delta\phi_v \frac{\eta v}{2}$$

$$\Rightarrow \Delta C = \epsilon A \cos\left(\angle Av\right) f \sin\theta_v\ \Delta\theta_v \Delta\phi_v \frac{\eta v^4}{2}. \tag{4.40}$$

By assuming that the angles in Figure 4.9 correspond to the angles in Equation 4.40 as $\theta_v = \left(\frac{\pi}{2} - \beta\right)$ and $\phi_v = \alpha$, the equation can be rewritten using the energy-geometrical factor:

$$\Delta C = \epsilon A \cos\left(\angle Av\right) f \sin\left(\frac{\pi}{2} - \beta\right) \Delta\beta\Delta\alpha \frac{\eta v^4}{2}$$

$$\Rightarrow \Delta C = \epsilon A \cos\left(\angle Av\right) f \cos\beta\Delta\beta\Delta\alpha \frac{v^4}{2} \frac{\Delta\left(\frac{E}{q}\right)}{\frac{E}{q}}$$

$$\Rightarrow \Delta C = \epsilon A \cos\left(\angle Av\right) \Delta\alpha \frac{\Delta\left(\frac{E}{q}\right)}{\frac{E}{q}} \cos\beta\Delta\beta \frac{v^4}{2} f$$

$$C = G_E^* \frac{v^4}{2} f\epsilon \tag{4.41}$$

$$G_E^* = A_e^* \left\langle \Delta\alpha \frac{\Delta E}{E} \right\rangle \int_{\Delta\beta} \cos\beta \mathrm{d}\beta \tag{4.42}$$

$$A_e^* = X_0^{'} \Delta R \cos\left(\angle Av\right). \tag{4.43}$$

The geometrical factor is a useful metric for comparing the collecting power of various types of instruments. It is a convenient way to summarize the gathering power of an instrument, but does not give the complete picture of what the instrument will measure in space. To determine the number of particles-per-second that a plasma instrument can be expected to measure for a given velocity distribution function, the geometric duty cycle must also be calculated.

4.4.3 Geometric Duty Cycle

The geometric duty cycle for a space plasma instrument characterizes the percentage of time that particles will be able to enter the instrument at a given voltage setting. There are several factors that are involved with the geometric duty cycle calculation, including the rotation of the spacecraft, the direction the instrument is facing with respect to the source of particles, the acceptance angle of the collimator, and the distribution of incoming particles. A simple illustration (Figure 4.10) is useful to explain the concept. With the direction of a beam of solar wind shown as a red arrow and the acceptance angle of the collimator as 6.17°, the spacecraft rotates on an axis indicated by the black dot. With each rotation, the collimator will sweep through the solar wind, temporarily bathing the detector in plasma. The geometric duty cycle can be calculated with a simple integral:

$$D = \frac{1}{360} \int_0^{6.17} d\Psi = 1.71\% \tag{4.44}$$

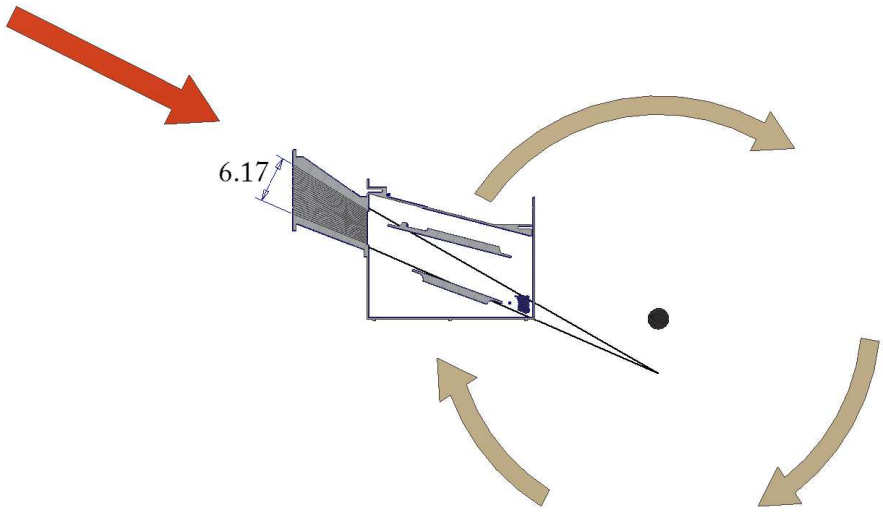

Figure 4.10: A simple illustration of spacecraft rotation for the calculation of a geometric duty cycle. The collimator has an entrance aperture of 6.17°. As the spacecraft rotates a full 2π radians, a beam of solar wind will penetrate the instrument for a fraction of the total time.

For a more pertinent illustration, consider the *Ulysses*–SWICS instrument, which has a collimator acceptance solid angle of roughly 4° x 69° and rotates about the Earth-pointing axis shown as a dashed blue line in Figure 4.6. If the aspect angle α, the angle between a pencil thin beam of incoming solar wind and the rotation axis of the spacecraft, is less than 2°, then as SWICS rotates it will see solar wind 50% of the time. If the aspect angle is larger, the geometric duty cycle can be found from spherical trigonometry to range between 0 and 1/2 (*von Steiger et al.*, 2000).

$$D_{(\alpha)} = \begin{cases} \frac{1}{2} & \text{for } \alpha \leq 2^\circ \\ \frac{1}{2\pi}\left(\cos^{-1}\left(\frac{\cos\alpha\cos\theta_m - \cos\theta_-}{\sin\alpha\sin\theta_m}\right) - \cos^{-1}\left(\frac{\cos\alpha\cos\theta_m - \cos\theta_+}{\sin\alpha\sin\theta_m}\right)\right) & \text{for } 2^\circ \leq \alpha < 56.04^\circ \\ 0 & \text{for } \alpha > 57.44^\circ \end{cases} \tag{4.45}$$

The collimator entrance of SWICS is characterized by the boundaries $\theta_- = 55°$, $\theta_+ = 59°$, $\phi_- = 0°$, and $\phi_+ = 69°$, and the axis of rotation is at $\theta_m = 57°$, $\phi_m = 0°$. An optimal arrangement would have SWICS aligned on the spacecraft in such a way that the incoming particles always passed through a part of the collimator, leading to a 100% geometric duty cycle. If the effects of thermal spreading are taken into account, the incoming particles are no longer a simple beam, but are best described as a Maxwellian distribution. A generalized formula for the geometric duty cycle must take this into account:

$$D_{(\alpha)} = \frac{1}{2\pi} \int_0^{2\pi} d\Psi \int_{\phi_-}^{\phi_+} d\phi \int_{\theta_-}^{\theta_+} \sin\theta \, d\theta \, f_{(\theta,\phi)}. \tag{4.46}$$

Here, Ψ is the spacecraft rotation angle, the θ and ϕ integrals describe the acceptance solid angle of the collimator, and $f_{(\theta,\phi)}$ is the velocity distribution function of the incoming particles, such as that shown in Equation 4.33.

4.5 Status of Current Technology

The instruments discussed here not only made groundbreaking measurements of the space environment, but also laid the foundation for the research carried out in this dissertation. Each successive mission brought with it lessons learned and improvements over those that came before. Some recent technological developments include SSDs with low-energy thresholds (*Funsten et al.*, 1997) and MCPs with improved efficiencies (*Siegmund et al.*, 2003; *Tremsin et al.*, 2007). The mass spectrometers used in space still have room in their design for optimization, and as improvements are made to increase the collecting power and detection efficiency, new instruments will be developed.

One limitation of the current design of ESAs is that particles with energies above a few MeV-per-nucleon require too high of voltages to adequately deflect and measure

them (*Klecker et al.*, 2006). This energy limit is near the lower threshold of ACRs in the suprathermal tail of the solar wind velocity spectrum. Another limitation is that the use of carbon foils in the TOF systems cause dispersion and energy loss, resulting in adverse affects to the instrument's resolution. A system that could eliminate the use of a foil, or perhaps move in the direction of extremely thin single-layer nanotube foils would help mitigate this restriction. The statistically low count rates of rare (i.e., low-density) particles also limits the resolution of data. New instrument designs need to allow for miniaturization without loss of resolution. This involves raising the collecting power per volume (or per mass) of the instrument, and can be achieved by innovative geometric designs such as those in the PEPE and FIPS instruments (*Young et al.*, 2007; *Koehn et al.*, 2002), or by optimizing and integrating the electronics and power supplies.

For the single-anode version of the cylindrically symmetric LEF TOF, it is extremely difficult to separate the high-resolution signals from the low-resolution ones when they are all convolved together on the straight-through detector (*Young*, 2007, private comm.). The high-resolution isochronous signal can be overshadowed by the broad peaks of the low-resolution measurement, an issue that is addressed with a new design for LEF TOF instruments, explained in Chapter VI.

Chapter V introduces a new design for an ESA, IonSpec, which achieves some of the improvements described above with a sensitivity and collecting time that substantially surpasses CHEM and SWICS. IonSpec enables new measurements due to its tremendous sensitivity, allowing for increased statistics of particle populations.

CHAPTER V

The Ion Composition Spectrometer (IonSpec)

5.1 Introduction

To enable new measurements that can explore the unstudied aspects of the space environment, new types of instruments must be developed — ones that overcome the inherent deficiencies of previous instruments. Pickup ions in particular require high-resolution measurements carried out by instruments specifically designed for particles in the pickup ion energy range. In addition, the collecting power of instruments must be increased to measure greater amounts of these particle populations, some of which are found in such low densities that only a few atoms are detected each year (*Gloeckler and Geiss*, 1996). The goal of high-resolution measurements is addressed in Chapter VI, where an improved design for time-of-flight analyzers is discussed. The need for greater collecting power is addressed here in a new instrument design — the Ion Composition Spectrometer (IonSpec). The collecting power and sensitivity of an ion mass spectrometer can be improved by increasing its geometrical factor and geometric duty cycle, as well as the integration time that it spends at a given voltage setting. A straight-forward way to increase the geometrical factor is to enlarge the effective entrance aperture of the instrument, thus increasing its total size. To keep the size and mass of such instruments low, the geometrical factor could alternatively be increased by improving the energy resolution η or the solid angle field of view

$\Delta\Omega = \sin\theta\Delta\theta\Delta\Phi$.

IonSpec is the next step in the evolution of electrostatic analyzers like CHEM and SWICS, but substantially modified to provide new and improved measurements. This is done by increasing its geometrical factor and the time it spends analyzing a given particle species before stepping to a new voltage, i.e., the integration time. The concept for IonSpec, originally called the Pickup Ion Composition Spectrometer (PICSPEC), can be found in proposals for the Interstellar Pathfinder mission (*Gloeckler et al.*, 1998b, 2001; *McComas et al.*, 2003) and the Particle Acceleration in the Turbulent Heliosphere (PATH) mission (*Zurbuchen et al.*, 2003). The research in this dissertation covers the entire design cycle of the instrument, taking the concept through simulation (§ 5.2–5.4), fabrication and testing (§ 5.5–5.6), and analysis of future innovations and adjustments to the design (§ 5.7).

5.2 Conceptual Description

Position-sensitive particle detectors can measure not only the E/q, but also the incident angle of incoming ions. The FIPS instrument on *MESSENGER* is one such instrument (*Koehn et al.*, 2002). The innovation for IonSpec was to use position-sensitive detectors similar to FIPS to identify the incoming angle, and also to implement a completely new ESA design to fundamentally increase the energy range. This is achieved through enlarging the exit aperture of a correctly shaped ESA modified from the original SWICS design, which had only a small slit for an exit aperture. This modification allows ions with a broad range of E/q to pass into the TOF analyzer simultaneously. Detectors with position sensitivity are used to distinguish between the different E/q species in a similar fashion to what is used on the *ACE*–Solar Energetic Particle Ionic Charge Analyzer (SEPICA) instrument (*Möbius et al.*, 1998). Figure 5.1 shows an initial conceptual drawing of IonSpec, with the ESA on the left and the TOF system on the right.

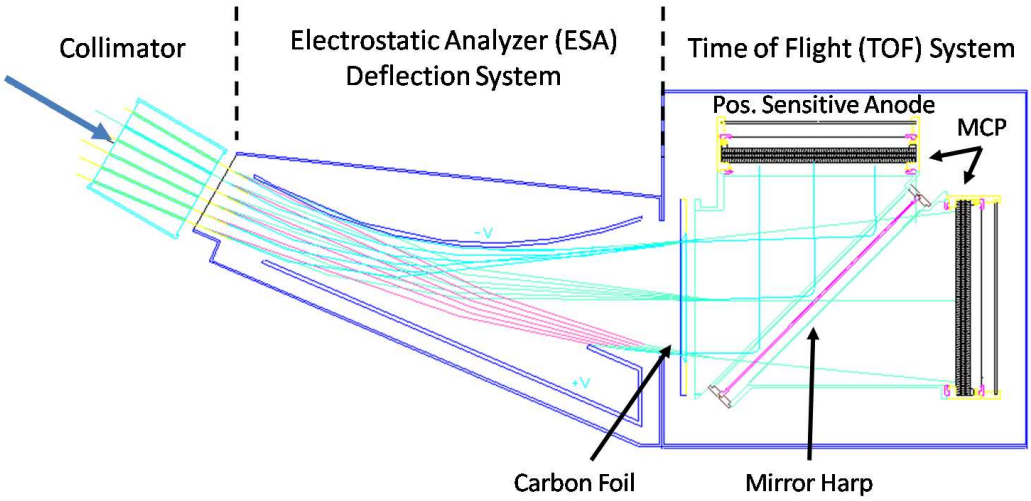

Figure 5.1: A conceptual drawing of the IonSpec instrument. The trajectories of particles entering at the left are deflected by charged plates in the ESA, with their radius of deflection inversely proportional to their E/q. A position-sensitive anode is used in the TOF analyzer to identify the species. Figure adapted from R. Lundgren (private communication).

As in the SWICS instrument, ions are deflected as they pass through the ESA. The radius of refraction, introduced in § 4.2.1, is inversely proportional to the E/q, so higher-energy ions enter the TOF telescope near the lower region of the ESA's exit aperture. Once ions enter the TOF region they penetrate a carbon foil, causing electrons to be ejected. These electrons are accelerated toward a charged wire "mirror harp", which deflects them toward an MCP and its accompanying position-sensitive anode while maintaining position information. The voltages on the charged electrostatic deflection plates can be adjusted to allow a specific energy passband to enter the TOF region, but these voltage steps would not need to occur as often as those in SWICS to achieve the same E/q range of acceptance. By using a "sit and stare" approach to minimize the voltage stepping, the IonSpec concept greatly increases the ability to accumulate counts for the different ion species.

The voltages on the deflection plates of the SWICS instruments step to a different value every 12 seconds. For the SWICS instrument on *Ulysses*, the main channel covers an E/q range of 0.65–60 keV/e in each 12.8-minute, 64-step cycle (*Gloeckler*

et al., 1992). For *ACE*–SWICS, a 0.49–100 keV/e range is covered in a 12-minute, 60-step cycle (*Gloeckler et al.*, 1998a). The goal for IonSpec is to design an instrument that can measure a broad instantaneous energy passband of $(E/q)_{\max} = 3(E/q)_{\min}$ without stepping the voltage (*Gloeckler et al.*, 1998b, 2001; *Möbius et al.*, 1998). By having a factor of 3 in E/q passing through the ESA at once and using a position-sensitive anode to tell the species apart, IonSpec would be able to cover in only 5 steps the same E/q range as the SWICS instruments. For comparison, if it were to operate on a 12-minute cycle, the deflection voltages on IonSpec would step every 144 seconds, giving it an integration time 12 times longer than SWICS for each E/q. For purposes of illustration in this dissertation, the $(E/q)_{\min}$ and $(E/q)_{\max}$ are given values of 30 keV/e and 90 keV/e, respectively. This preserves the factor of 3 in range and allows for a more quantitative discussion. All voltages and energies can be adjusted to a required energy range if needed.

5.3 Analytical Model

There are many factors that affect the trajectories of ions as they pass through the ESA. These include the size and shape of the grounded housing, the length, angle, and voltages of the electrostatic deflection plates, the angle of incoming ions through the collimator, and the size and position of the entrance and exit apertures. Small changes in any of these parameters could have substantial effects on the ion's trajectory through the ESA. To gain a general understanding for these effects, and to possibly identify some general ranges of optimization, it is useful to study a simplified analytical model that calculates trajectories based on changes in energy.

Figure 5.2 shows a schematic of ion deflection between parallel, charged plates of length λ that are separated by a distance d. The upper and lower deflection plates have voltages V_U and V_L, respectively. In this schematic, regions I and V are free of electrostatic fields and represent areas outside of the ESA. Regions II and IV are

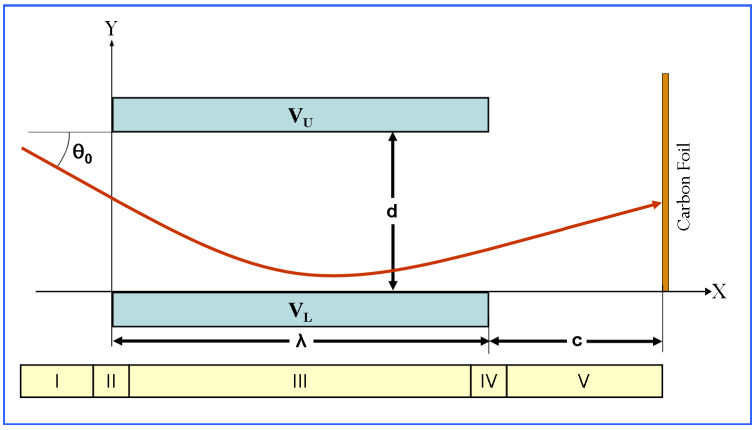

Figure 5.2: An analytical model of the IonSpec ESA. Ions enter at angle θ_0 and are deflected by electrostatic deflection plates of length λ, voltage V, and separation d. Ions then travel through a field-free region of distance c before reaching the carbon foil.

transition regions that represent the ESA's entrance and exit apertures, respectively, and region III is the deflection region between the charged plates, which is filled by a constant electric field directed from the lower plate straight toward the upper plate. The effects of fringe fields are not taken into account in this simplified model. In the following equations, parameters that pertain to any given region are marked with the region number as a subscript.

The voltage potential between the charged plates varies in only the y direction and the electrostatic fields do not extend beyond the sides of the plates. By integrating Equation 2.9 over y, expressions for the potential $\Phi_{(y)}$ and the magnitude of the electric field $|\mathbf{E}|$ between the charged plates can be derived (5.1)–(5.2).

$$\mathbf{E} = -\nabla\Phi$$
$$\Rightarrow -\int |\mathbf{E}|\, \mathrm{d}y\hat{\mathbf{y}} = \Phi\hat{\mathbf{y}}$$
$$\Rightarrow -|\mathbf{E}|\, y + C_1 = \Phi$$

Boundary condition: at $y = 0$, $\Phi_{(y)} = V_L$.

$$C_1 = V_L$$
$$\Phi_{(y)} = V_L - |\mathbf{E}|\, y \tag{5.1}$$

Boundary condition: at $y = d$, $\Phi_{(y)} = V_U$.

$$V_U = -|\mathbf{E}|\, d + V_L$$
$$\Rightarrow |\mathbf{E}| = \frac{(V_L - V_U)}{d} \tag{5.2}$$

The effect of stepping into or out of the field is akin to a change in the particle's energy. Since fringe fields are ignored and the constant electric field between the charged plates is vertical, the abrupt change in energy in regions II and IV is only experienced by the particle in the horizontal (x) direction. This implies that only the x components of the velocity are affected at this transition (5.3).

$$v_x = v\cos\theta \tag{5.3}$$
$$v_y = v\sin\theta \tag{5.4}$$

An ion approaches the ESA in a straight line at an angle θ_0 with an initial speed v_I. The energy-per-charge it has when it is between the plates E_{III}/q must equal the initial energy-per-charge of the particle E_I/q less the work-per-charge required to bring it into the field $q\Phi_{yII}/q$:.

$$\frac{E_{xIII}}{q} = \frac{E_{xI}}{q} - \frac{q\Phi_{yII}}{q} \tag{5.5}$$
$$\Rightarrow \frac{1}{2}mv_{xIII}^2 = \frac{1}{2}mv_{xI}^2 - q\Phi_{yII} \tag{5.6}$$
$$\Rightarrow v_{xIII} = \sqrt{v_{xI}^2 - \frac{2q\Phi_{yII}}{m}}. \tag{5.7}$$

In region III the particle travels with a constant horizontal velocity v_{xIII}, but ex-

periences a Lorentz force (2.3) that affects its position and velocity in the y direction. By equating the Lorentz force to the force the particle has due to Newton's second law (2.4) and integrating over time $t_{III} = x_{III}/v_{xIII}$, the parameters y_{III} and v_{yIII} can be found throughout region III.

$$\mathbf{F} = m\mathbf{a} = q\mathbf{E} \tag{5.8}$$

$$\Rightarrow v_{yIII} = \frac{q\,|\mathbf{E}|\,t_{III}}{m} + v_{yI} \tag{5.9}$$

$$\Rightarrow y_{III} = \frac{q\,|\mathbf{E}|\,t_{III}^2}{2m} + v_{yI}t_{III} + y_{II} \tag{5.10}$$

Region IV is similar to region II in that the particle's behavior can be modeled by a change in the horizontal component of the energy. The kinetic energy-per-charge of the particle after exiting the plates E_{xV}/q must equal the energy-per-charge between the plates E_{xIII}/q plus the work-per-charge required to send the particle out of the field $q\Phi_{yIV}/q$:

$$\frac{E_{xV}}{q} = \frac{E_{xIII}}{q} + \frac{q\Phi_{yIV}}{q} \tag{5.11}$$

$$\Rightarrow \frac{1}{2}mv_{xV}^2 = \frac{1}{2}mv_{xIII}^2 + q\Phi_{yIV} \tag{5.12}$$

$$\Rightarrow v_{xV} = \sqrt{v_{xIII}^2 + \frac{2q\Phi_{yIV}}{m}}. \tag{5.13}$$

The ion then travels in a straight line in the field-free region V, impacting the carbon foil after traveling a distance c. The equations can be combined in such as way as to solve for the value of y at the carbon foil in terms of the other parameters, thus allowing a description of the particle's trajectory through the entire area. One useful application of this analytical model is the analysis of perturbations in the initial parameters. By varying the initial parameters and monitoring the position of ion impact at the carbon foil, the most sensitive parameters and their boundaries can be identified.

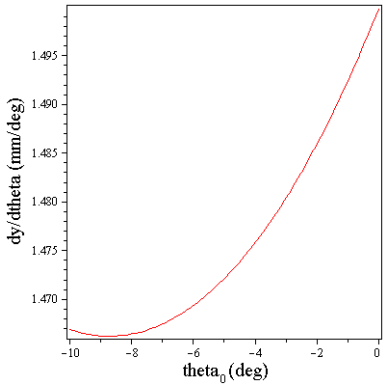

Figure 5.3: Effects of initial angular perturbations $d\theta$ on the dispersion of final impact positions dy. When the ions' initial entrance angle θ_0 is perturbed, it will cause a dispersion in their impact locations on the carbon foil. This perturbation affects the trajectories differently depending on the value of θ_0. The value of θ_0 that results in the minimal amount of dispersion at the foil can be found from the minimum of $dy/d\theta$.

There is a spread in position dy at the carbon foil that occurs when the entrance angle θ_0 is slightly perturbed by an amount $d\theta$. For a position-sensitive measurement, a spread in position relates to a decrease in E/q resolution. High-resolution measurements will require this dispersion at the foil to be minimized as much as possible. The amount of dispersion is dependent on the value of the entrance angle, with the optimum value of θ_0 being the one for which $dy/d\theta$ is at a minimum (Figure 5.3). The optimum angle increases in magnitude as the initial E/q decreases (Figure 5.4). For purposes of illustration, the parameters in the model were set to $E/q = 50$ keV/e, $V_U = -4$ kV, $V_L = +4$ kV, $d = 30$ mm, $c = 20$ mm, $\lambda = 65$ mm, $\theta_0 = -5°$, and $y_{II} = 15$ mm. The change in position with angular perturbations is on the order of 1.4 mm/deg in this simulation.

The vertical impact position y at the carbon foil as a function of initial E/q, shown in Figure 5.5(a), indicates that ions with E/q near the maximum of the energy passband will not have a large vertical separation from neighboring E/q particles. This is in agreement with the radius of refraction of charged particles (4.3) that share a common tangent, as illustrated in Figure 4.1. Unlike the angular perturbations,

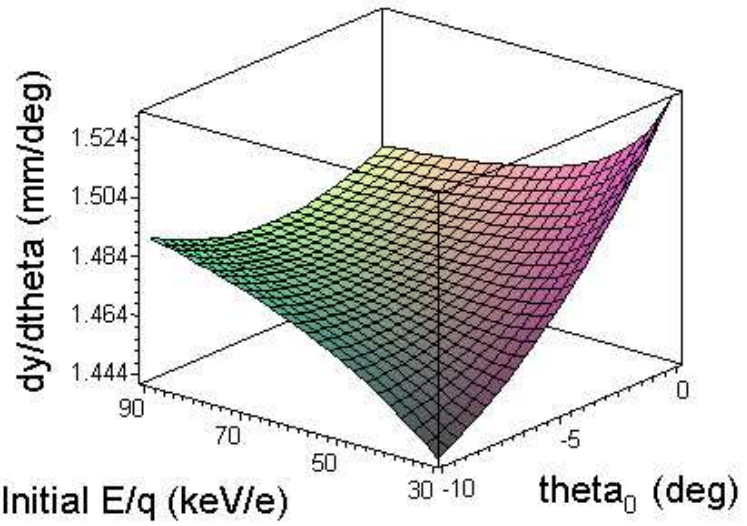

Figure 5.4: The energy dependence of optimum ion entrance angles. The optimum values of θ_0 at each E/q are given by the minima of the curve. As the initial E/q of the ion is decreased, the optimum entrance angle must become steeper to keep dispersion at a minimum.

there is no optimal E/q for which perturbations are minimized. It can, however, be noted that ions with higher initial E/q will not be affected as much by perturbations as ions with lower E/q, as shown in Figure 5.5(b). The behavior is consistent across all entrance angles. The change in final impact position with perturbations in the initial E/q is of the order 10^{-1} mm/keV/e in this simulation, an order of magnitude smaller than the effects due to angular perturbations.

Ions on the lower-energy end of the energy passband will be more affected by perturbations than ions with a higher initial E/q. However, this does not necessarily imply that their energy resolution at the carbon foil will be worse. There are many factors that cannot be accounted for with this simplified model. The effects of such things as non-parallel plates, plates that are not necessarily the same length, and fringe fields that will affect particle trajectories must be included. To fully investigate the IonSpec concept, a more detailed analysis using ion optics simulations is required.

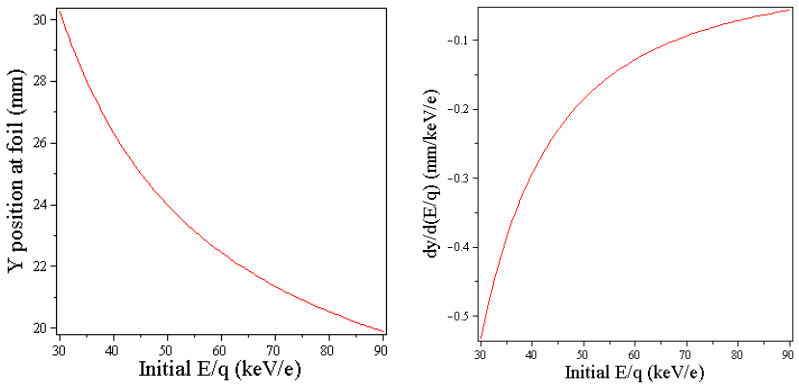

(a) (b)

Figure 5.5: Effects of initial E/q values and perturbations on final position. (a) The impact position at the carbon foil as a function of initial E/q shows that higher-E/q ions will impact close to each other vertically, while lower-E/q ions will be more spread apart. (b) Perturbations of the initial E/q will not affect the final impact positions of ions with an initial E/q near the maximum of the E/q passband as much as the lower E/q ions.

5.4 Simulations

Ion optics simulations are useful for determining the behavior of ions in the IonSpec ESA. As ions pass between the electrostatic deflection plates, they are sorted according to their E/q and exit the ESA at different locations, with their radius of deflection inversely proportional to their E/q (Figure 5.6). One key challenge is to simultaneously focus ions with different E/q values on a given foil plane. The focal points of the deflected ions can be moved by adjusting various parameters in the simulation, but the sensitive interdependencies among the parameters require care to be taken or the ions will go out of focus entirely.

Many different versions of IonSpec were explored before the design in Figure 5.6 was attained. With each iteration, modifications were made to the ion's incoming angle θ_0, the size and shape of the ESA, as well as the ratios of the voltages V on the electrostatic deflection plates. One goal during optimization was to cause the focal points of the different ion species to all line up vertically at the carbon foil. Figure 5.6 examines a configuration in which no post-acceleration voltage was used

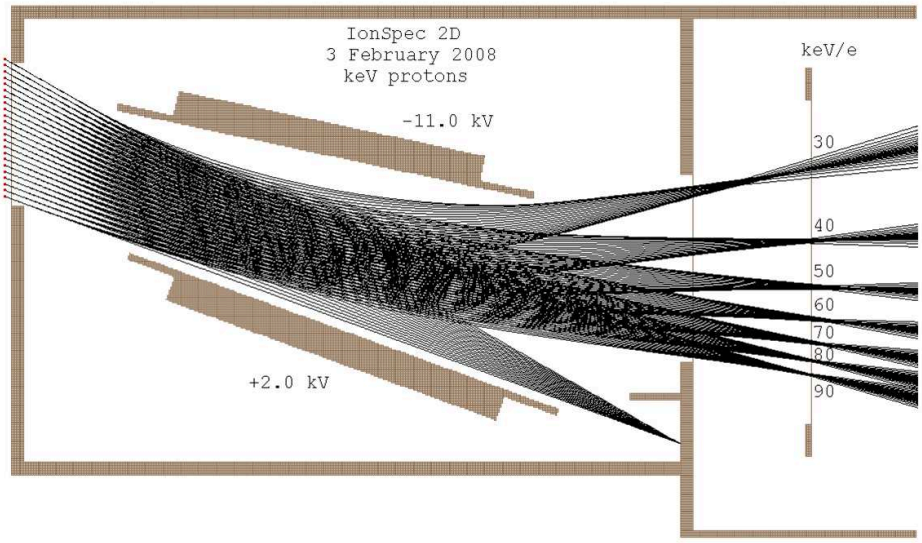

Figure 5.6: A 2D view of the IonSpec electrostatic analyzer. Simulated ion trajectories for several different E/q species are shown, as well as the straight trajectories of UV light to illustrate the collimator's focus. The focal points do not line up vertically at the carbon foil.

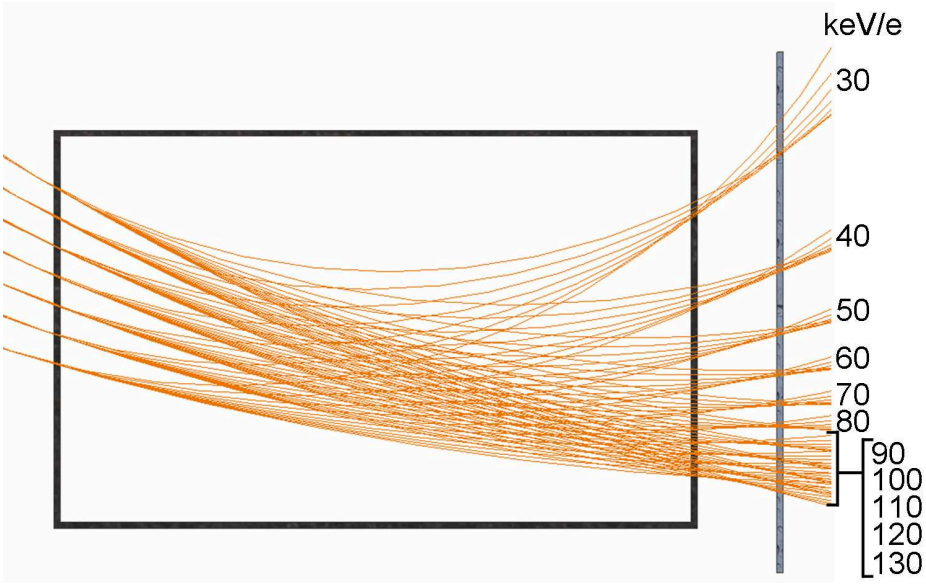

Figure 5.7: An illustration of the radius of refraction from several initial positions and angles. The IonSpec collimator will allow particles in from different positions, all aimed at the same focal point. This idealized trace of circles shows the same behavior as the ion simulations, namely that the focal points of each E/q species do not align vertically with each other.

to accelerate the ions before they impact the carbon foil. A -20 kV post-acceleration voltage was also simulated at the carbon foil, but it did not lead to any improvement. It was finally determined that this idealized goal is physically unattainable, with the explanation related to the radius of refraction. The illustration in Figure 4.1 traced the circular trajectories of particles with a common entry point and entrance angle. If other entry points are included with entrance angles all aimed toward the same collimator focal point, then a series of overlapping trajectories will be mapped out. The circles overlap near the 'detector' creating points of focus that are interesting in that they do not line up vertically among the different E/q species (Figure 5.7). This calculation is similar to what was observed in the ion optics simulations. The trait of a non-vertical alignment of focal points is due to a geometrical shaping caused by the Lorentz force. During simulations, the shape and positioning of this arc of focal points was manipulated, but vertical alignment was never fully achieved. This characteristic could be accommodated by using a curved carbon foil whose shape follows the locations of the focal points, resulting in an improved position resolution measurement.

A close examination of the focal points of the overlapping circles also shows that they do not come into a sharp focus. Painstaking attention was paid to deflection plate angles, plate lengths, voltage ratios, and entrance aperture size and positioning in the IonSpec simulations to overcome this characteristic. A sharp, symmetric focus for each E/q at all entrance positions can be seen in the final IonSpec version in Figure 5.6.

One of the performance metrics for this instrument is the ability to separate and identify ions by their E/q, measured by the E/q resolution $\eta = \frac{\Delta E/q}{E/q}$. To examine this resolution, it is necessary to carry out Monte Carlo simulations in which the initial position, angle of incidence, and E/q of the ions are varied within certain limits. For these specific simulations, the entrance angle was allowed to vary by $\pm\, 0.35°$ and

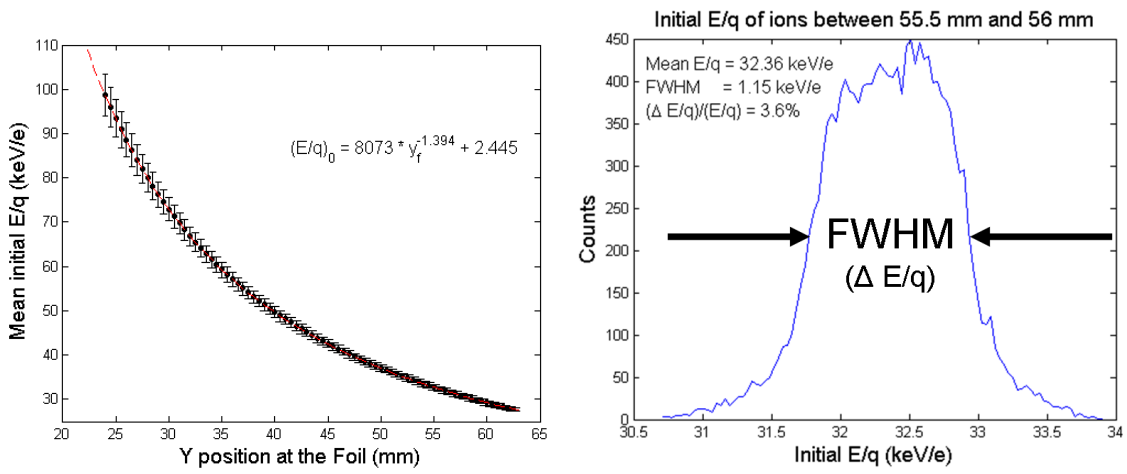

(a) (b)

Figure 5.8: The relation between mean E/q and impact position at the carbon foil for IonSpec Monte Carlo simulations. (a) The mean E/q is plotted for each 0.5 mm bin, along with the FWHM of the E/q distribution. The data closely fits a power law, with an index of -1.4. (b) The FWHM, written as $\Delta(E/q)$ is found from a histogram of E/q plotted across the impact position on the carbon foil.

the initial vertical position and E/q were randomized. As the ions reach the carbon foil, they are collected in bins of size $y = 0.5$ mm each, in agreement with the sub millimeter resolution of a position-sensitive anode. For each of these bins, histograms of initial E/q were created using the collected Monte Carlo data. Figure 5.8 shows simulation data for the ESA geometry of Figure 5.6. The average initial E/q of ions is plotted against their vertical impact positions in Figure 5.8(a). As expected, ions with low E/q impact the foil at higher vertical positions, indicating a smaller radius of refraction as they travel through the ESA. The E/q is plotted for each bin, along with error bars that indicate the FWHM of the E/q distribution. The FWHM of the E/q, shown in Figure 5.8(b), becomes larger as the mean E/q increases. Ions with E/q values near the maximum limit of the energy passband tend to have their focal points close to each other, as seen in Figures 5.6 and 5.7, so a bin in this area of the carbon foil will collect ions with several different E/q values and a large FWHM in their E/q distribution. A bin near the minimum limit of the energy passband (i.e.,

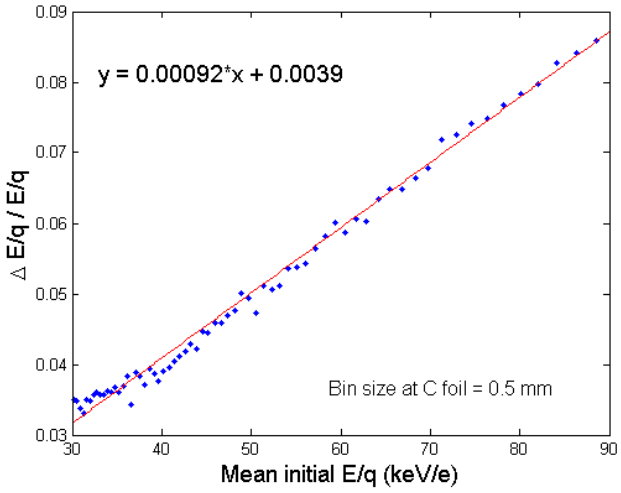

Figure 5.9: The relation between E/q resolution and mean E/q at the carbon foil for 2D IonSpec Monte Carlo simulations. The energy resolution follows a clear linear relationship, with the best values found at the low-E/q range of the energy passband. The resolution ranges from 3.4–9.0 %.

vertically high on the foil) will predominantly measure ions with E/q similar to each other, leading to a small spread in the E/q distribution. A fit to the mean E/q values in the Monte Carlo data follows a power law (5.14).

$$(E/q)_0 = 8073 y_f^{-1.394} + 2.445 \tag{5.14}$$

When the values for η in each bin are plotted together for a given deflection voltage, a clear linear relation is revealed in which the ions with a lower E/q have better resolution than ions with a higher E/q (Figure 5.9). The resolution for the 2D simulations of IonSpec ranges from 3.4–9.0 % and has a slope of 9.3×10^{-4} $(\mathrm{keV/e})^{-1}$.

$$\eta = 0.00093\,(E/q) + 0.0037 \tag{5.15}$$

Once the 2D simulations were complete, they were expanded into 3D by rotating the geometry into a cylindrical wedge shape similar to SWICS. Minor modifications needed to be made to the geometry, collimator focus, and voltage ratios after exam-

ining the 3D simulations, since SIMION treats a 2D simulation as though the fields extended to infinity in the 3rd dimension. In 3D, the effects of fringe fields coming around the edges of the charged deflection plates will skew the ion trajectories. As a 3D geometry took shape, the ESA was modeled using the 3D computer-aided design (CAD) software Autodesk Inventor Professional so that it could be constructed.

5.5 Structural Design and 3D Models

Proper voltage ratios, entrance angles, and general instrument geometry, must all be considered during the design process to create parts that can physically be built and assembled. Each component of IonSpec was created using CAD software, then the size and shape were modified until they fit soundly together. Once a complete ESA was drawn in 3D, the model was imported into SIMION to run additional ion simulations. The design of the ESA went through several iterations as various parts were changed to make them lighter, easier to fabricate, or more structurally sound. With each change in a part's design, ion simulations needed to be repeated to ensure that the energy resolution did not suffer. The final design of the IonSpec ESA consisted of a 60° x 6° field of view, a collimator, and a light trap, as shown in Figure 5.10. The total weight of the aluminum parts was calculated to be just over 2 kg, not including the fasteners, but since this was only a test prototype no attempt was made to minimize the weight of the sensor beyond the weight limits of the motion control stages that were used during testing.

Uniform movement of the instrument during testing was attained by use of three motion control stages for rotational (elevation angle), horizontal, and vertical directions. A Burle Channeltron® single channel electron multiplier (CEM) was used for monitoring the ion beam before it reached the ESA, and a position-sensitive Quantar Technology Inc. MCP Imaging Detector System was used in place of the carbon foil and TOF analyzer. During the planning of the test setup, a problem was discovered

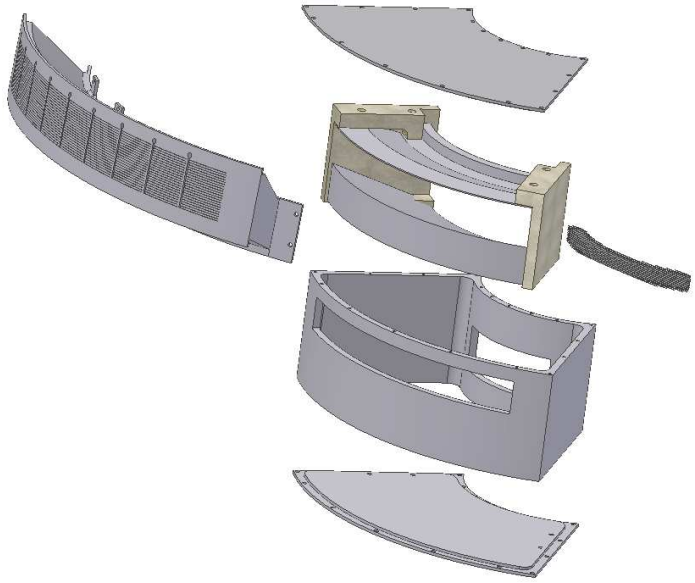

Figure 5.10: A 3D model of the IonSpec ESA, exploded view. Shown are the collimator, deflection plate assembly, outer case, and light trap plates. The ESA was calculated to weigh just over 2 kg, not including the weight of fasteners.

in the ESA design. The available Quantar detector was too large to fit behind the instrument where its MCP would line up with the plane of the simulated carbon foil (Figure 5.11). To avoid this problem, the prototype test of the ESA was changed to a version with a rectangular shape rather than one with cylindrical symmetry. The azimuthal symmetry of the ESA was attained by revolving the 2D design about an axis. Ion simulations show that the ions traveling through the ESA retain the same behavior at different incident azimuthal angles until the edges of the plates are approached, where fringe fields cause azimuthal dispersion (Figure 5.12). Similarly, a rectangular-shaped instrument will behave as the 2D simulations, retaining the same E/q focusing properties and suffering from fringe field dispersion effects near the plate edges. The innovation in the IonSpec design is found in the plane of the 2D illustration, which contains the spatial separation and simultaneous measurement of an entire range of E/q species. This novel technology can be demonstrated with either a rectangular or azimuthal instrument since the plane of interest has the same

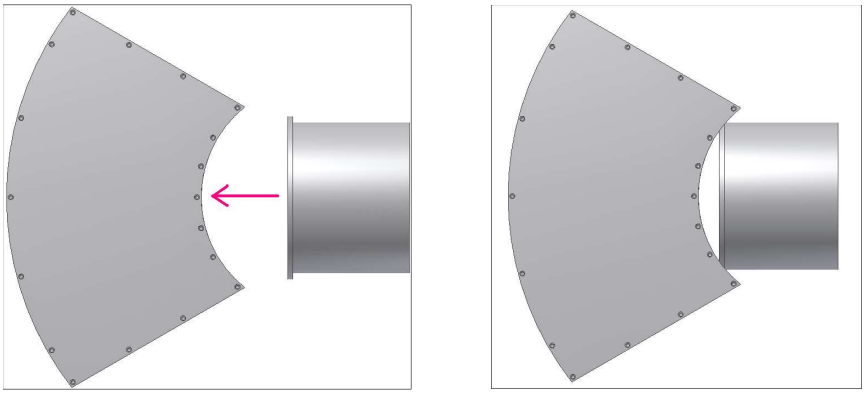

Figure 5.11: The imprecise fit of the Quantar detector behind the original IonSpec ESA. The position-sensitive detector available for testing of the IonSpec ESA was too large to fit within the inner radius of the housing. This led to a modification of the design from an ESA with cylindrical symmetry to one with rectangular geometry.

geometry in both cases.

To change the geometry to a rectangular shape, a new series of simulations and structural models needed to be studied. Instead of a $\pm 30°$ revolution, the electrostatic deflection plates were extended in the z direction by ± 50 mm, shown in Figure 5.13. To test the resolution and mitigate the effects of fringe fields, the simulation results shown in Figure 5.14 consisted of a Monte Carlo run with ions kept within the boundaries $z = \pm 10$ mm. The initial elevation angle was varied by $\pm 0.35°$, the initial azimuthal angle was varied by $\pm 1°$, and the initial E/q and vertical position were randomized. The E/q resolution of this version of the ESA ranged from 3.2–8.6 %, and followed a linear trend as before, with a slope of 9.0×10^{-4} $(\mathrm{keV/e})^{-1}$, only 2% different than the slope from the 2D simulations.

Once the geometry was set, the entire test setup was modeled with CAD software to ensure that all of the mounting plates and instrument components would fit together properly, and that they would be able to fit in the vacuum chamber in the necessary configuration (see Figures 5.15 and 5.16). Rather than constructing a full collimator for the rectangular IonSpec, a single 0.75 mm collimator slit was used, with the ESA itself rotated through each of the collimator angles on an axis through

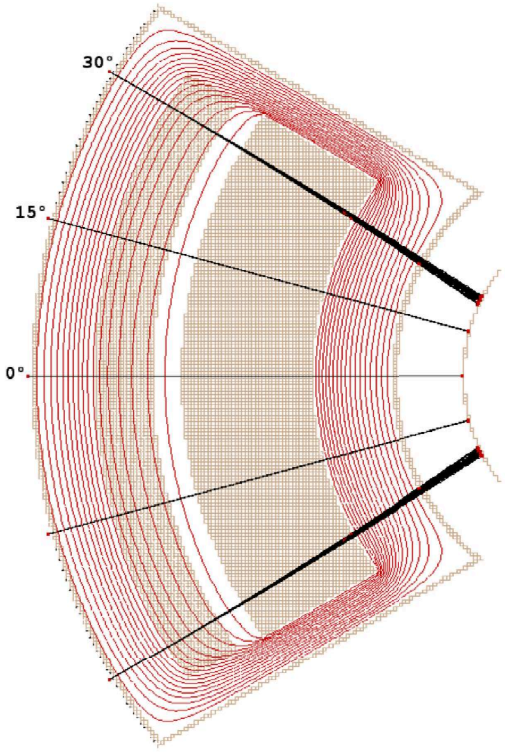

Figure 5.12: The effects of fringe fields on ion trajectories. In this top view slice of the IonSpec ESA, ions enter from the left and are refracted inward if they travel near the edges of the electrostatic deflection plates. Electrostatic field contours are shown in red.

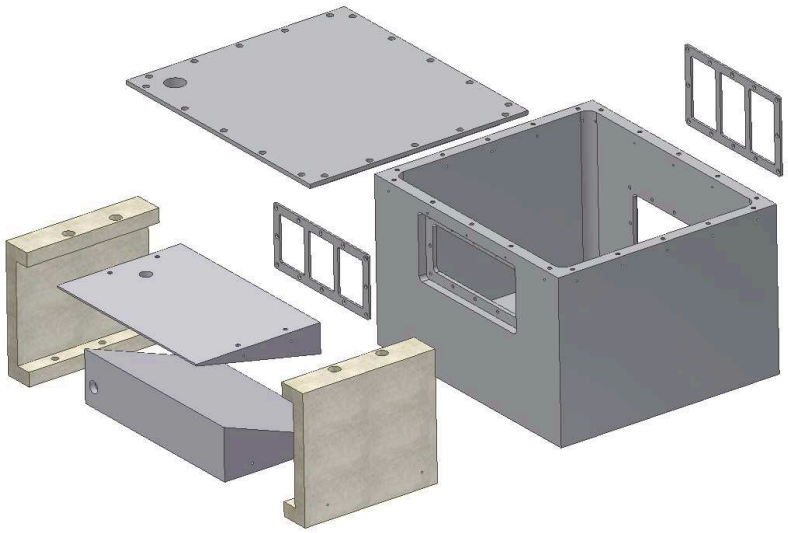

Figure 5.13: A 3D model of the rectangular IonSpec ESA, exploded view. The geometry is the same in the xy plane as it was for the azimuthally symmetric ESA.

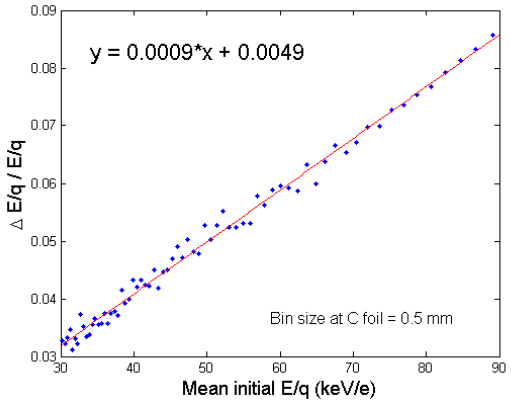

Figure 5.14: E/q resolution over the entire energy passband for the rectangular IonSpec geometry. The rectangular CAD model was imported into SIMION for Monte Carlo simulations of ion trajectories. The relation of E/q resolution to mean initial E/q is linear, similar to the 2D simulations, and ranges from 3.2–8.6%.

the modeled collimator focal point (Figure 5.17). To keep the interior electrostatic fields from affecting ions or equipment outside of the ESA, field containment grids were designed to cover the entrance and exit apertures.

Unique drawings were created for each mechanical part to be fabricated (see Appendix B), but even at this stage, minor modifications were made to some parts in order to accelerate fabrication and keep within the allotted budget. Upon completion, each metallic part was triple-cleaned in a process that included washing with detergent and then submersing in an ultrasonic bath with solutions of Trichloroethylene, Acetone, and finally Ethyl Alcohol. The non-metallic parts such as the two insulating brackets used to hold the electrostatic deflection plates followed the same cleaning process, but without the Trichloroethylene or Acetone chemical baths. The final parts and complete ESA are shown in Figure 5.18.

5.6 Measurements and Discussion

The measurements for the IonSpec ESA were performed in a vacuum chamber at the University of Michigan with pressures below 3×10^{-7} Torr. Such pressures

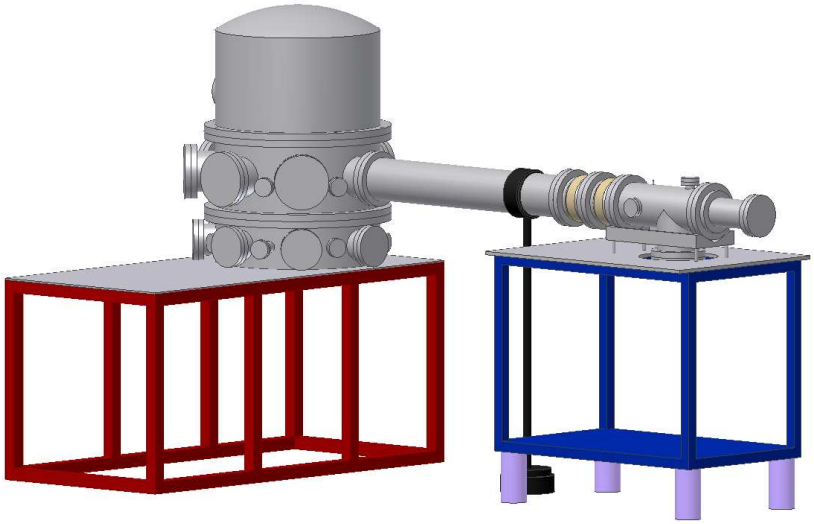

Figure 5.15: A model of the vacuum system used in testing of the IonSpec ESA. An ion source accelerates particles through a focusing lens and Wien filter, which sorts them by m/q, before they pass through the drift tube into the main chamber. A grounded cage (not shown) surrounds the particle acceleration system so it can safely be floated to high voltage.

are necessary to keep the humidity-sensitive MCPs clean and dry during the testing, as well as avoid possible voltage arcing and reduce the amount of background noise in the measurement. The particle acceleration system (Figure 5.19) consists of an ion source that uses electron impact ionization to create electrically charged plasma from an input gas. The source is floated at an input voltage that causes particles to accelerate down the tube once they become ionized. The ion beam passes through an Einzel lens that brings it into focus, then enters a Wien filter where the ions are sorted by their velocity. Since the ion source sends out particles with a known energy, the velocity can be shown to relate inversely to the m/q. By adjusting the electric and magnetic fields in the Wien filter, specific values of m/q can be tuned to pass straight through the filter, past the insulating ceramic collars, and down the drift tube into the main vacuum chamber where the detectors are located (Figure 5.20). A detailed schematic of the acceleration system used for these measurements can be found in Appendix B.

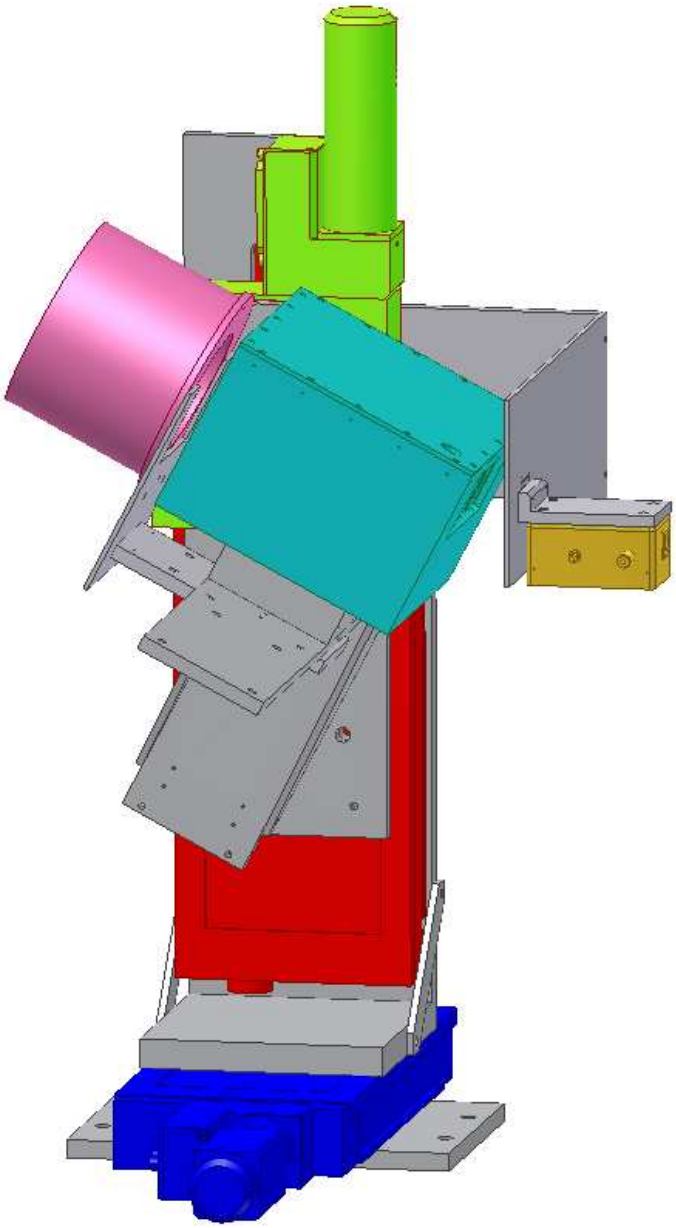

Figure 5.16: The test setup for IonSpec ESA measurements. The horizontal (*blue*), vertical (*red*), and rotational (*green*) motion control stages provide the necessary degrees of movement. A CEM (*gold*) is mounted below the collimator slit to detect the incoming ion beam, and the Quantar detector (*pink*) is mounted behind the exit aperture to detect the deflected ions. The IonSpec ESA (*turquoise*) is mounted so that the rotational stage pivot is on the axis of the collimator focal point.

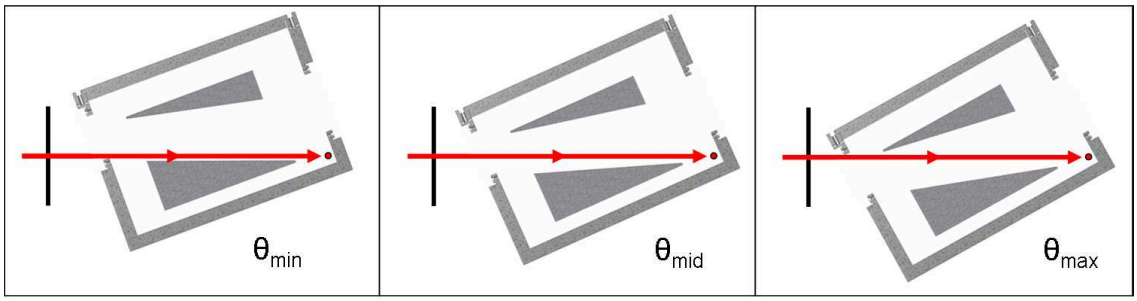

Figure 5.17: The single-slit method of measuring the full collimator range. The collimator focal point used in simulations (*red dot*) is the pivot point for the ESA rotation. Ions passing through a single collimator slit will enter the ESA at different angles and initial positions as the ESA is rotated, covering the full collimator range from $\theta_{\min}$ to $\theta_{\max}$.

Tests were conducted to verify that the collimator slit was indeed lined up with the pivot of the rotational motion stage so the effects of a full collimator could be reproduced. The Quantar detector was installed such that the surface of the MCP was colinear with the pivot axis, then measurements were taken at several angles. The results show that the position of the ion beam moved slightly in the vertical direction as the angles were adjusted (Figure 5.21). In the 20°–30° range of the IonSpec tests, the vertical movement of the beam was less than 1.5 mm. A slight spread in the distributions of detected ions can be expected due to the effects of rotation.

Hydrogen gas was used as an input for the main test of the ESA's deflection system, along with the equipment settings listed in Table 5.1. Rather than change the E/q of the ion beam to sweep through the factor of 3 in the energy passband, the voltage settings on the electrostatic deflection plates were adjusted. To ensure that the full range of the entrance aperture was being utilized at each voltage step, and to provide the effect of ions coming through the full collimator, a range of entrance angles covering 19°–30° was scanned in steps of 1°. The first and last of these angles did not yield any ions passing through the ESA since the aperture was rotated out of the beam line. The voltages for the ESA's electrostatic deflection plates were set to the ratio of -12:+1, with the negative plate on the top. For a 1 keV ion beam, voltages

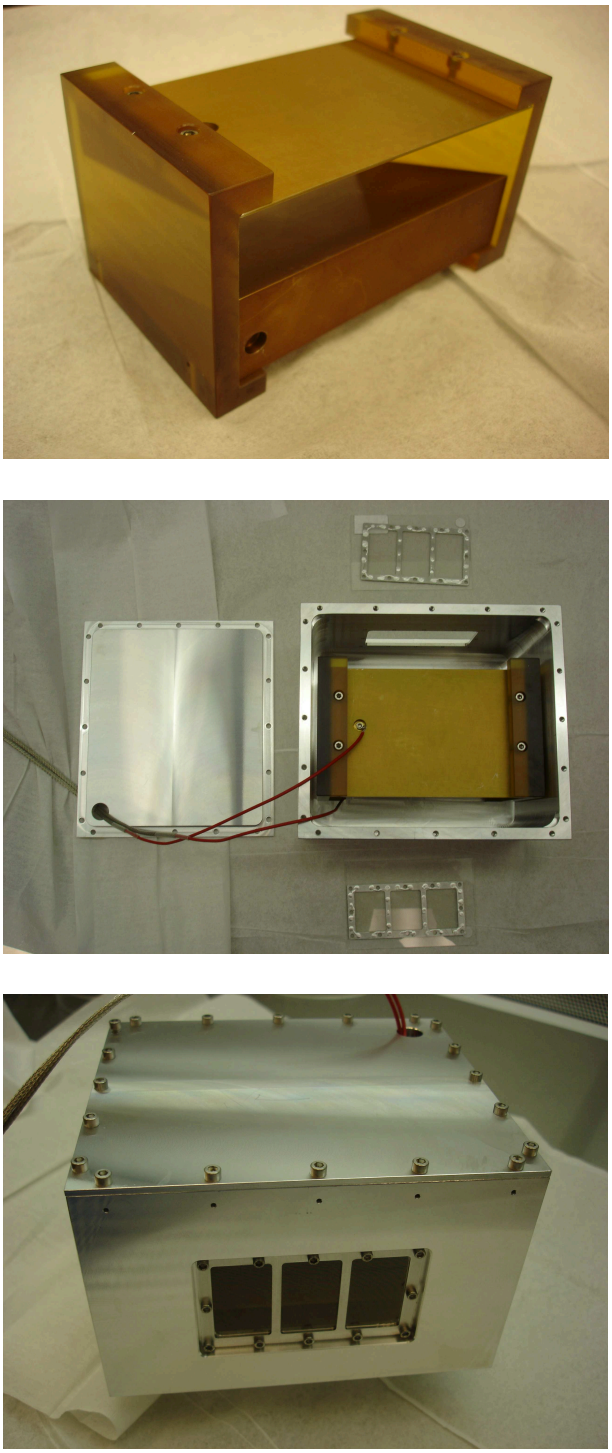

Figure 5.18: The IonSpec Electrostatic Analyzer. All parts were triple-cleaned and assembled in a clean environment to avoid the risk of contaminants entering the vacuum system during testing.

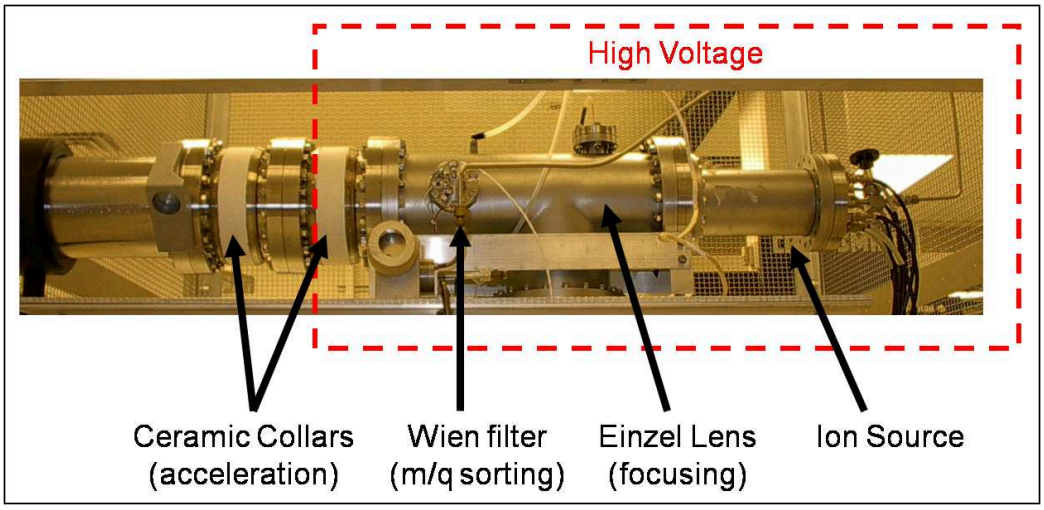

Figure 5.19: The ion acceleration system used in laboratory tests of plasma instrumentation. Ions are generated in the ion source and accelerated toward a focusing Einzel lens. They next pass into a Wien filter, where they are sorted by their m/q. Ions of the selected m/q continue past the insulating ceramic collars where they are accelerated before continuing down the drift tube. The drift tube leads to the main vacuum chamber, where the measurement is taken.

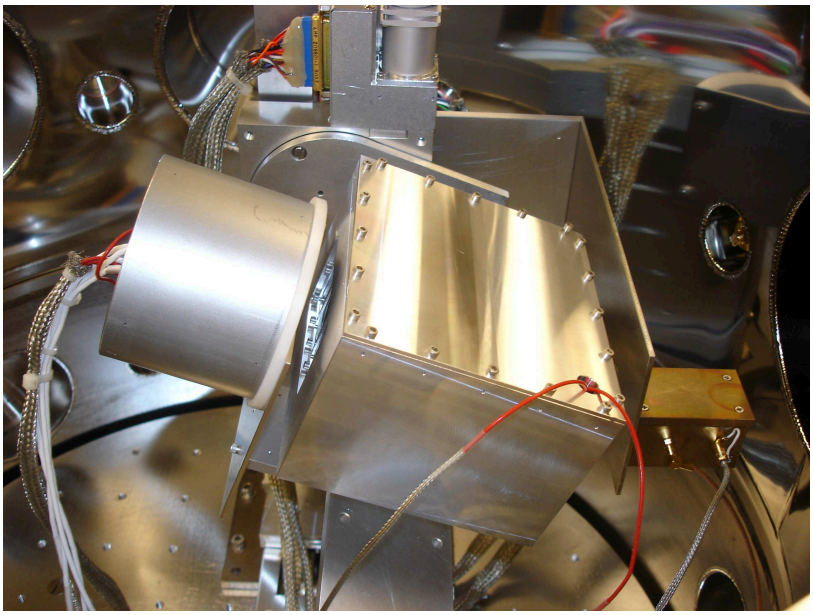

Figure 5.20: The IonSpec ESA in the vacuum chamber. The instrument faces the drift tube (far right), from which incoming ions will flow. The CEM is on the right, mounted just below the collimator slit, and the Quantar detector is mounted behind the ESA, on the left. To test with all relevant collimator angles, the instrument can be rotated through the range of 20°–30°.

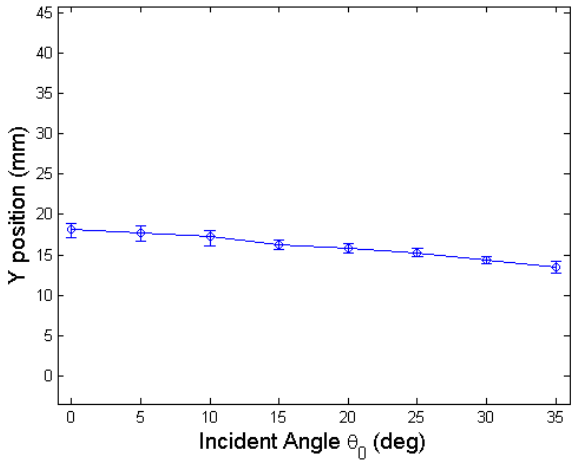

Figure 5.21: Results of the rotation-alignment test. The Quantar detector was mounted so that its MCP was colinear with the rotation axis of the motion stage. As the stage was rotated through different angles, the ion beam coming through the collimator slit was expected to remain aimed at the same spot on the detector. Over the range of 35° the beam moved by approximately 4.5 mm. For the angular range of the IonSpec ESA tests the movement was less than 1.5 mm.

extending from -141 V to -480 V and from +11.8 V to +40 V are required to allow coverage of an E/q range larger than the $(E/q)_{\max} = 3(E/q)_{\min}$ range of interest. Ions at either extreme of this range were scattered by collisions with the deflection plates or walls of the ESA. For ease of notation when plotting the data, the axes of figures were scaled such that $(E/q)_{\min} = 30$ keV/e and $(E/q)_{\max} = 90$ keV/e. Using that scaling, the E/q range of the test was from 25–85 keV/e, in steps of 5 keV/e. The 90 keV/e range was not able to be reached due to the ions impacting inside the instrument, just below the exit aperture. The 85 keV/e measurement showed a large amount of dispersion from collisions with the instrument, so was excluded from the analysis. The detailed testing log for the IonSpec deflection test measurements can be found in Appendix C.

Even though problems with dispersion and limited aperture size prevented the measurement of $E/q = 90$ keV/e ions, it was found during testing that the factor of 3 in E/q passband could still be obtained by slightly shifting the E/q range lower.

Equipment	Setting	Equipment	Setting
Beam Energy Supply	1 kV	Deflection Plates Supply	12.1 V
Beam Focus Supply	510 V	Control Box Supply	150 V
Beam Monitor	-2.5 kV	Steering Plates Supply	±5 V
Beam Control Box	4.4 A	Quantar HV Input	1.8 kV
Leak Valve	125	Magnet Supply	0.746 A
Horizontal Stage	0 mm	Vertical Stage	+25 mm
Chamber Pressure	2.8×10^{-7} Torr	Input Gas	H

Table 5.1: Equipment settings used during the IonSpec measurements. Block diagrams in Appendix B indicate the function and naming of each piece of equipment.

This small change was enough to allow the high-E/q ions to exit from the ESA and strike the detector (Figure 5.22), however the distributions are close to the edge of the detector's range at both the minimum and maximum E/q. The Quantar detector contains a stack of 2 MCPs with 40 mm diameters, and has a FWHM resolution of 0.4 mm. Measurements above ∼84 keV/e were cut off by the edge of the Quantar detector, which is outlined in red. Although the ion simulations indicated that this size of exit aperture would be sufficient for the 30–90 factor of 3 in E/q range to comfortably exit the instrument, engineering factors like geometric tolerances in the machining process and small refractions in the ion beam due to fringe fields can cause some deviations from the controlled environment of the simulation. The exit aperture of the ESA could be widened in the vertical direction by 2–3 mm to comfortably allow the full target distribution to be measured, and a detector with a larger area, or a combination of multiple detectors, could be used. The E/q range that passed through the ESA was from ∼27–82, which satisfies the goal of a factor of three.

Systematic scans through the entire range of voltages and angles were necessary for a measurement of the integrated energy-angle response of the ESA. To obtain a cleaner data set, the collimator slit was widened from 5 to 15 mm, and the high voltage bias on the Quantar detector was raised from 1.7 kV to 1.8 kV. These two modifications to the test setup led to a much improved set of measurements without

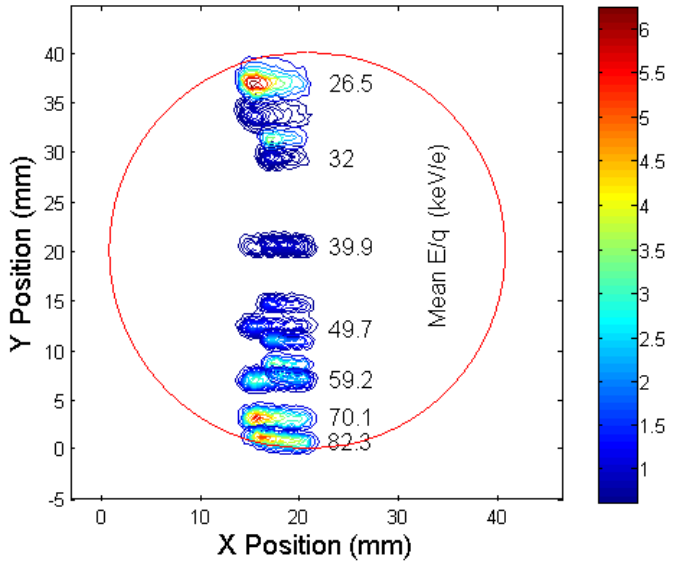

Figure 5.22: A factor of 3 in simultaneous E/q range, as detected by the IonSpec ESA.

the background noise and low count rates that are noticeable in the data shown in Figure 5.22.

Unlike the previous measurement, the widened collimator slit lead to mostly clean, distinguishable peaks on the Quantar surface, as shown in Figure 5.23. The shape of the collimator slit is clear from the buildup of particle counts. The collimator slit is 15 mm across, but a vertical grid support structure on the ESA is blocking a 3 mm section around $x = 8.5$ mm.

No attempt was made to adjust the E/q range to better fit within the bounds of the detector for this full scan. For comparison with simulation data, the initial E/q was plotted against the final position on the detector. Each data point in Figure 5.24(a) contains the sum of normalized counts s^{-1} bin^{-1} from all angles measured for that E/q. The position measurements map to the input energy with a power law fit, just as in the simulations, but with an index of 0.41. Figure 5.24(b) shows that the E/q resolution of the IonSpec ESA increases linearly with the the mean initial E/q, with error bars indicating the maximum and minimum energy resolution over a 5 mm

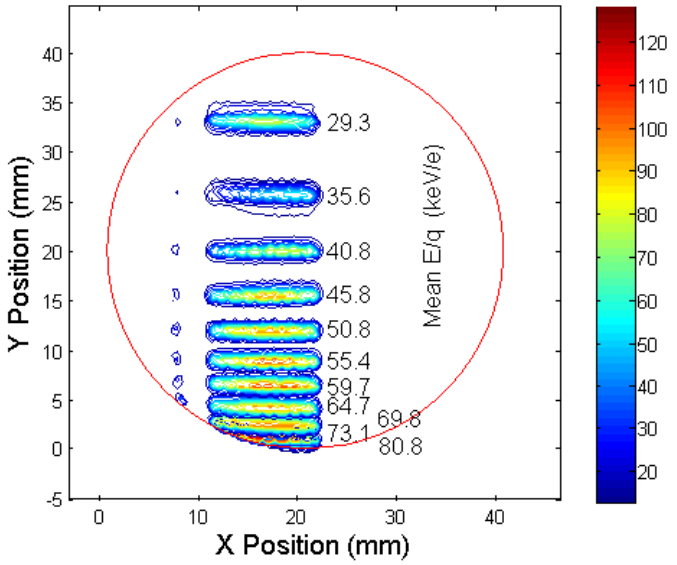

Figure 5.23: A composite image of the entire IonSpec ESA measurement run as detected by the position-sensitive anode. The MCP border is shown in red. The expected pattern and spacing of trajectories is clearly evident in the measurements. There is a cutoff at the higher E/q values due to ions focusing beyond the edge of the detector.

wide horizontal section of the detector. The slope of the linear trend is shallower than what the simulation predicted (.06% vs. .09%). This discrepency with the simulation results may be due to the Quantar being set farther back or closer toward the instrument than was simulated, or the fact that higher-E/q ions were impacting the detector at the lower edge and beyond, preventing a full distribution from being obtained in some cases (Figure 5.23). A fit to the data puts the resolution in the 30–90 E/q range at 2.9–6.7%.

Another check of the collimator slit alignment with the rotation axis was performed by comparing the impact positions of each E/q species over its range of entrance angles. A good alignment would lead to an E/q (or equivalently, vertical impact position) that does not vary much with angle. This was the case for IonSpec, thus validating that the angular rotation of the instrument accurately modeled a focused collimator (Figure 5.25).

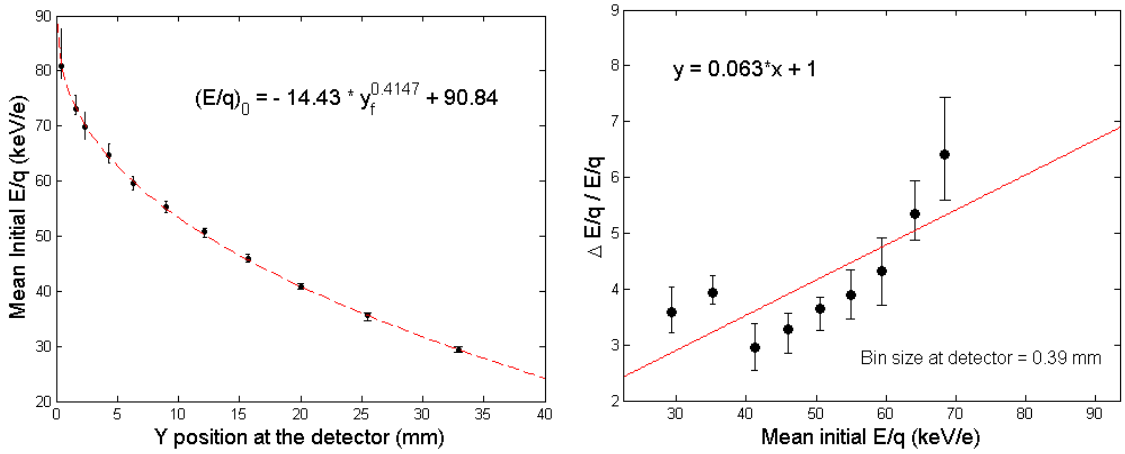

(a) (b)

Figure 5.24: Position-E/q relation and E/q resolution for the IonSpec ESA tests. (a) The mapping of initial E/q to final impact position on the detector follows a power law fit of order 0.41. (b) The E/q resolution linearly increases with mean initial E/q with a slope of 0.06 $(\text{keV/e})^{-1}$.

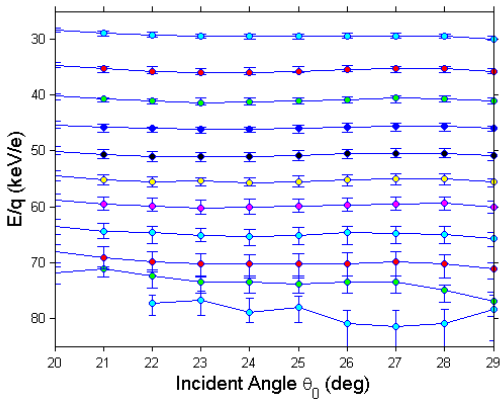

Figure 5.25: The variation of impact position over all entrance angles. The position was converted into E/q values using the empirical power law relation shown in Figure 5.24(a). The values remain relatively constant during the sweep of angles, indicating that the alignment between the collimator slit and the rotation axis of the ESA was correct, and thus the single-slit collimator functioned as a multi-slit collimator for this set of measurements. Due to impact dispersion that spread noise across the detector, two of the data points for the 80 keV/e set were removed.

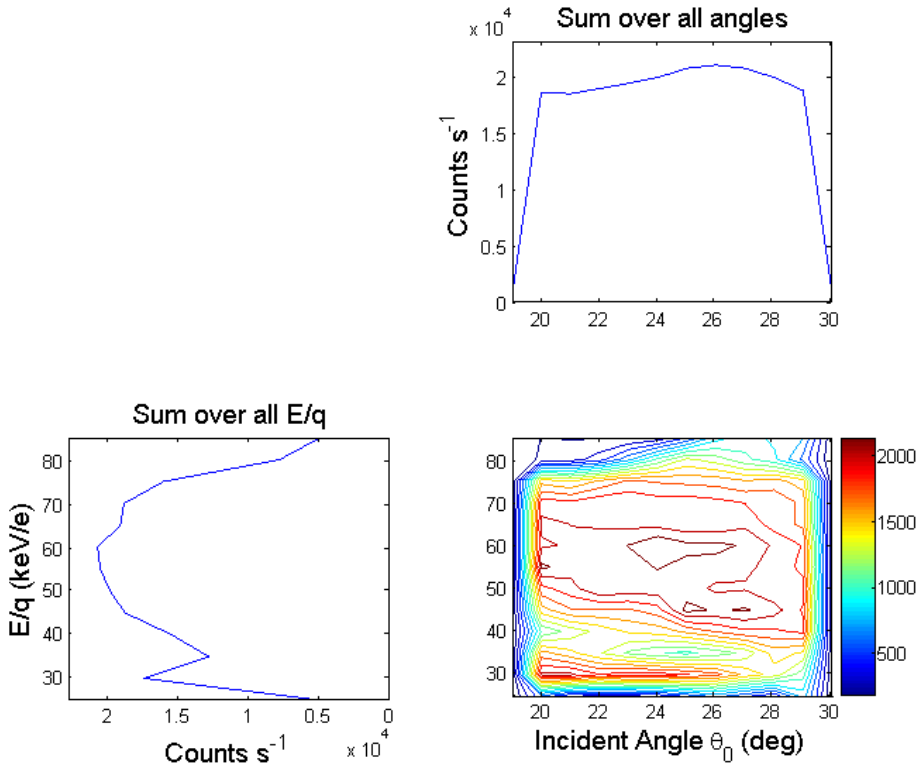

Figure 5.26: The IonSpec ESA's energy-angle response shown in a 2D histogram. The 1D histograms represent summations over the contour plot to show the total response over the full E/q and angular acceptance range.

The geometrical factor was calculated for this ESA by taking summations of a 2D histogram of E/q and incident angle θ_0 (Figure 5.26). The FWHM of each summed histogram was found, then the integrated energy-angle response (5.18) was calculated.

$$\Delta\left(\frac{E}{q}\right) = 0.9423\left(\frac{E}{q}\right) \tag{5.16}$$

$$\Delta\alpha = 9.9135^\circ \tag{5.17}$$

$$\left\langle \Delta\alpha \frac{\Delta E/q}{E/q} \right\rangle = 0.1630 \quad \text{(rad)} \tag{5.18}$$

To compare with the SWICS instruments, the entrance area of the cylindrically symmetric version of the IonSpec design was used. The effective entrance area is a projection of what a particle will see as it approaches the collimator, which is a conic section tilted between 20–30° in the case of IonSpec. The projected area of the

entrance aperture is 12.90 cm^2. This will need to be adjusted for the transmission coefficient C_t of the collimator itself once a collimator is designed. By integrating over the aperture's 60° field of view, G_E can be found:

$$G_E = A_e \left\langle \Delta\alpha \frac{\Delta E}{E} \right\rangle \int_{\Delta\beta} \cos\beta \, \mathrm{d}\beta \tag{5.19}$$

$$= 12.90 * C_t * 0.1630 * \frac{60 * \pi}{180} \tag{5.20}$$

$$= 2.20 * C_t \quad (\mathrm{cm}^2 \ \mathrm{sr}). \tag{5.21}$$

The IonSpec ESA is a novel design built on the knowledge gained through a long heritage of mass spectrometers. With its factor of 3 in E/q passband and factor of 12 in increased integrated collecting time, it is capable of providing measurements that answer some of the remaining questions about the solar system. If IonSpec were to travel on a mission with an orbit similar to that of *Ulysses*, high collecting rates and a triple-coincidence TOF system would provide a clear, low-background measurement of the isotopes of Helium to put a constraint on Deuterium and ^{3}He production in the Big Bang (*Gloeckler and Geiss*, 1996). IonSpec is also capable of measuring the velocity distributions and abundances of the solar wind with extremely high statistical precision. The populations of interstellar and inner-source pickup ions require long collecting times to build up accurate statistics, and with this instrument's high integration time and geometric duty cycle it is ideal for the task. If the IonSpec ESA is combined with TOF electronics similar to what was flown on FIPS (*Koehn et al.*, 2002; *Andrews et al.*, 2007), a 1 mm or finer position resolution could be achieved at the carbon foil, leading to high-resolution measurements across the E/q passband. With a collimator entrance of 60° x 6°, IonSpec would have a 30% larger field of view than *Ulysses*–SWICS, which, together with its larger energy-angle response, will give it a geometrical factor at least an order of magnitude higher. The FIPS electronics can provide a m/q resolution more than twice that of current instruments (*Gloeckler*

et al., 2001), and the integration time is 12x longer for each voltage step. With all of these features, IonSpec would have over 100 times the collecting power as previous instruments, making it a truly innovative tool for the future of mass spectrometry.

5.7 Future Development

The encouraging results from the testing of IonSpec's ESA provide a strong foundation on which to build the full instrument. The multi-slit collimator used on several instruments, including SWICS and CHEM (e.g., *Gloeckler et al.*, 1985, 1992) could be used for IonSpec as well, but there is room for optimization in the collimator design. It will be one of the main objectives in the development of the complete instrument to construct a collimator that provides better angular resolution, is lighter, and has a larger acceptance area than the current multi-slit versions. One idea is to etch straight grooves into the faces of thin narrow plates. The grooves are etched at angles that all focus to a point, as shown in Figure 5.27(a). Any particle or light ray that travels along one of the grooves will have a trajectory that is aimed at this focal point. Several etched plates can then be stacked together in such a way that the grooves form tunnels through which ions travel, as shown in Figure 5.27(b) and Figure 5.28. Since the length of the tunnels is related to the length of the plates, the collimator can be made smaller and less massive by shortening the tunnels. The angular spread $\pm\Delta\theta_{\rm res}$ experienced when passing through a tunnel is related to the tunnel's cross-sectional area and length x.

$$x = \frac{y}{\tan\left(\Delta\theta_{\rm res}\right)} \tag{5.22}$$

If the length of a tunnel is reduced, the etching would need to be narrower in y to avoid a loss of resolution, as shown in Equation (5.22). An advantage of this type of collimator design is that the grooves can be etched extremely close together, limited

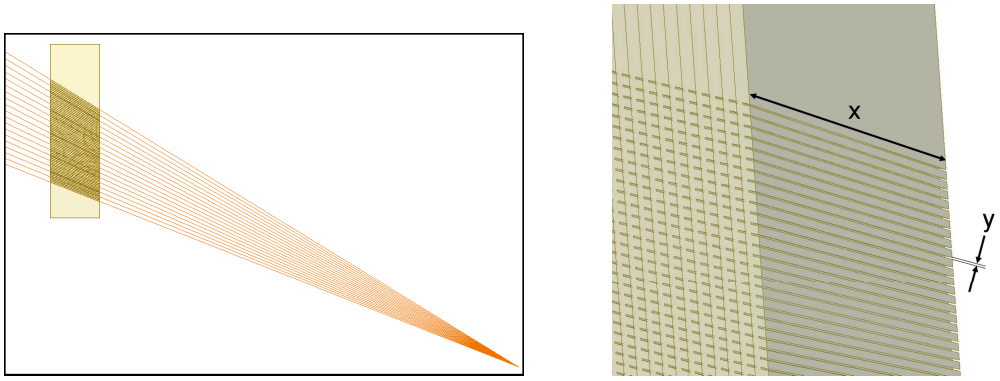

(a) (b)

Figure 5.27: A new design for a particle collimator. (a) Grooves etched into the sides of thin plates are angled from a common focal point. (b) The plates are stacked together so the grooves form tunnels through which particles can travel. The angular spread of ions that pass through a tunnel is determined by both the cross-sectional area and length of the tunnel.

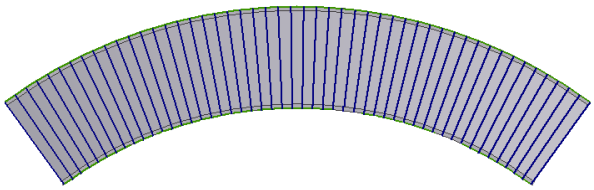

Figure 5.28: Top view of a new collimator design. Etched plates are stacked together to form a collimator that fits the outer contour of the IonSpec ESA. Particles enter from the top of the page.

only by the structural integrity of the remaining "walls", without the possibility of particles crossing from one tunnel to another as they travel through the collimator.

The light trap for IonSpec has not yet been designed in full, but to achieve adequate suppression of UV light within the instrument, a suppression factor of 10^{-7} is desired. MCPs will record a detection when hit by photons of energies $E_{\text{phot}} \geq 4$ eV (*Wüest*, 1998), creating noise in the measurement. Typically a "three-bounce" rule is followed in this type of instrument design, where light experiences diffuse reflection a minimum of three times before it enters the TOF region. In addition to a light trap design, other light-suppression techniques will be examined, such as coating the interior of the ESA with absorptive material or using specially designed filters that

block UV wavelengths of light but allow particles to pass through (*Scime et al.*, 1995; *Mukherjee et al.*, 2007).

Advances can also be made with respect to the carbon foil. Carbon foils are necessary for the generation of a start signal in the TOF analyzer, but they slow and scatter ions in the process. With the broad availability of carbon nanotubes, there may be a way to make thinner foils that are more resistant to tearing than standard foils.

To avoid the effects of fringe fields, a resistive voltage divider will be installed at the side edges of the electrostatic deflection plates. This well-established technique provides a uniform field between the deflection plates at the edges, rather than the disruptive fringe fields.

CHAPTER VI

An Optimization of LEF TOF Analyzers

6.1 The Single-Detector Mode

To measure rare particles in space, an analyzer must be able to detect the signals of these low-density populations among the signals of more populous species. An instrument needs high mass resolution to separate particles adequately, but the size and mass of the instrument should be kept to a minimum. The design discussed here provides a large improvement over existing technologies without increasing the size.

The original design for the cylindrically symmetric LEF TOF discussed in § 4.2.2 used anodes behind two separate MCP stacks to detect start and stop signals (*McComas and Nordholt*, 1990; *Young et al.*, 2004b). This design was used in the IMS sensor on *Cassini*–CAPS (*McComas et al.*, 1998), which has $m/\Delta m = 70$ (*Young et al.*, 2004b). The MCPs that generate a signal on the straight-through anode for particles such as neutrals and negative ions will provide a low mass resolution measurement. As particles traverse the carbon foil, they experience angular scattering and energy losses. They emerge from the foil with a distribution in energy values and, since the flight times for straight-through particles are energy dependent, a distribution of flight times (see Equations 4.19, 4.26, and 4.24). The mass resolution is

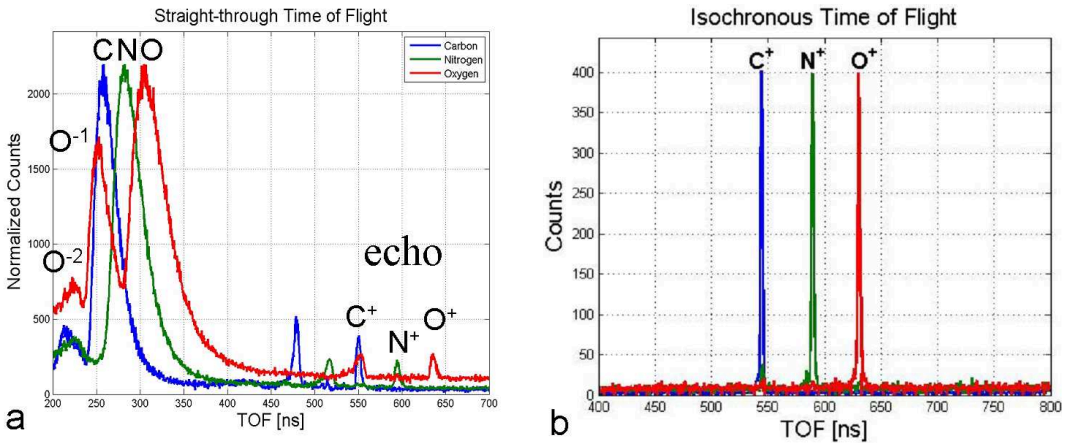

Figure 6.1: Particle measurements using the straight-through and isochronous anodes. (a) Straight-through C (*blue*), N (*green*), and O (*red*) particles have low flight times and broad distributions, with $m/\Delta m = 3.9$. Secondary electron echo peaks that match isochronous flight times are caused by ions that impact a field suppression grid above the isochronous MCP. (b) High-resolution distributions of isochronous ions have tall, narrow peaks with a mass resolution of $m/\Delta m = 137$.

related to the time-of-flight resolution by

$$\frac{m}{\Delta m} = \frac{t}{2\Delta t}, \tag{6.1}$$

where the Δm and Δt refer to the FWHM of the mass and time peaks.

The anode that positive isochronous ions will impact after their trajectories are turned around by the linear electric field is referred to as the "isochronous" anode in this dissertation. Equation 4.23 indicates that in the ideal case, when $|\mathbf{E}| \propto z$, the flight time of isochronous ions does not depend on energy, so will not be affected by scattering or deceleration in the carbon foil. The flight times for these ions tend to be sharply clustered together, creating a narrow distribution in their measured m/q. Figure 6.1 shows measurements taken with a cylindrically symmetric LEF TOF analyzer. An ion beam of $E/q = 2$ keV/e was used, with three different m/q species sent into the sensor: 12, 14, and 16 amu/e. In Figure 6.1(a) is data from the straight-through anode, which records the flight times for particles that are affected by energy

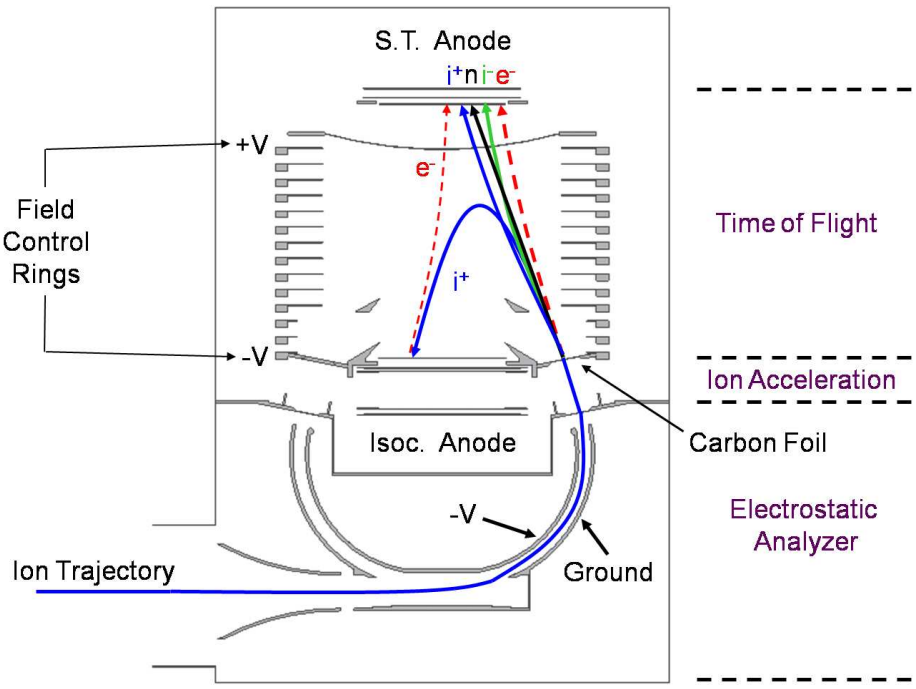

Figure 6.2: An LEF TOF system with a single anode. Positive ions hit an emissive surface and sputter off secondary electrons, which are accelerated toward the straight-through anode. The flight times for all particles can be measured with a single anode, thereby eliminating the need for the isochronous anode with its electronics, power requirements, and mass.

loss and scattering in the carbon foil. These particles have a large distribution of flight times, as can be seen by the wide peaks. The measurements from the isochronous anode are shown in Figure 6.1(b). For the measurements of the 3 species shown here, the average mass resolution of particles impacting the straight-through anode is $m/\Delta m = 3.9$, and the resolution for the isochronous anode is $m/\Delta m = 137$.

Experiments with H^+ and He^+ have shown that metals experiencing ion bombardment will emit secondary electrons of at least 1–10 electrons per ion (*Hill et al.*, 1939; *Sternglass*, 1957). In Figure 6.1(a), there are TOF peaks detected by the straight-through anode that correspond to the flight times measured by the isochronous anode in 6.1(b). These are caused by isochronous ions that impact a field containment grid above the MCPs and sputter off secondary electrons, which are accelerated toward the straight-through anode to trigger a stop signal (see Figure 6.2). The secondary

electron peaks from the field containment grid can be seen in the straight-through data as narrow peaks with the same time of flight as the isochronous ion plus the travel time of the secondary electrons.

The presence of secondary electron peaks in the straight-through anode's measurements has led to a modified design for cylindrically symmetric LEF TOF instruments. The isochronous MCPs and anode are replaced by an emissive plate that generates secondary electrons upon ion impact. *Yokota et al.* (2005), for example, used an MgO-coated copper beryllium plate for their development of a single-anode LEF TOF instrument. These secondary electrons are accelerated toward the straight-through MCP and create a stop signal. This "echo peak" of isochronous positive ions on the straight-through anode retains the high mass resolution and allows the measurements to be taken with fewer parts and electronics in the analyzer. The single-anode version was built into the PEPE instrument and flown on *Deep Space 1* (*Young et al.*, 2007), and has been improved upon by *Yokota et al.* (2005) and *Gilbert et al.* (2007a).

When a cylindrically symmetric LEF TOF analyzer is operated in a low-resolution, single-anode mode, there is a risk that the high-resolution capabilities will be lost (*Young et al.*, 2004a). The percentage of ions exiting the carbon foil with a positive charge state (i.e., the isochronous particles) increases with increasing energy. Unless a high enough post-acceleration voltage is used, there will not be many isochronous particles relative to the straight-through particles, and the high-resolution isochronous measurement will be buried in the statistical noise. The single-anode version of the LEF TOF analyzer was pioneered on the mission to the comet 19P/Borrelly in 2001, and due to a high voltage discharge in the instrument it was unable to reach voltages sufficient to clearly measure the isochronous peaks in the data (*Nordholt et al.*, 2003).

Using a single-anode mode LEF TOF sensor with an aluminum plate in place for secondary electron generation (Figure 6.3), data was taken for several m/q species. Figure 6.4 shows the results of $m/q = 12$ amu/e for a 4 keV ion beam. Before reaching

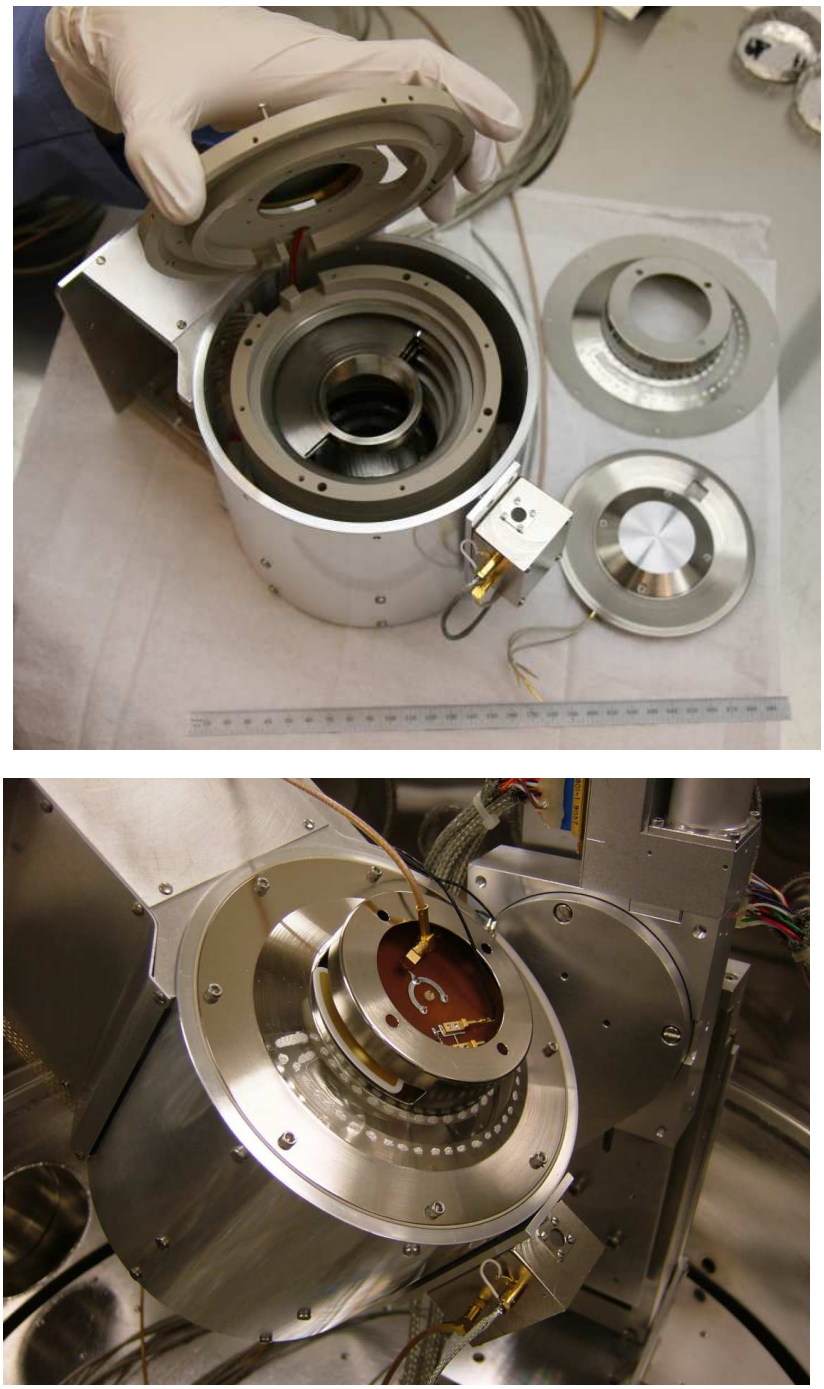

Figure 6.3: The cylindrically symmetric LEF TOF sensor used in this research. (*top*) The field control rings and straight-through anode are visible inside of the instrument, and the plate for secondary electron generation is located next to it. (*bottom*) The sensor as it was mounted in the vacuum chamber during testing.

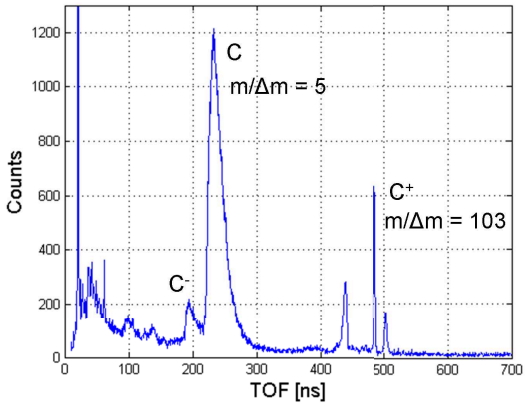

Figure 6.4: Single-anode measurements of $m/q = 12$ amu/e ions. The post-foil charge states of negative ions, neutrals, and positive isochronous echo peaks are all visible. Additional peaks in the spectra are from ion collisions with structural pieces inside the TOF cylinder. The mass resolution is $m/\Delta m = 5$ for the neutral peak, and $m/\Delta m = 103$ for the isochronous ions.

the carbon foil, the ions were post-accelerated by an additional 8 keV. Upon entering the TOF chamber, they encountered a 12 kV electrostatic field. Positive ions with near 12 keV in E/q traveled almost to the top of this field before finally being reversed in direction. The neutral peaks and isochronous echo peaks are clearly distinguished, as well as some echo "noise" that resulted from ions colliding with the field control rings and generating secondary electrons.

When a molecule passes through the carbon foil, it will break apart into its atomic daughter products. Each daughter atom will retain the same center-of-mass velocity as the parent, minus any energy loss due to straggling in the foil (*Young et al.*, 2007). This means that the daughter atoms will split their parent molecule's energy E_p in proportion to their mass fraction, as shown in Equation 6.3.

$$E_p = \sum E_d \tag{6.2}$$

$$\Rightarrow \frac{1}{2}\frac{m_p}{q}v^2 = \frac{1}{2}\frac{\sum m_d}{q}v^2 \tag{6.3}$$

The subscripts in the equation refer to the parent (p) and daughter (d) particles. An

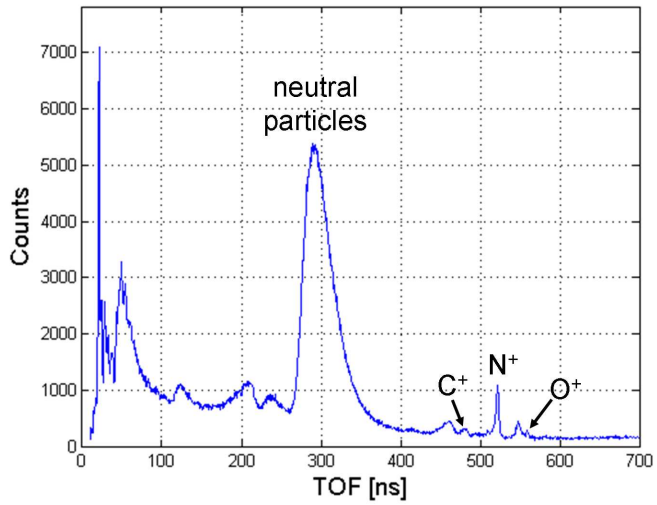

Figure 6.5: Single-anode measurements in an LEF-TOF instrument for $m/q = 28$ amu/e molecules. The majority of post-foil particles are neutral, with a flight time centered around 290 ns. The TOF for the daughter product N^+ is centered near 522 ns.

analysis of Equations 4.19–4.26 shows that the straight-through particles will each have the same TOF as their parent molecules. This characteristic leads to a useful technique for determining the parent molecule from the daughter products.

When timing electronics are used that can record multiple stop signals for a single start, the measuring of multiple daughter atoms from the same parent molecule becomes possible. For this research, specialized timing electronics that implement a time-to-digital converter in a field-programmable gate array (FPGA) chip were used (*Rogacki*, 2007). The FPGA has an internal delay line and automatically compensates for variations in propagation due to temperature and supply voltage, allowing active signal processing 100% of the time. This specialized timing circuit also has the ability to record multiple stop events for the same start event, allowing the daughter products of molecules that break apart at the carbon foil to be examined. Measurements were made with the goal of distinguishing parent molecules of similar masses (i.e., CO and N_2, which are both 28 amu) by examining their daughter products. Figure 6.5 shows a TOF measurement of molecules with initial $m/q = 28$ amu/e. The gas CO_2 was input to the ion source, and there was residual N_2 in the vacuum

chamber. Electron impact ionization takes place inside the ion source that breaks the CO_2 apart into mostly atomic ions C^+ and O^+, and the CO^+ molecular ion. The ions are then accelerated through the Einzel lens and Wien filter (Figure 5.19) up to an energy of 3 keV. At the Wein filter the m/q value of 28 amu/e was selected and the ions were post-accelerated through an additional 8 kV before impact with the carbon foil of the TOF system. The voltage inside the TOF chamber rose 12 kV between the carbon foil and the straight-through MCP. Assuming some energy loss in the carbon foil, the neutral time of flight for a $m/q = 28$ particle is:

$$\begin{aligned} t_{28\mathrm{n}} &= \lambda_2 \sqrt{\frac{m_{28}}{2E_{28\mathrm{int}}}} \\ &= 0.09579 \sqrt{\frac{28 * 1.66E^{-27}}{2 * (11000 - (-8000) - 3000) * 1.6E^{-19}}} \qquad (6.4) \\ &= 289 \text{ (ns)}. \qquad (6.5) \end{aligned}$$

All daughter products (C, N, and O) will have the same straight-through TOF as the parent molecule. For example, Oxygen has a mass fraction from CO of $16/28 = 57.14\%$, so it will receive that fraction of the parent molecule's energy while Carbon will get the rest. The flight time of the daughter product O is:

$$\begin{aligned} t_{\mathrm{n_O}} &= \lambda_2 \sqrt{\frac{\mathrm{m_O}}{2E_{\mathrm{Oint}}}} \\ &= 0.09579 \sqrt{\frac{16 * 1.66E^{-27}}{2 * .5714 * (11000 - (-8000) - 3000) * 1.6E^{-19}}} \qquad (6.6) \\ &= 289 \text{ (ns)}. \qquad (6.7) \end{aligned}$$

The same calculation can be performed for each charge state of the straight-through post-foil daughter products for Oxygen, Carbon, and Nitrogen, each with a TOF equivalent to the parent molecule. The one difference between times of flight for parents and daughter products is in the positive isochronous flight time, which is only

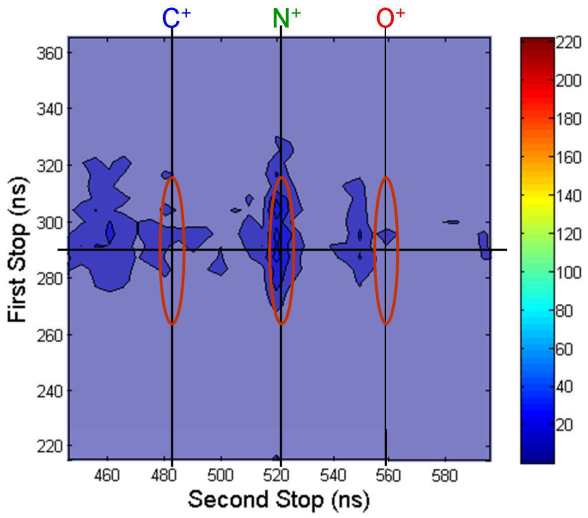

Figure 6.6: Parent molecules of $m/q = 28$ amu/e determined by their LEF daughter products. The TOF for the abundant neutral particles is indicated with a horizontal line, and the calculated TOF for each isochronous daughter product is shown with a vertical line. The N^+ peak is clear, indicating a strong N_2^+ parent composition. The daughter products of C^+ and O^+ did not have sufficient statistics in this measurement to be seen above the noise. The peaks to the left of C^+ and O^+ are from secondary electrons ejected by the N^+ ions at unintended parts of the instrument.

dependent on the m/q. The isochronous echo peaks visible in Figure 6.5 correspond to the calculated TOF for C^+, N^+, and O^+.

If the TOFs of daughter products are plotted against each other in a 1st-stop-signal vs. 2nd-stop-signal graph, the parent molecules become apparent. Figure 6.6 shows the flight times of neutral daughter products versus isochronous daughter products for a parent m/q of 28 amu/e. The clear peak for N^+ indicates that there were N_2^+ parent molecules in the original plasma. The peaks for C^+ and O^+ can also be seen, but were not in sufficient numbers to stand out from the noise. The peaks to the left of C^+ and O^+ are from secondary electrons ejected by N^+ ions that impact places in the instrument other than the isochronous target plate. Ion simulations have shown that these peaks are due to physical parts that interfere with the ions' path of travel, such as specific field control rings (*Panning*, 2007, unpublished simulations). The same two peaks can be seen surrounding the isochronous measurement of the C^+ ion

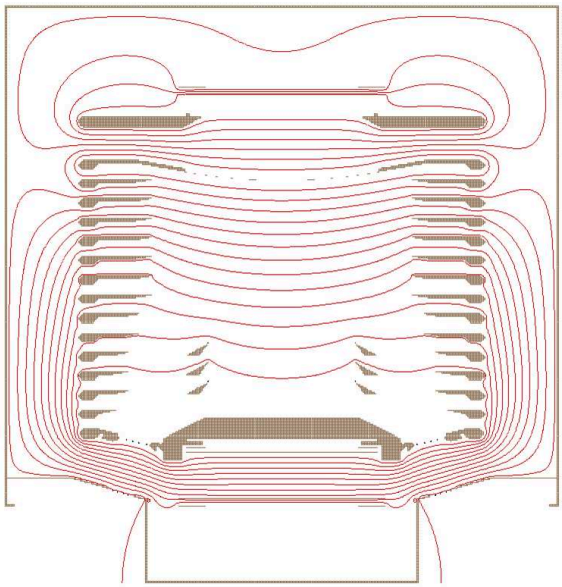

Figure 6.7: A modification to the LEF TOF design to keep the electrostatic fields linear. Smaller field control rings were added just above the isochronous MCP, with voltages equal to the outer rings in the same plane. Electrostatic field contours are shown in red.

in Figure 6.4. A future revision in the design of this particular LEF TOF instrument will require changing the geometry slightly to 'clear the path' for the particles to avoid these spurious echo peaks.

6.2 Secondary Electron Focusing

With a structural modification to the original LEF TOF design of *McComas and Nordholt* (1990), an improved operational mode can be achieved in which the high-resolution measurement can be separated from the background in a single-anode configuration by use of position-sensitive detection. This will provide the low mass and power advantages of the single-anode design with the high resolution of the double-anode design.

Additional, smaller field control rings were added in the center of the instrument just above the area of isochronous impact. The voltages on these inner rings are equal to the outer rings that are in the same horizontal plane. The original purpose

of these inner rings was to keep the electrostatic fields as linear as possible across the TOF chamber so that the ions would experience a full linear electric field during their journey (Figure 6.7). An additional effect of the inner rings was that the newly shaped field focused the secondary electrons that were sputtered off of the isochronous plate. By using position-sensitive electronics to isolate the central region of the straight-through anode, these secondary electrons can be separated from the rest of the straight-through particles and analyzed as high-resolution measurements. Figure 6.8 shows the trajectories of secondary electrons without (a) and with (b) the inner rings.

The electrons' unique focused location makes them distinguishable from all other particles regardless of the flux of straight-through particles from the foil. Even though only one anode is used, the ability to resolve high-resolution isochronous measurements is retained. Figure 6.9 shows Monte Carlo simulations of focused secondary electrons, as detected by the straight-through anode. The isochronous signal on the anode is contained in a sharp peak with a FWHM of 1.0 mm. When all flight times recorded by the anode are plotted in Figure 6.10(a), the neutral, negative, and isochronous peaks can clearly be seen, but the isochronous TOF has a low amplitude compared to the others. When the inner 2 mm diameter circular area of the anode is examined, however, the isochronous peak dominates over all others, as shown in Figure 6.10(b). This illustrates that the noise from other particles impacting in the inner space is not overpowering the signal from the isochronous particles.

To demonstrate the secondary-electron focusing ability, the LEF TOF analyzer was equipped with a position sensitive anode behind the straight-through MCP. Measurements were made for a particle beam of energy 4 keV and $m/q = 12$, with a post-acceleration voltage of 8 kV. The flight times of the ions were studied, as well as their locations of impact on the detector. Figure 6.11 shows the impact positions on the straight-through anode, with the broad neutral and centered isochronous peak

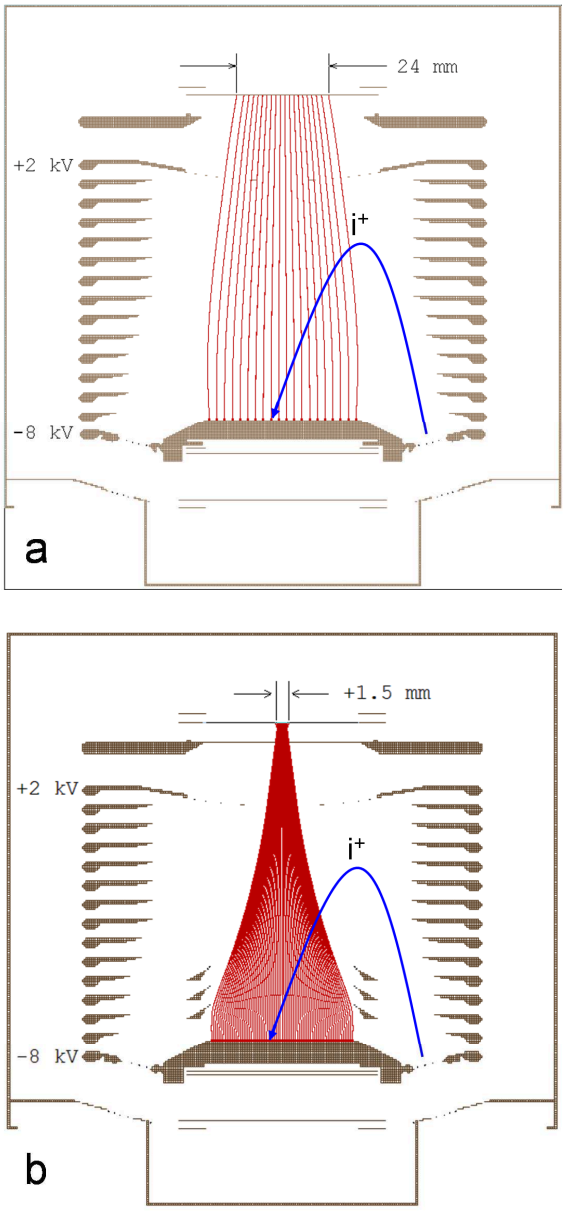

Figure 6.8: Simulation of the focusing of secondary electrons (*red*) in a cylindrically symmetric LEF TOF analyzer. Particles that exit the carbon foil with a positive charge (*blue*) will impact a metal plate, creating secondary electrons. (a) The sensor without inner rings does not show any substantial focusing of secondary electrons. (b) With inner focusing rings, the secondary electrons are guided toward the center of the MCP to generate stop signals. They can be distinguished from the stop signals of neutral and negative particles by a position-sensitive measurement.

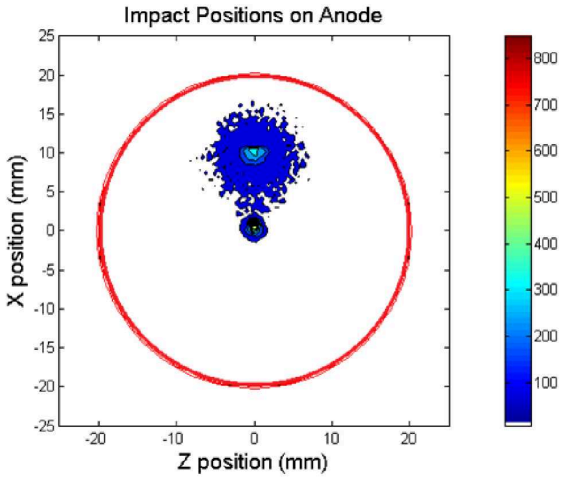

Figure 6.9: Monte Carlo simulations of secondary electron focusing. In this contour image of the straight-through anode, the broad neutral peak is visible as well as the centered isochronous echo peak, which has a FWHM of 1.0 mm.

visible. In this measurement, the isochronous peak has a FWHM of 3.97 mm. Figures 6.12(a) and 6.12(b) show the TOFs for the entire anode and for a central area of diameter 4 mm, respectively. The isochronous peak is not a large component of the total measurement, but dominates over the other peaks when the central area of the anode is examined.

6.3 Discussion

By using timing electronics that can record multiple stop events for a single start event, the daughter products of molecules can be analyzed. Plotting the flight times of two daughter products on opposite axes will create a 2D histogram that allows for quick identification of the parent molecule. In the example of CO and N_2, both of which have masses of 28 amu, the parent molecules were clearly identifiable from the daughter products.

To retain the high-resolution capabilities of a double-anode sensor using only a single-anode design, the focusing of secondary electrons from the isochronous impact is necessary. This focusing can be accomplished by adding inner rings with voltages

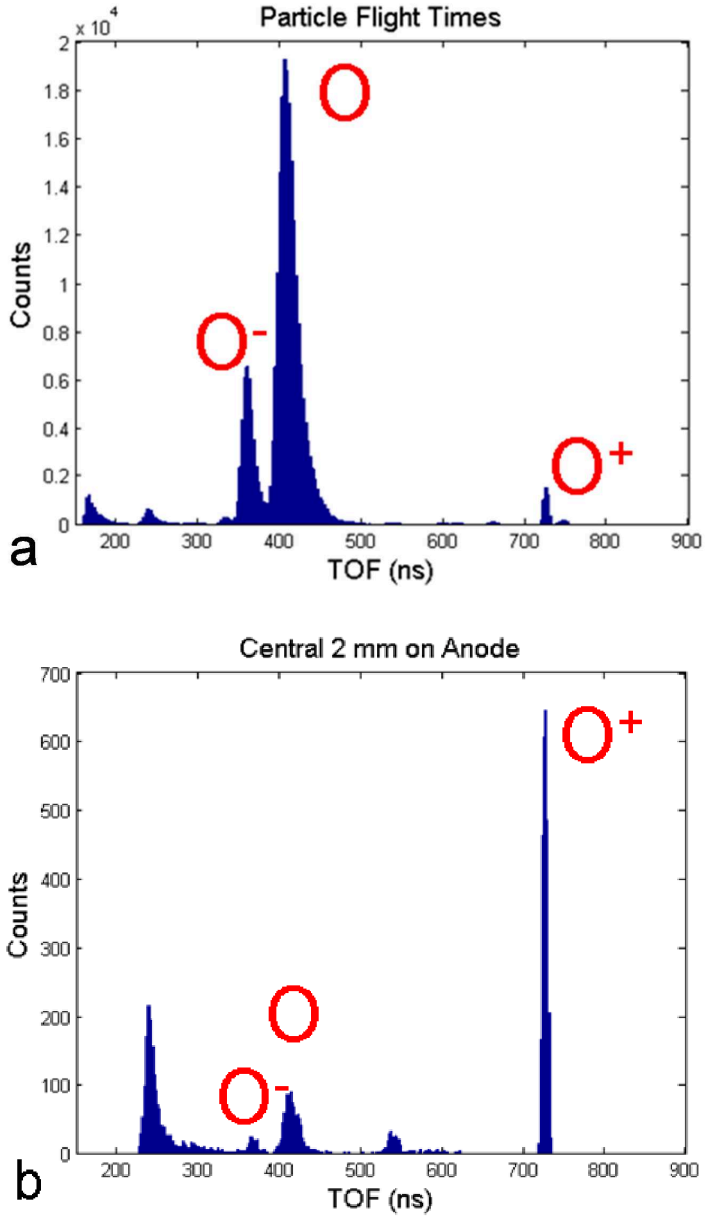

Figure 6.10: Flight times from Monte Carlo simulations of secondary electron focusing. (a) When flight times across the entire anode are examined, the neutral and negative peaks dominate. (b) If a circular area of 2 mm diameter in the center of the anode is examined, the main peak is that of focused secondary electrons.

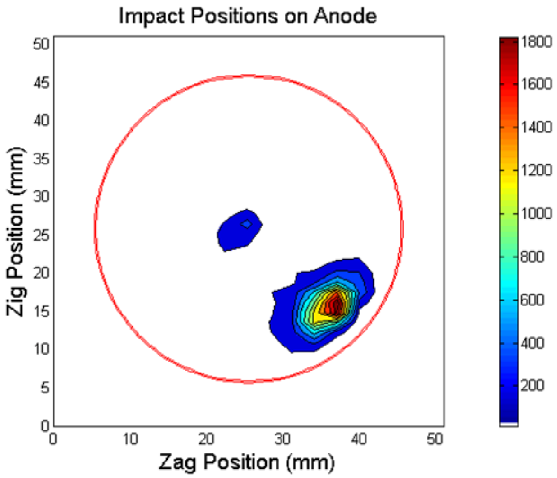

Figure 6.11: Measurement of secondary electron focusing in an LEF TOF sensor. The broad neutral peak and the centered isochronous echo peak can be seen in this contour image of the straight-through detector. The isochronous peak has a FWHM of 3.97 mm.

equal to those of the outer rings in the same horizontal plane. The isochronous flight times can be extracted from the data using position-sensitive electronics to separate a certain central area of the detector from the rest, or by using a completely separate anode for the region of interest. Simulation and measurement have shown that the electrons tend to focus in a circular region near the center of the anode. In scenarios where a measurement contains large peaks of other species that overlap or drown out the isochronous peaks, the isochronous measurements can be retrieved based purely on the impact position of secondary electrons.

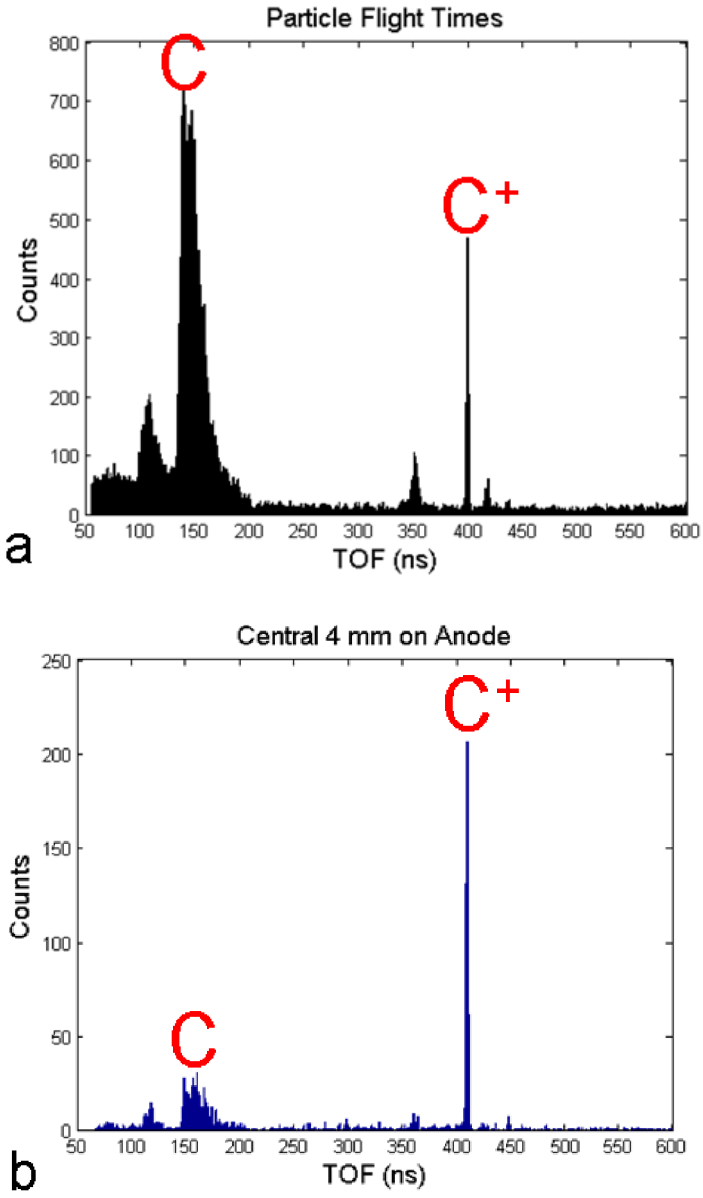

Figure 6.12: Flight times for secondary electron focusing measurements. (a) TOF peaks for the entire anode show the neutral, negative, and isochronous peaks. (b) When the inner area of 4 mm diameter is examined, the peak of secondary electrons focused from the isochronous ions is clearly visible above all others.

CHAPTER VII

Conclusions

7.1 Conclusions

This dissertation has presented new tools and techniques for studying the space environment and improving what is known about the fundamental physics that govern it. Basic knowledge such as the contributions of pickup ions and the sources of the streamer wind provide the foundation necessary to better understand and forecast space weather. With the methods discussed here, some of the unsettled questions in heliospheric physics may be answered.

In Chapter II some of the current questions in space plasma physics were enumerated. The origin of the slow, hot, streamer wind is still a topic of active debate, and an understanding of it will lead to knowledge of particle transport and acceleration throughout the corona. There is no current consensus on the exact origin of the streamer wind, or on the nature of its heating and acceleration. The new mapping technique for the open magnetic flux of the Sun explained in Chapter III provides a way to calculate where a photospheric footpoint of open flux will map to in the heliosphere. Since the solar wind carries open magnetic flux out to space, the technique can act as a mapping tool for the wind. If a spacecraft were to detect a boundary between coronal hole and streamer solar wind, the amount of distributed open flux on the Sun can be adjusted until the model expands the solar flux to the measured

boundaries. This can put a quantitative value on the amount of distributed flux on the Sun, and therefore a constraint on the streamer wind origin for some theories (*Fisk*, 2003).

The composition of the solar wind is also a vital piece of the puzzle. Certain ratios of ions in the solar wind can give clues to the physical processes occurring within the corona. With the development of a new electrostatic analyzer with a large E/q passband (Chapter V), measurements can be performed over longer integration times. If IonSpec were to travel in a polar orbit similar to *Ulysses*, the signals of low-density particles could be more clearly seen through the noise with IonSpec's large improvement in collecting power. The creation of inner-source pickup ions such as O^+ and C^+, as well as the population of $^3He^+$ pickup ions that trace the amount of matter in the early universe (*Gloeckler and Geiss*, 1996), are two areas of research for which IonSpec would be able to provide useful measurements. When compared to its predecessors, CHEM and SWICS, IonSpec has a dramatically increased collecting power without an increase in size. The sensitivity of this improved design will enable new measurements that can open the doors to formerly unexplored areas of research.

The issue of low signal-to-noise detection of isochronous flight times in the single-anode versions of the LEF TOF analyzers can be solved with the improvement discussed in Chapter VI. The focusing of secondary electrons to a concentrated spot on a position-sensitive anode will allow these types of instruments to have lower mass and power requirements without the requisite sacrifice in resolution.

7.2 Future Work

The utility of the open flux mapping technique has only begun to be explored. The open flux will be modeled over several Carrington rotations to calculate the amount of distributed flux required to align modeled coronal hole boundaries with measured ones. The results will be analyzed for trends that may provide clues to the streamer

wind origin. An investigation will also look into the ability of the mapping technique to calculate solar wind speeds, rather than relying on the non-physical expansion factor technique used by some today (*Arge et al.*, 2004; *Wang and Sheeley*, 1990).

The IonSpec instrument is still in an early stage of development. A collimator will be developed that maintains the position resolution of the ESA and that provides a large open area. The ESA needs an efficient light trap to keep UV light out of the TOF region. The design and testing of a light trap will lead to a suppression factor such that for every 10 million photons that enter the instrument, only one will successfully pass through the ESA. A resistive divider network for the mitigation of fringe fields will also be modeled and added to the deflection plate assembly. The entire ESA will be designed with the cylindrical-wedge shape to increase the field of view and prepare it for the addition of a TOF section.

The cylindrically symmetric LEF TOF instrument with secondary electron focusing requires some minor modifications to the inner geometry to eliminate the spurious echo peaks from ion collisions with field control rings. Some similar instruments have eliminated the rings altogether, replacing them with a high-resistance coating on the inner surface of a ceramic wall to create the linear electric field (*Young et al.*, 2007; *Balsiger et al.*, 2007). With optimizations to the design of the LEF TOF to eliminate the unwanted peaks, and with the position-sensitive detection ability for the identification of isochronous peaks, this analyzer will exceed the mass resolution of similar instruments and make groundbreaking discoveries of the plasma in space.

The research presented here provides new tools to unlock some of the mysteries of space. It is only through continual innovation and by building on the inspired developments of the past that new models and novel instruments can be developed. Each small discovery leads to a better understanding of the space environment, and an improved ability to accurately forecast space weather.

APPENDICES

APPENDIX A

Two-Dimensional Crank-Nicolson Scheme for a Uniform Spherical Grid

For the diffusion process, Equation 3.9 was solved using an implicit two-dimensional Crank-Nicolson scheme, which is unconditionally stable and second-order accurate in both time and space (*Crank and Nicolson*, 1947). In the conventional notation, the two-dimensional numerical scheme using central differencing can be written for a uniform Cartesian grid as

$$\begin{aligned}(1+2\mu)\,u_{i,j}^{t+1} - \frac{\mu}{2}\left(u_{i+1,j}^{t+1} + u_{i-1,j}^{t+1} + u_{i,j+1}^{t+1} + u_{i,j-1}^{t+1}\right) \\ = (1-2\mu)\,u_{i,j}^{t} + \frac{\mu}{2}\left(u_{i+1,j}^{t} + u_{i-1,j}^{t} + u_{i,j+1}^{t} + u_{i,j-1}^{t}\right),\end{aligned} \tag{A.1}$$

where $u_{i,j}^{t}$ is the value of the parameter undergoing the diffusion (B_r in this case) at position (i,j) at time t. The von Neumann number on a uniform grid is $\mu = \xi\Delta t/\left(\Delta x\right)^2$, where the size of the grid square is Δx on each side, and the diffusion coefficient ξ describes the speed at which the mathematical diffusion takes place. When deriving the two-dimensional Crank-Nicolson scheme in spherical coordinates, the von Neumann number is written as $\mu = \xi\Delta t/\left(r\Delta\theta\right)^2$, where $\Delta\theta = \Delta\phi$, and the cosine is replaced by the central difference of the sine to remain consistent with the discrete nature of the other terms. Care must be taken at the poles, where the central

differencing is replaced by forward or backward differencing. To keep second-order accuracy with forward or backward differencing, the series must be carried out to higher-order terms in the derivation. The two-dimensional numerical scheme using central differencing can be written for a uniform spherical grid as

$$\left(1+\mu+\frac{\mu}{\sin^2\theta_{i,j}}\right)u_{i,j}^{t+1}-\frac{\mu}{2}\left[1+\frac{(\sin\theta_{i+1,j}-\sin\theta_{i-1,j})}{4\sin\theta_{i,j}}\right]u_{i+1,j}^{t+1}$$
$$-\frac{\mu}{2}\left[1-\frac{(\sin\theta_{i+1,j}-\sin\theta_{i-1,j})}{4\sin\theta_{i,j}}\right]u_{i-1,j}^{t+1}-\frac{\mu}{2}\frac{1}{\sin^2\theta_{i,j}}u_{i,j+1}^{t+1}-\frac{\mu}{2}\frac{1}{\sin^2\theta_{i,j}}u_{i,j-1}^{t+1}$$
$$=\left(1-\mu-\frac{\mu}{\sin^2\theta_{i,j}}\right)u_{i,j}^{t+1}+\frac{\mu}{2}\left[1+\frac{(\sin\theta_{i+1,j}-\sin\theta_{i-1,j})}{4\sin\theta_{i,j}}\right]u_{i+1,j}^{t+1}$$
$$+\frac{\mu}{2}\left[1-\frac{(\sin\theta_{i+1,j}-\sin\theta_{i-1,j})}{4\sin\theta_{i,j}}\right]u_{i-1,j}^{t+1}+\frac{\mu}{2}\frac{1}{\sin^2\theta_{i,j}}u_{i,j+1}^{t+1}+\frac{\mu}{2}\frac{1}{\sin^2\theta_{i,j}}u_{i,j-1}^{t+1}. \quad \text{(A.2)}$$

Although it is unconditionally stable, a marching scheme such as this will depend on the value of μ for its accuracy. A lower choice of μ will lead to a more accurate solution at the expense of computational resources (i.e., a smaller time step Δt), while a higher value of μ will arrive at a solution more rapidly but with less accuracy (a larger time step). In this model, the value of the coefficient ξ describes the speed of the mathematical relaxation and, since it does not describe a physical process, can be chosen arbitrarily. Thus the only restriction for this scheme will lie in keeping μ small for accuracy and assigning either ξ or Δt. It can be seen that when μ is held constant, any choice for either ξ or Δt will lead to the same solution. A value of $\mu = 1/4$ was chosen, with an arbitrary time step of $\Delta t = 0.1$ s, and studied several different grid resolutions, with a grid size of 2.5° x 2.5° (72 x 144 grid spaces) on a uniform spherical grid used for the comparisons in this paper. The relaxation was allowed to continue on a sphere of $r = R_\odot$ until the difference in magnetic field magnitude between any cell and its neighbor was of order $10^{-1}\mu T$.

APPENDIX B

Mechanical Drawings, CAD Models, and Block Diagrams

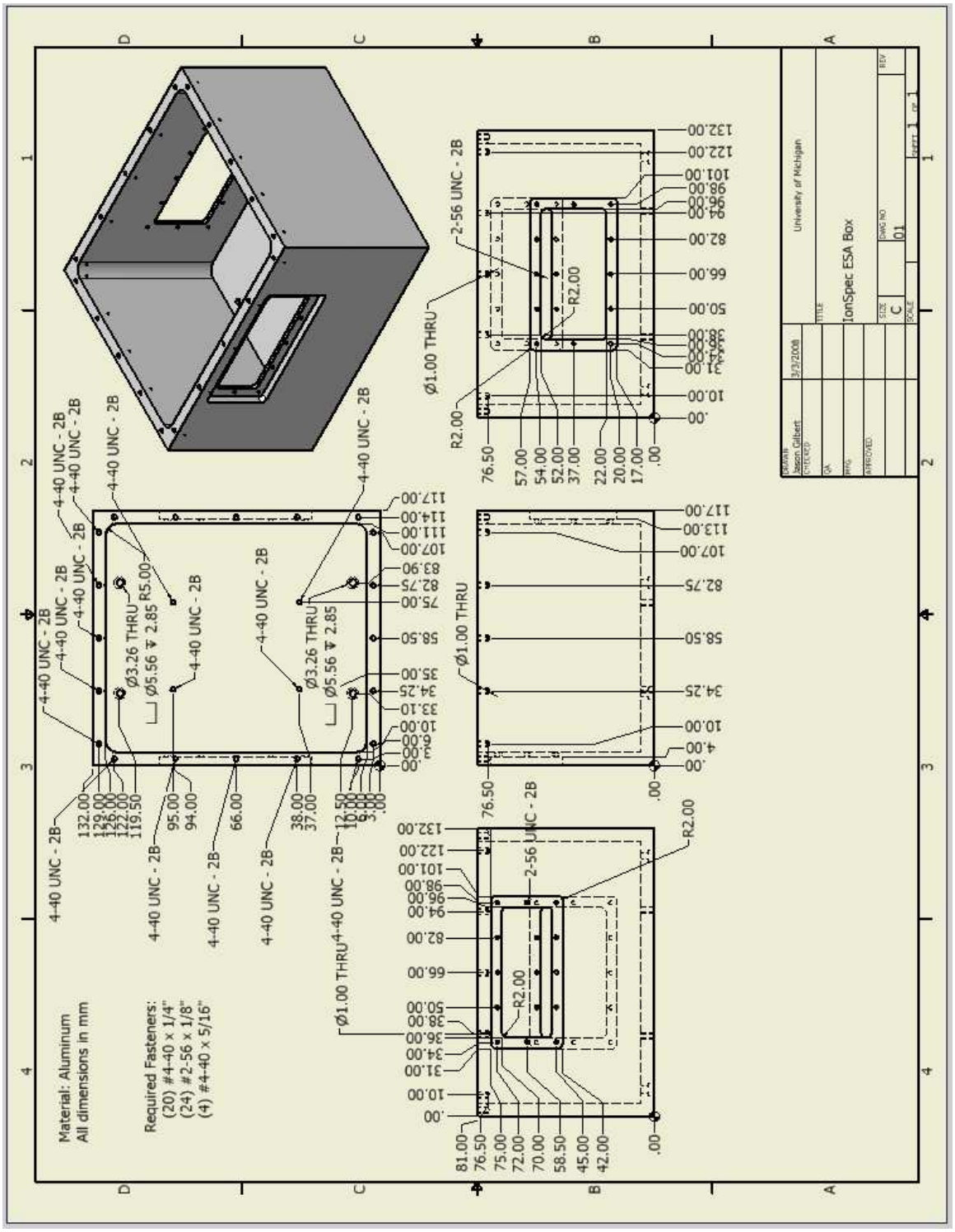

Figure B.1: The IonSpec ESA housing.

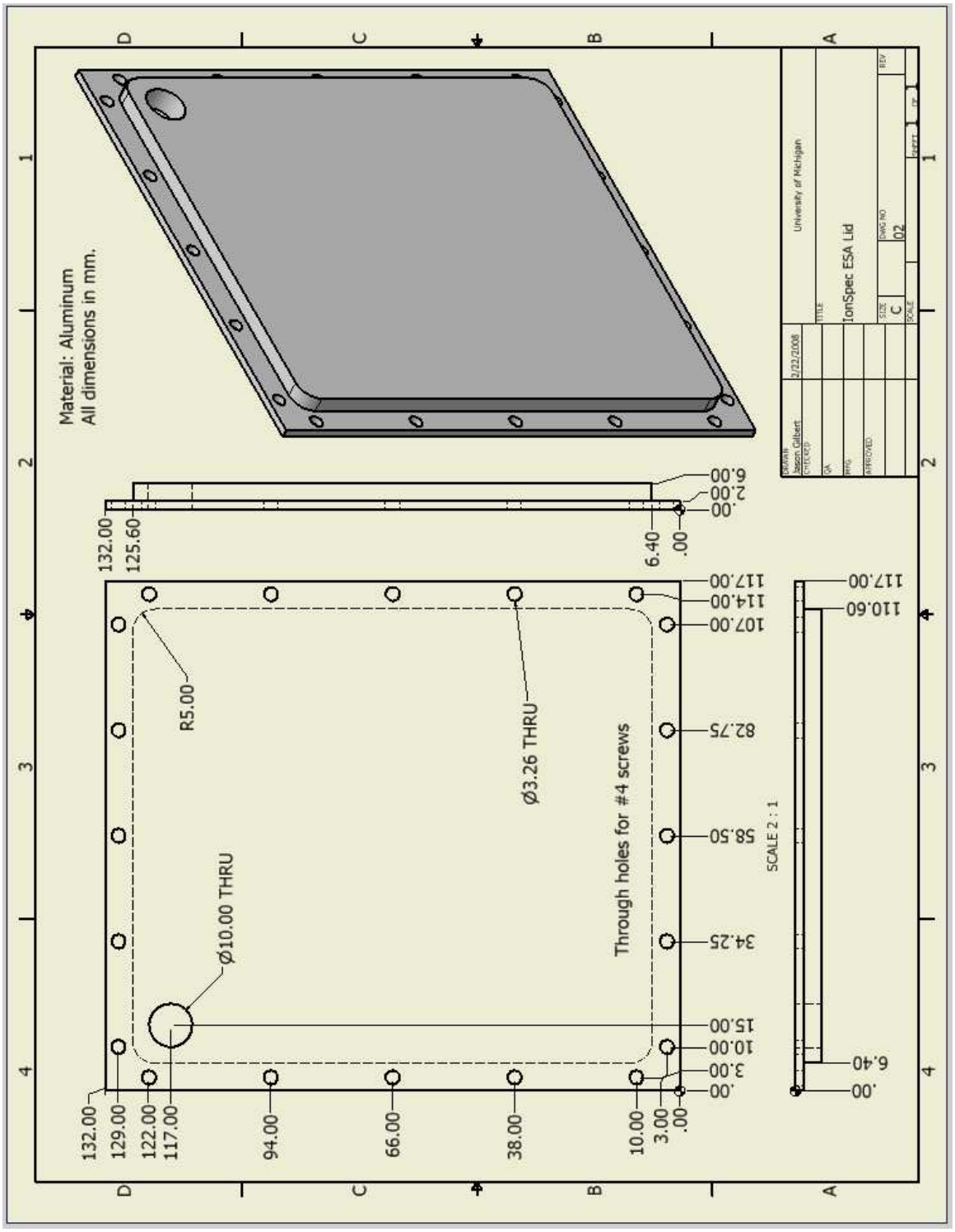

Figure B.2: The lid for the IonSpec ESA housing.

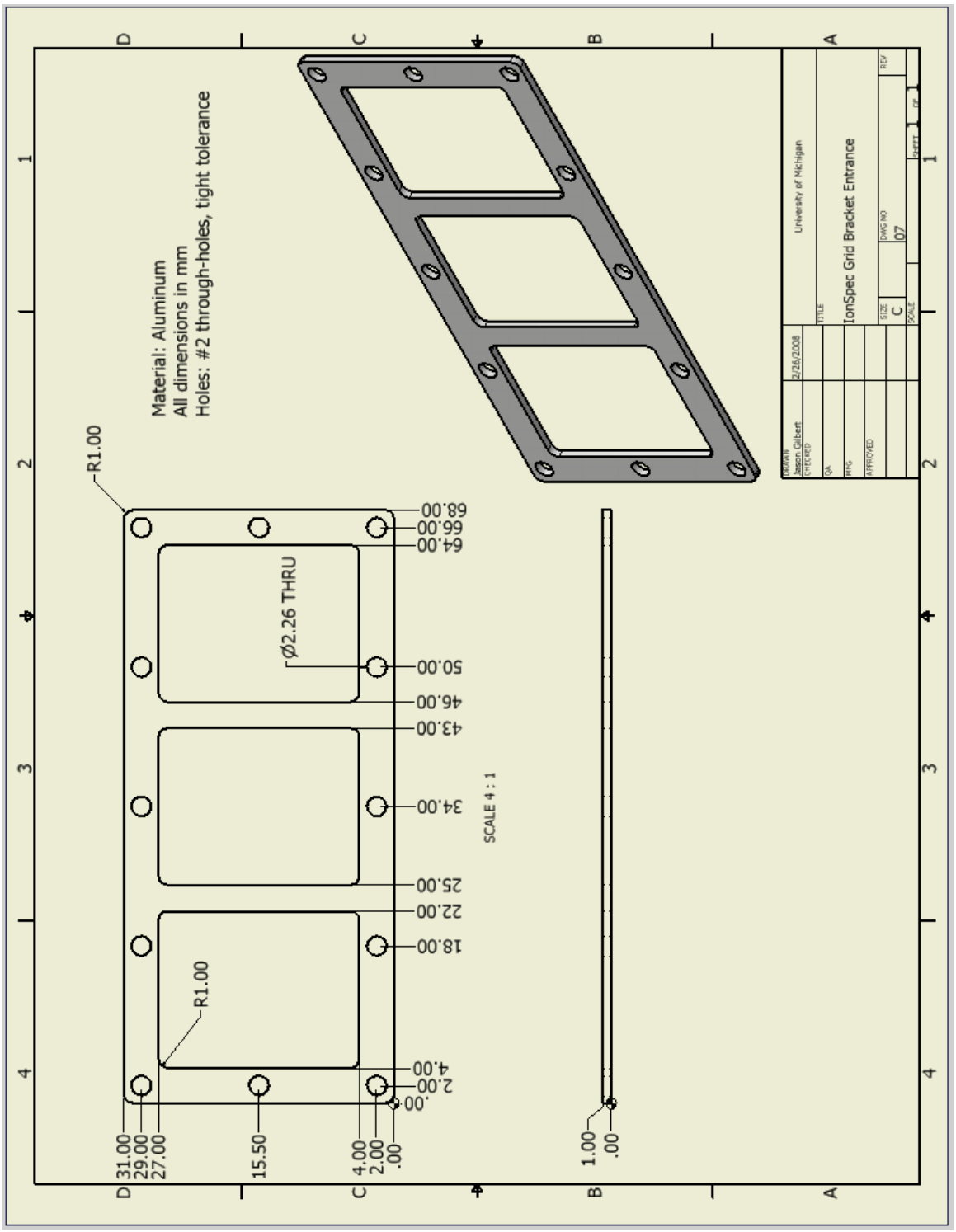

Figure B.3: The IonSpec entrance aperture field control grid.

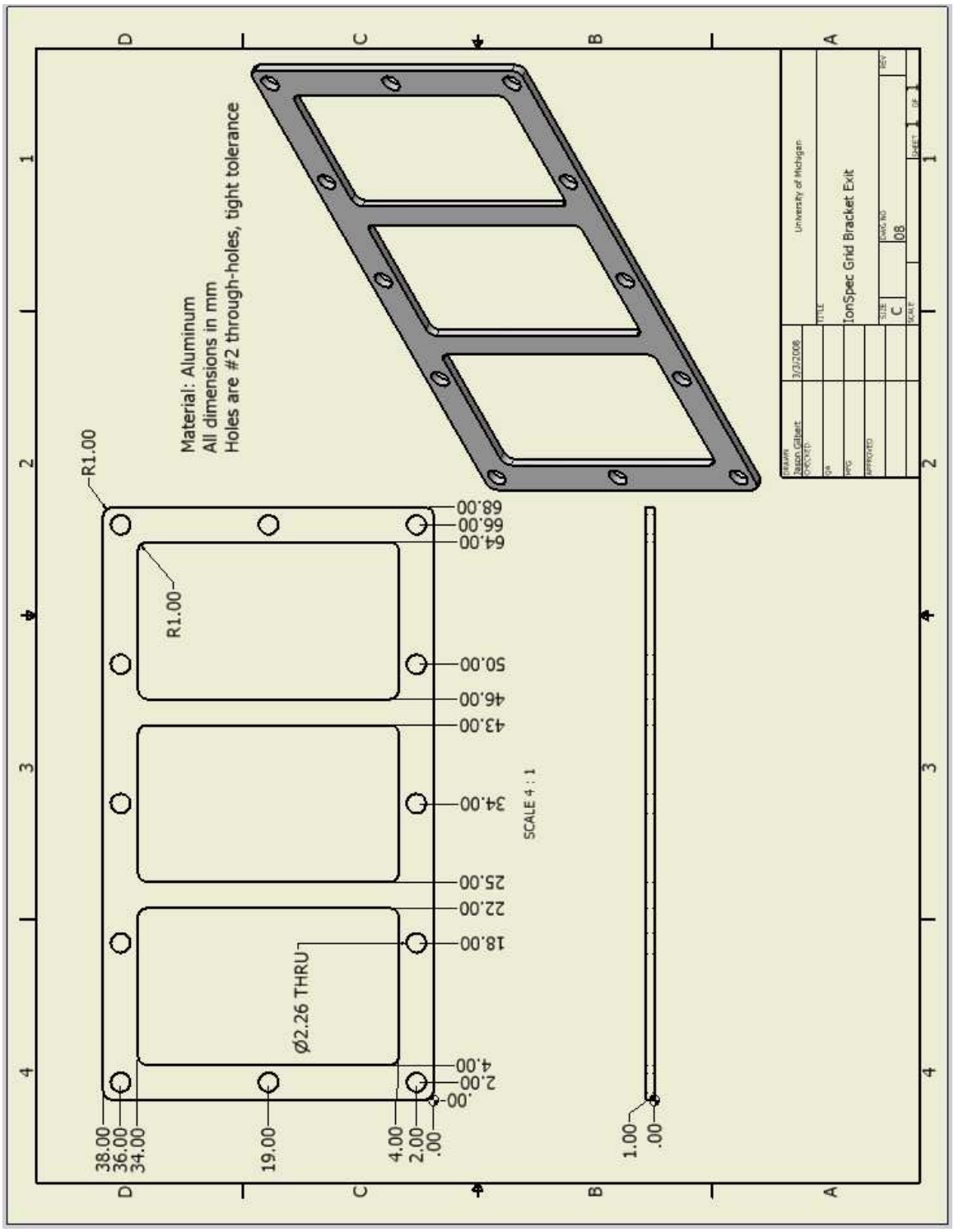

Figure B.4: The IonSpec exit aperture field control grid.

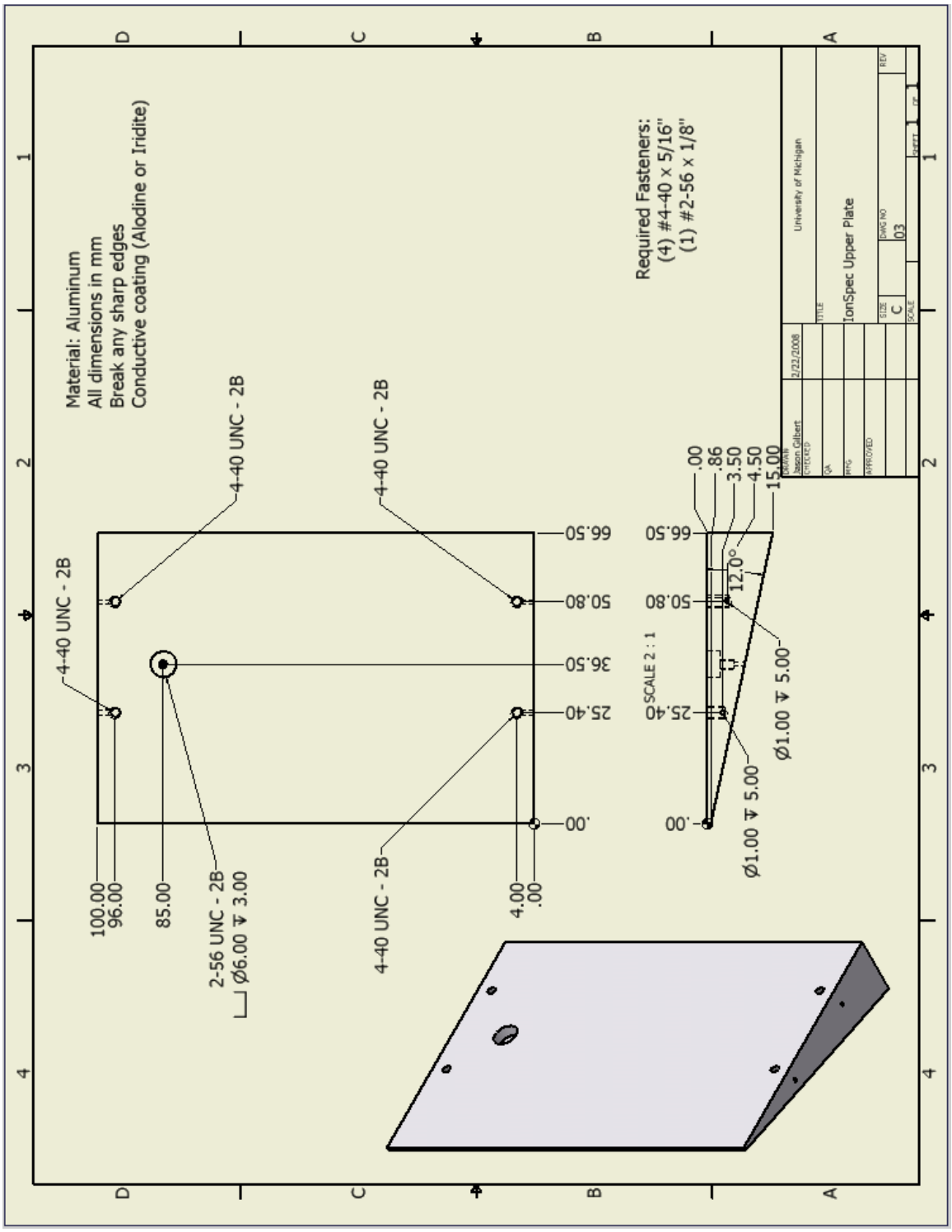

Figure B.5: The IonSpec upper electrostatic deflection plate.

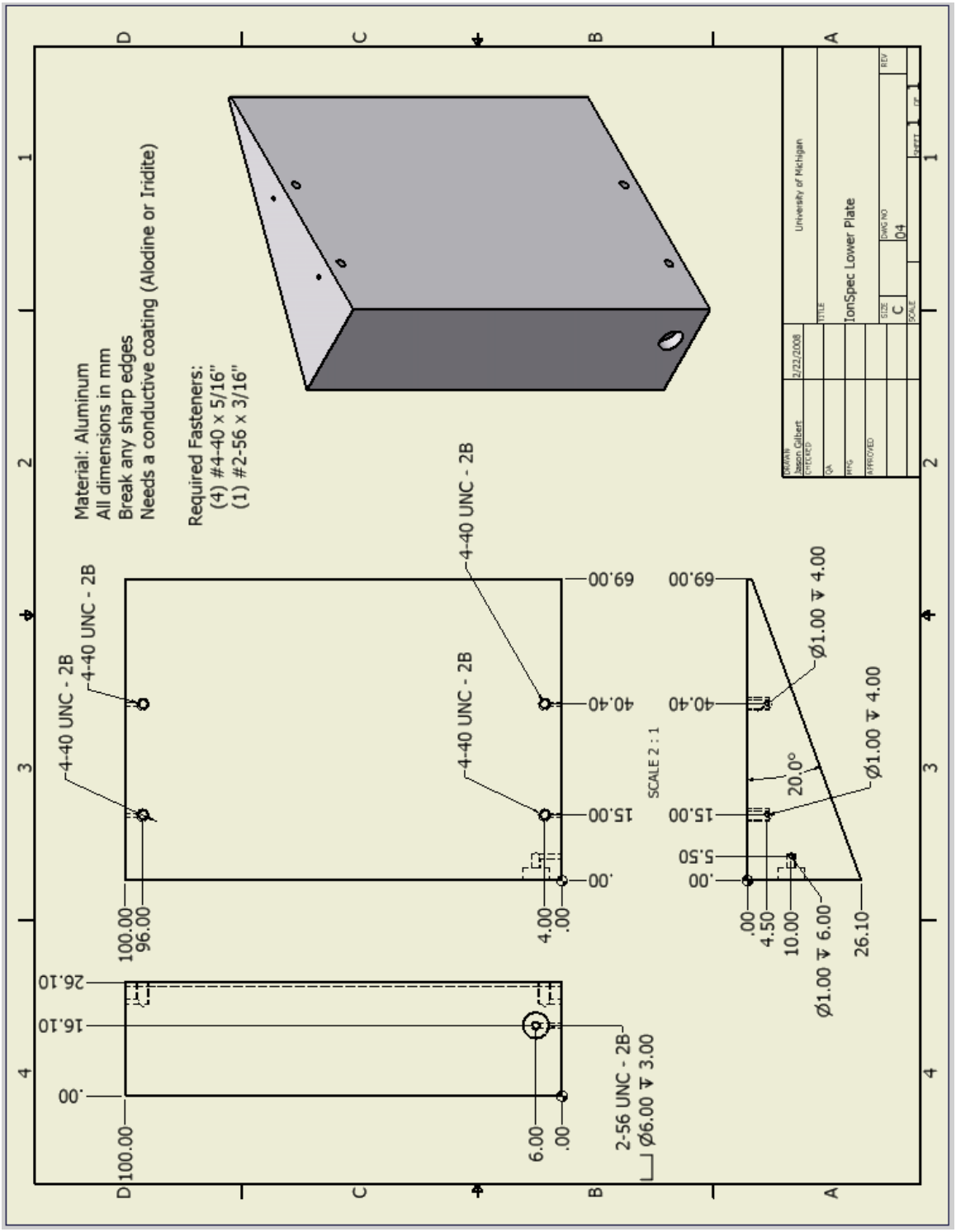

Figure B.6: The IonSpec lower electrostatic deflection plate.

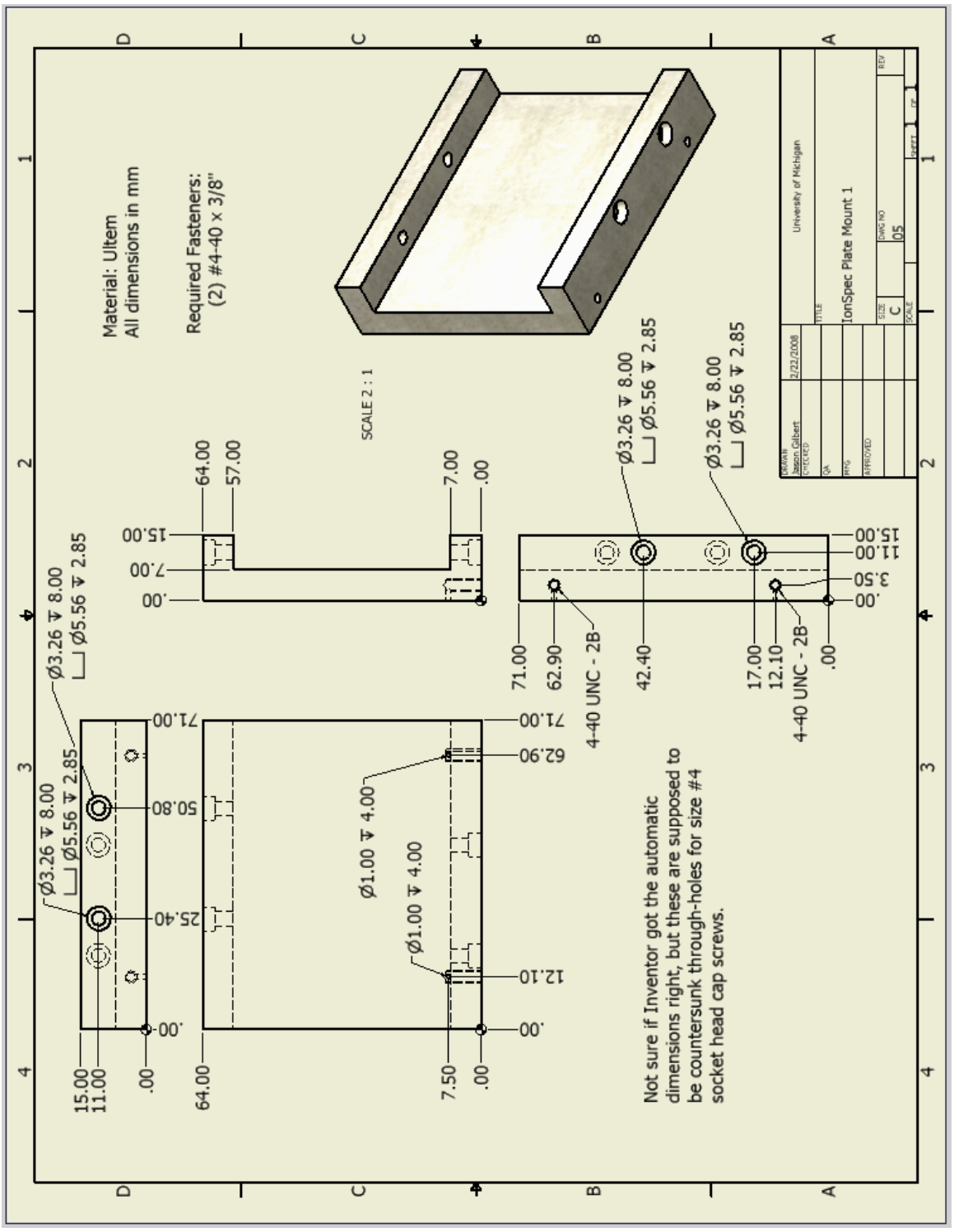

Figure B.7: The right-side mount for the IonSpec electrostatic deflection plates.

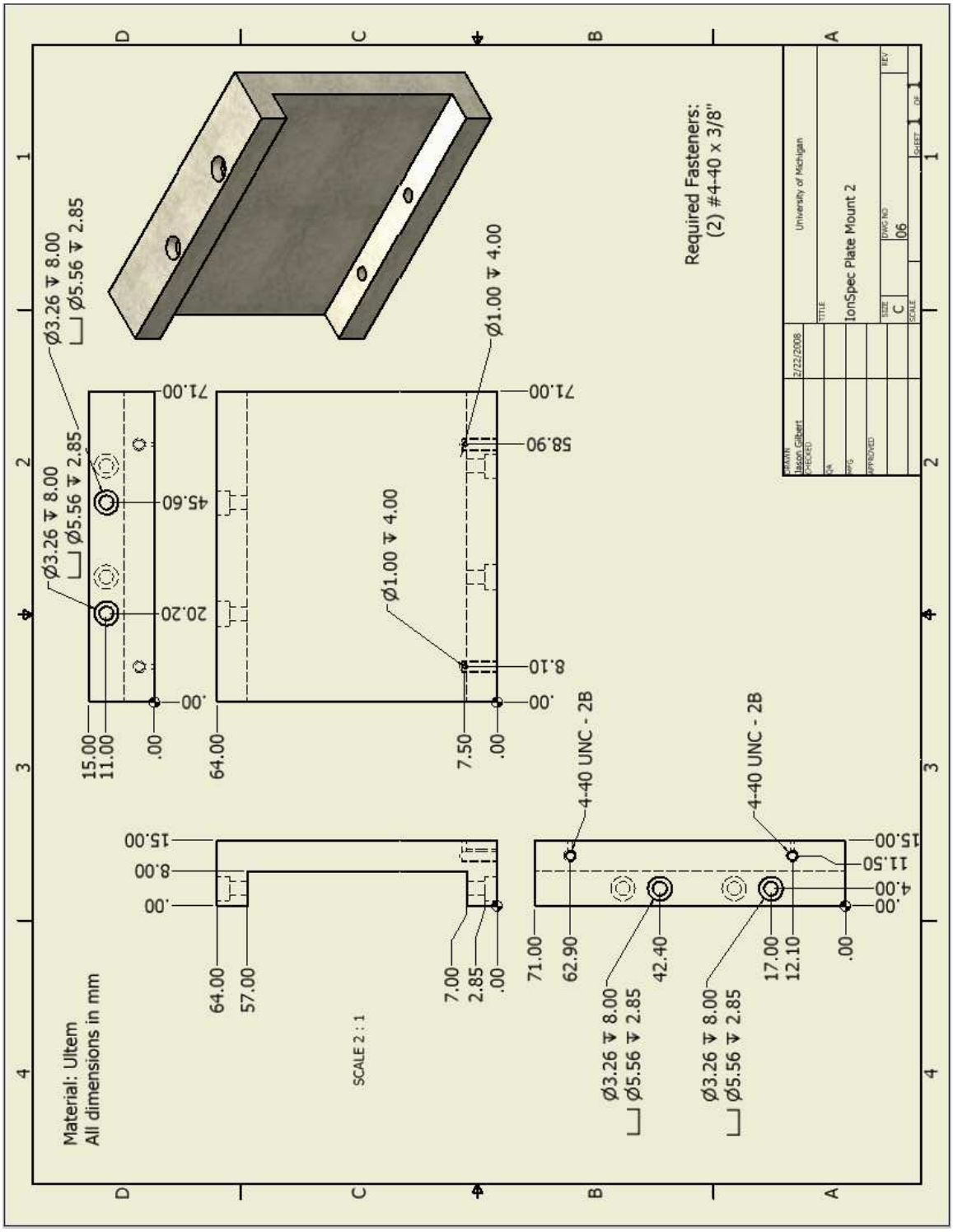

Figure B.8: The left-side mount for the IonSpec electrostatic deflection plates.

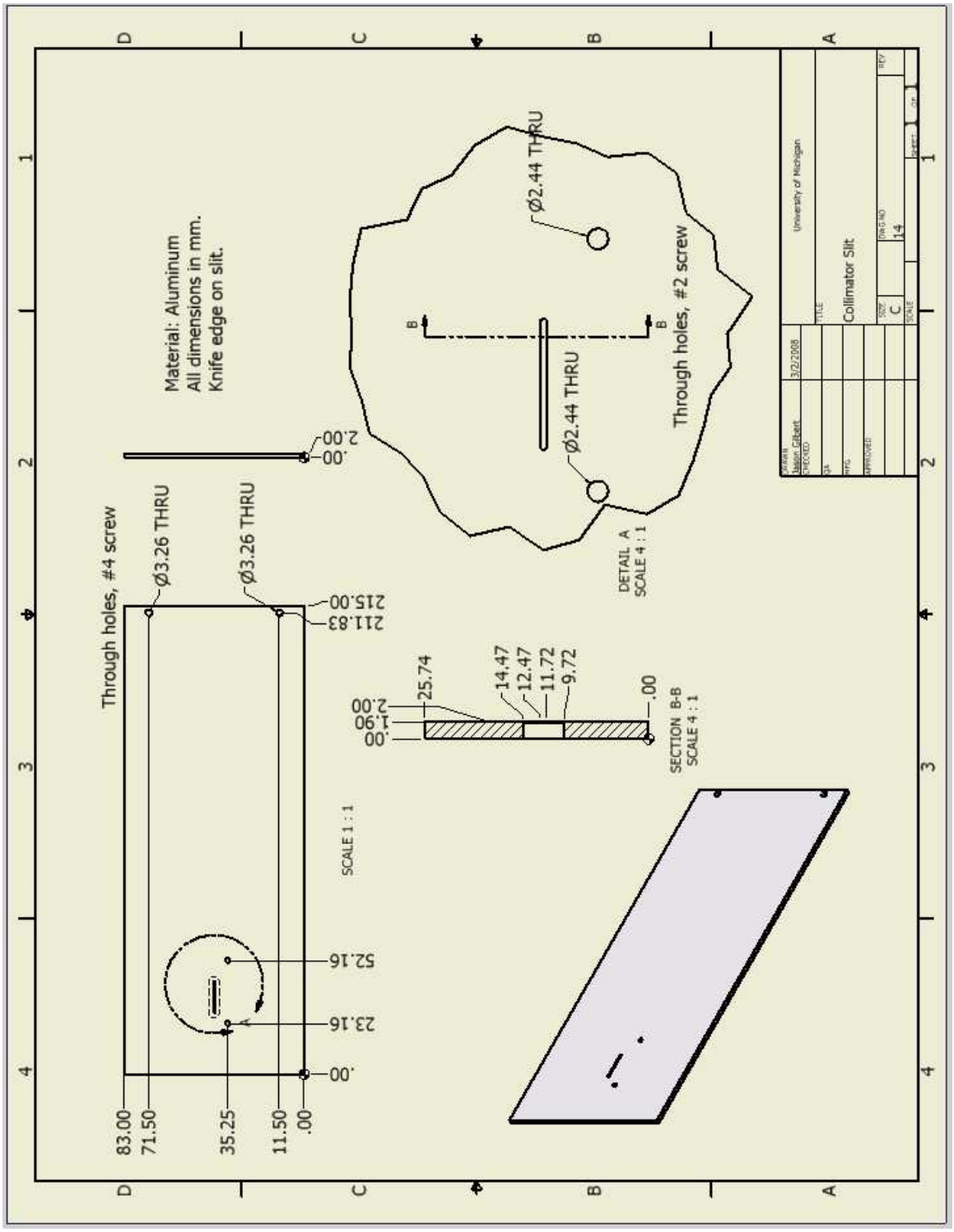

Figure B.9: The collimator slit used during IonSpec lab tests.

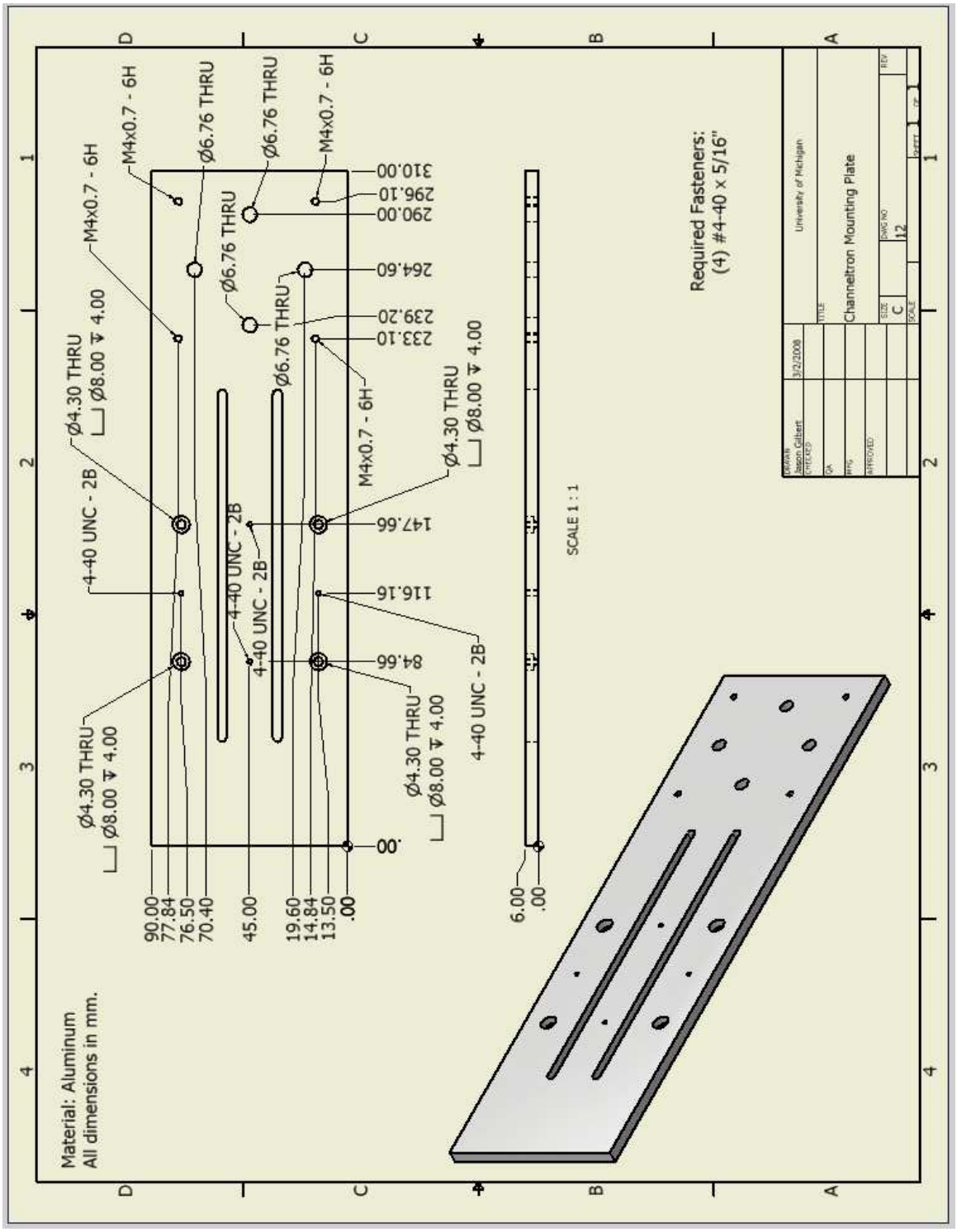

Figure B.10: The Channeltron Mounting Plate used in IonSpec lab tests.

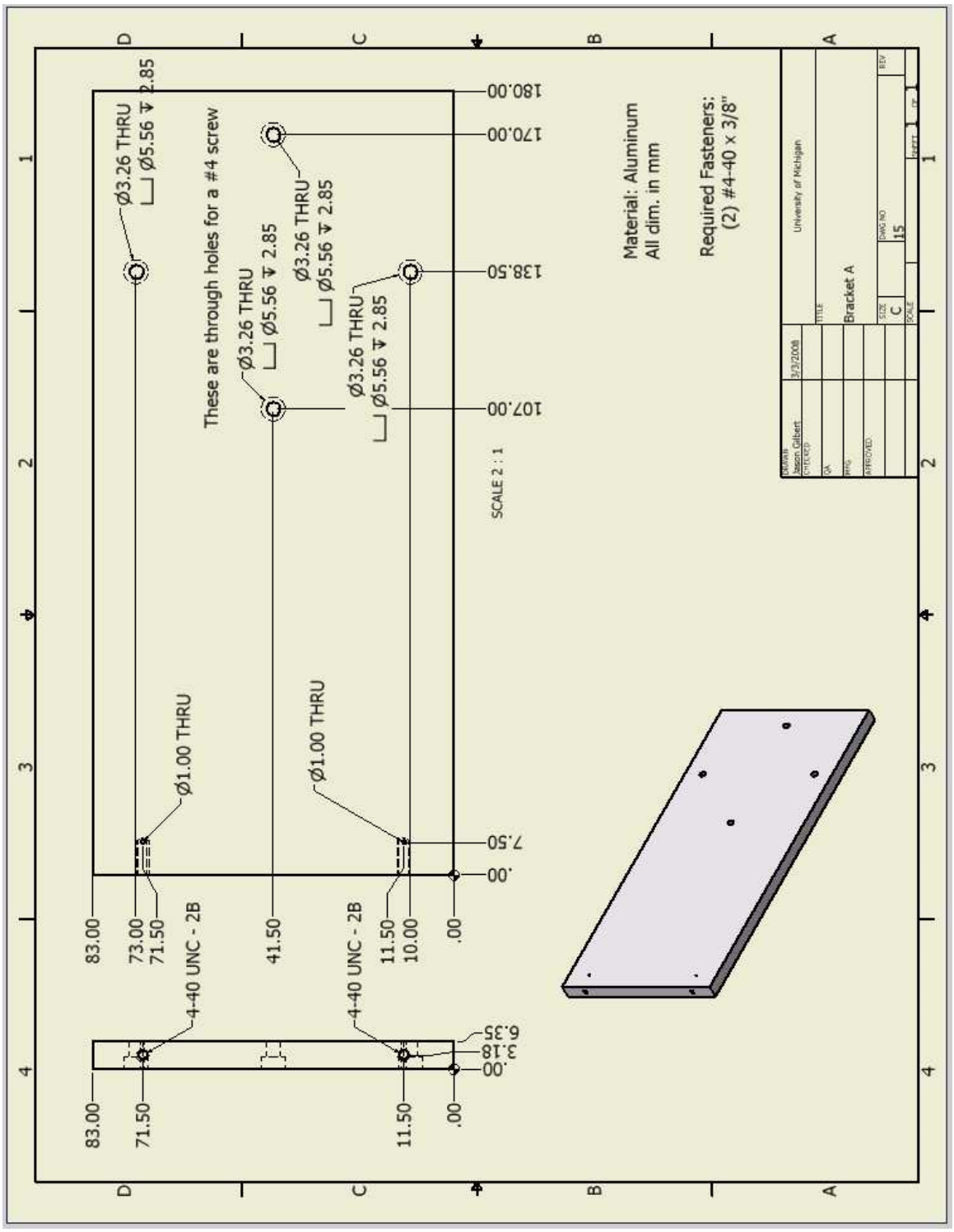

Figure B.11: A plate used to attach the collimator slit to the Channeltron Mounting Plate.

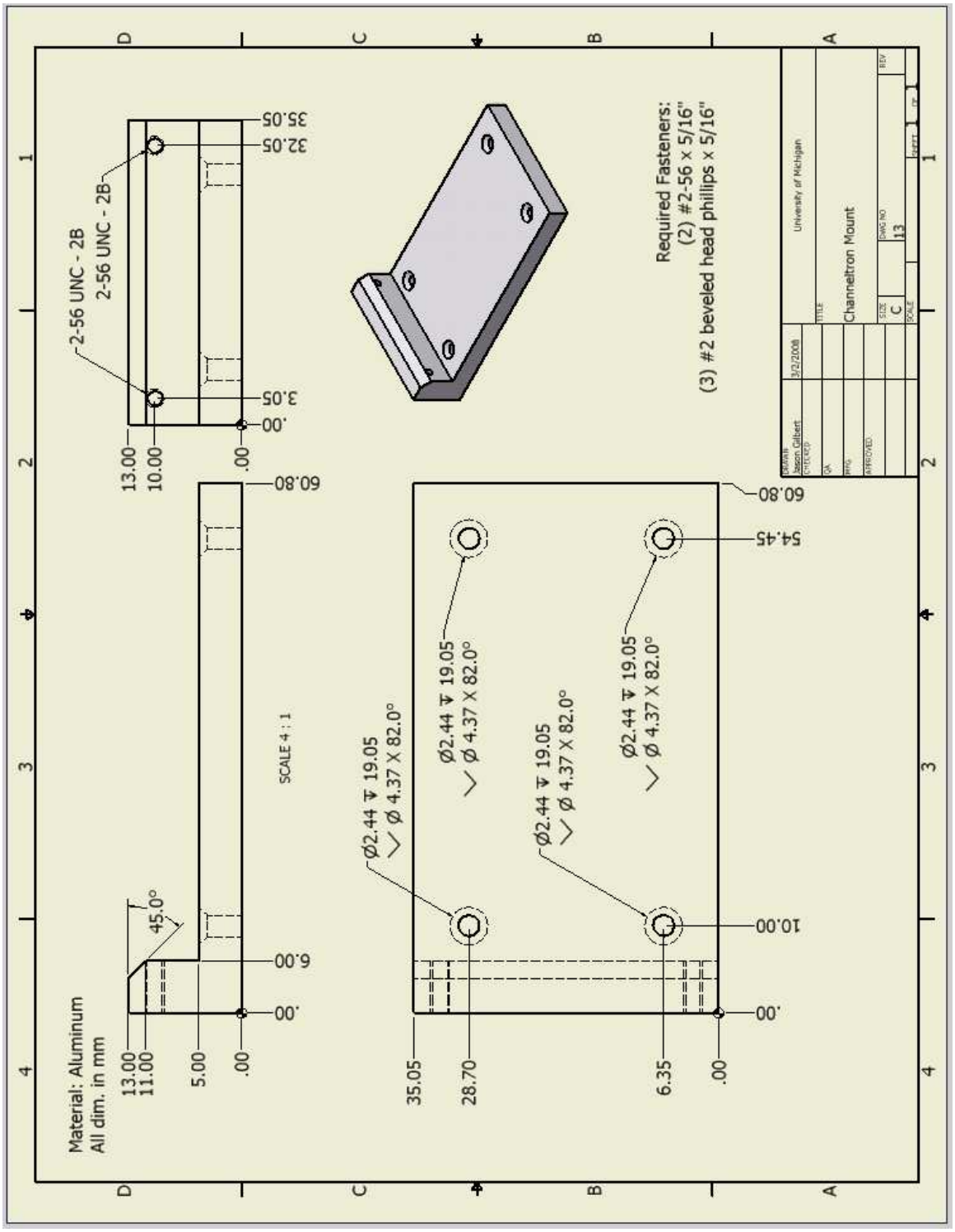

Figure B.12: A bracket used to mount the Channeltron to the collimator slit.

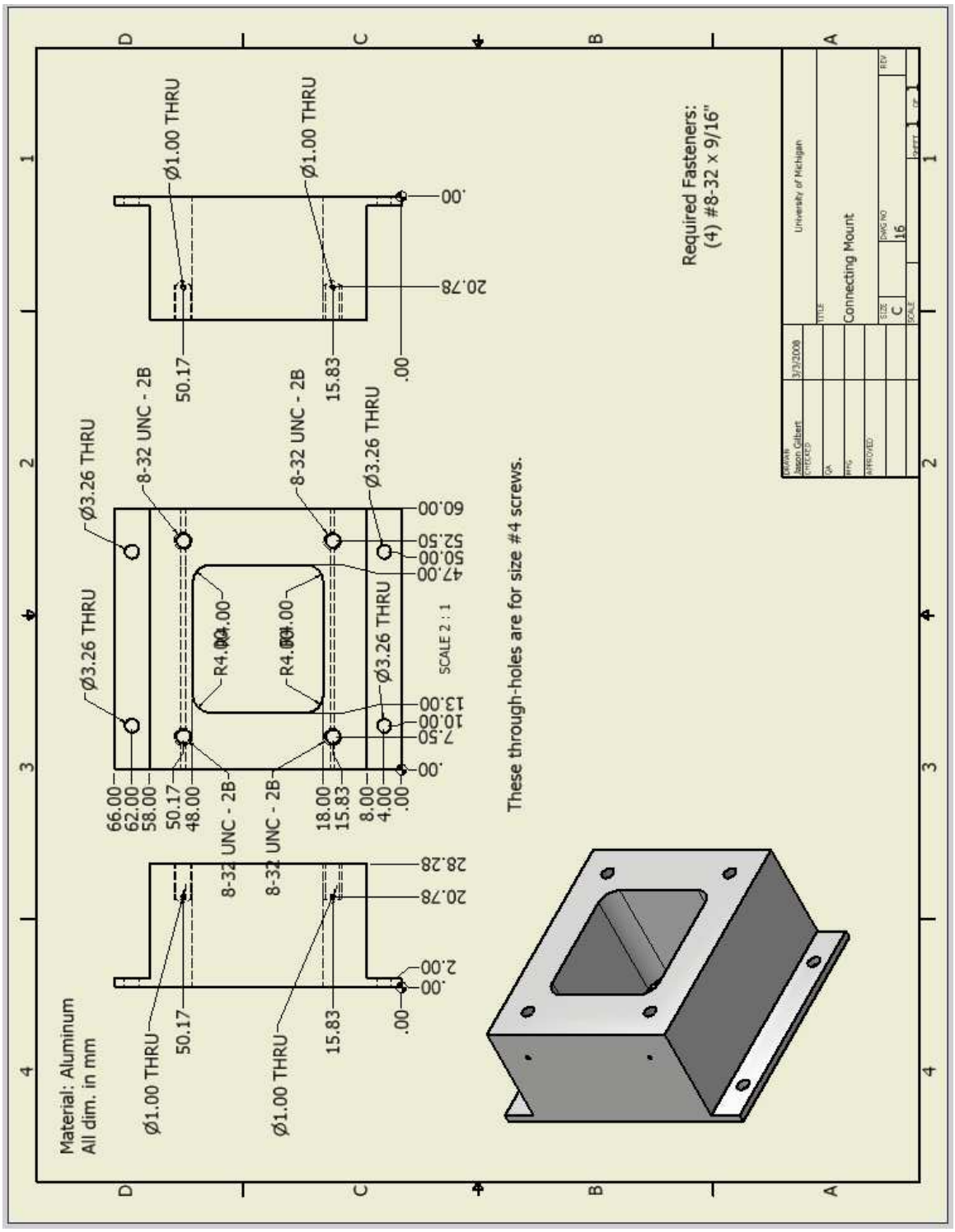

Figure B.13: A mounting bracket for attaching IonSpec to the lab test setup.

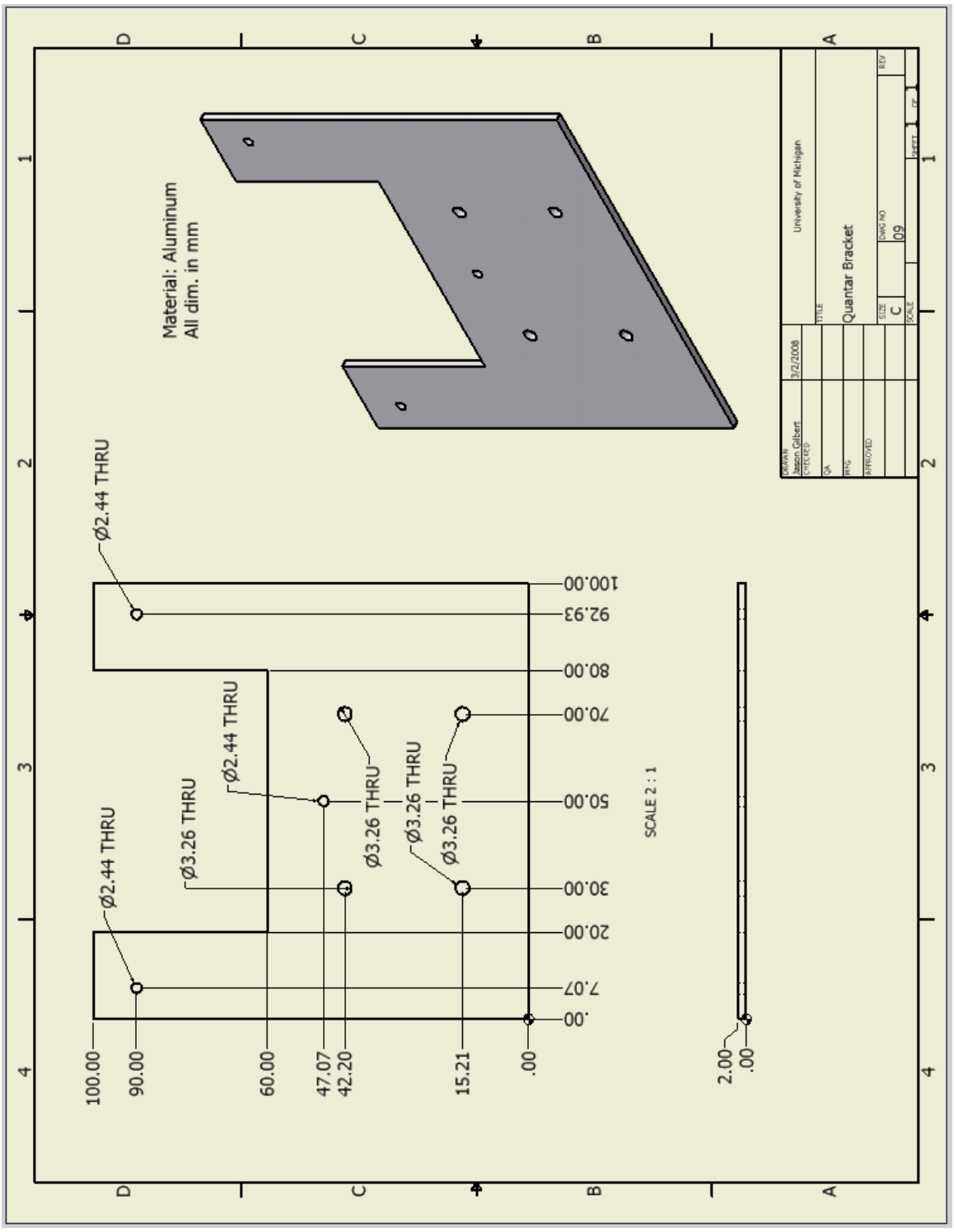

Figure B.14: A bracket used to hold the Quantar imaging detector.

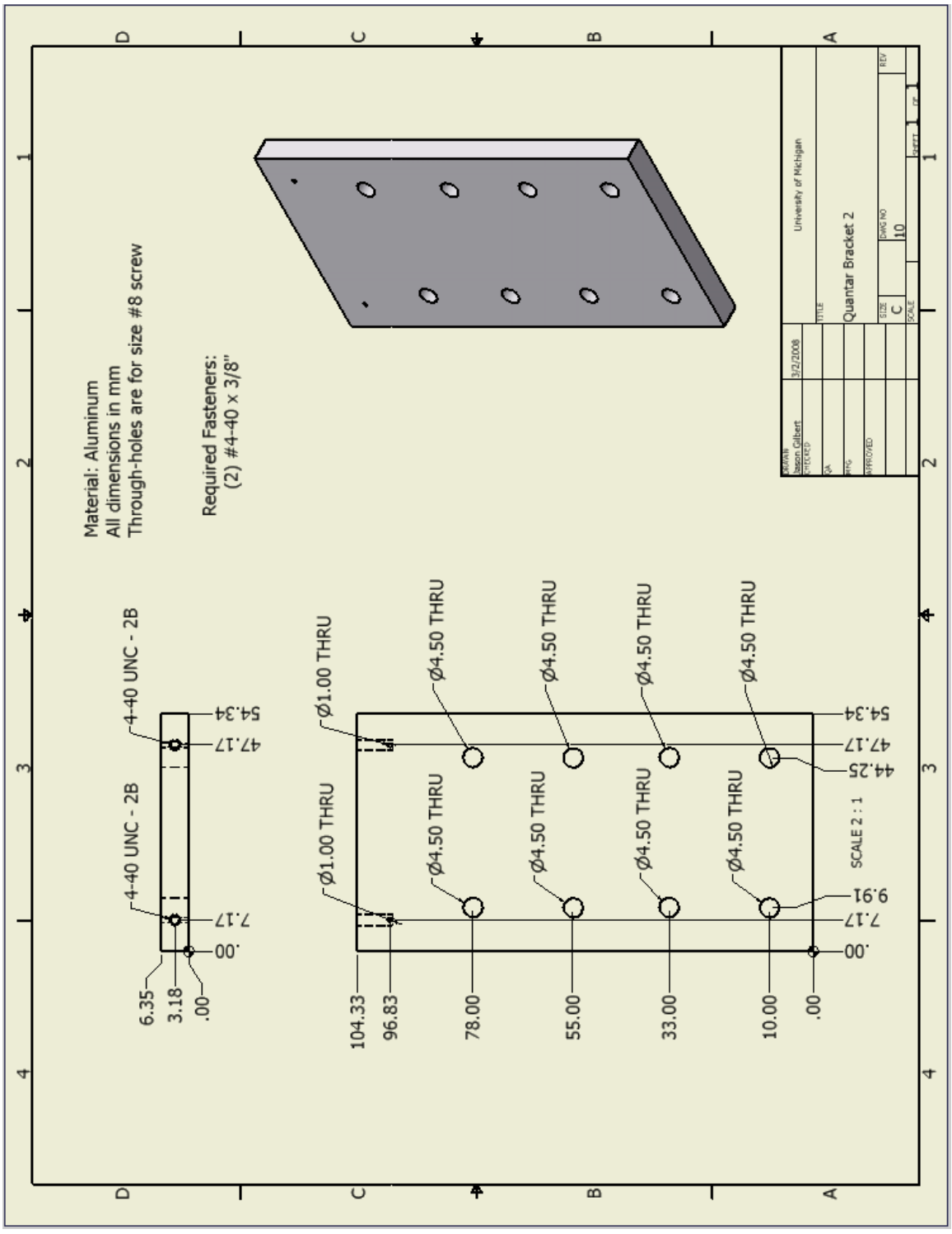

Figure B.15: A plate used to connect the Quantar bracket to the rotational stage.

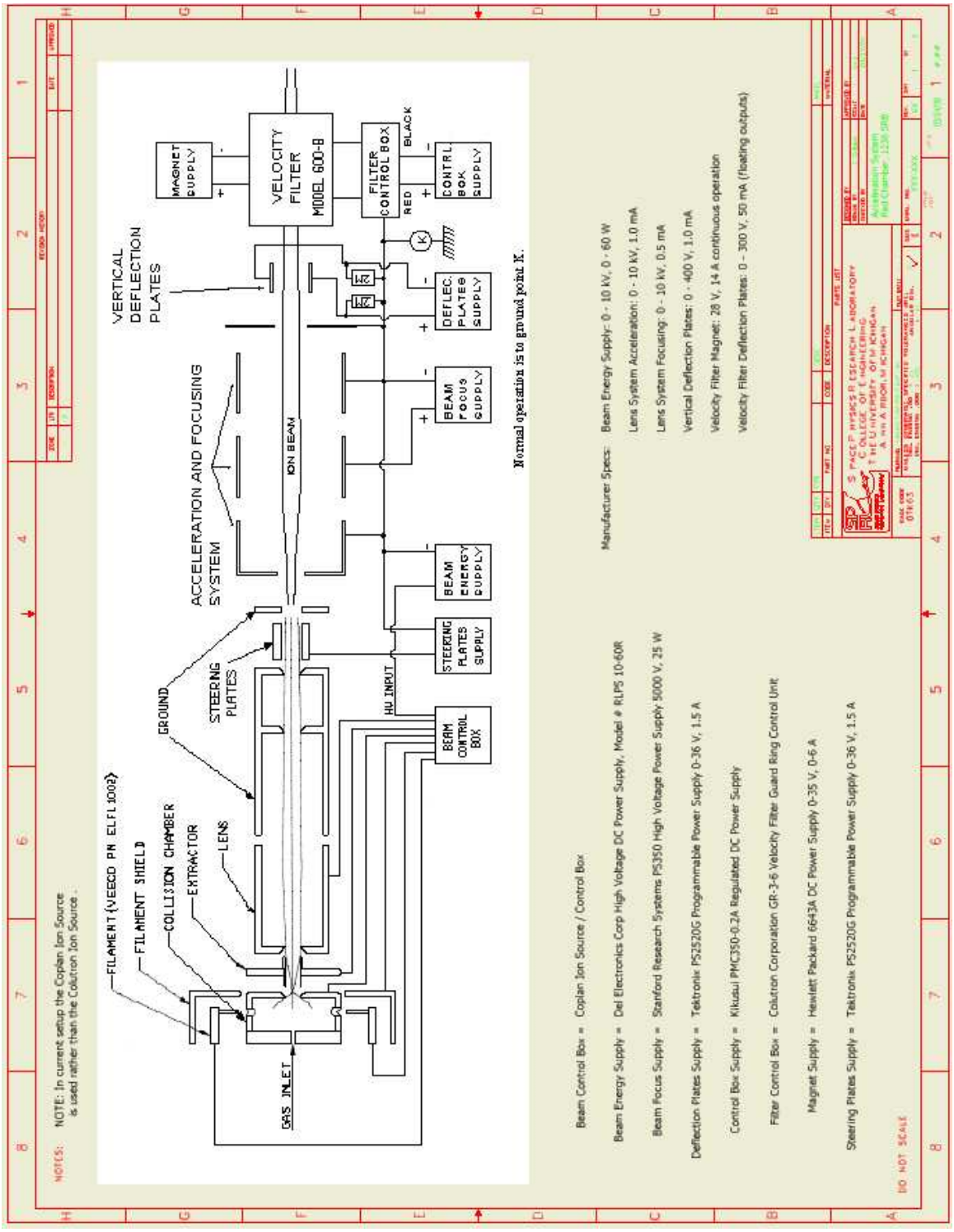

Figure B.16: A block diagram of the particle acceleration system used for all lab tests.

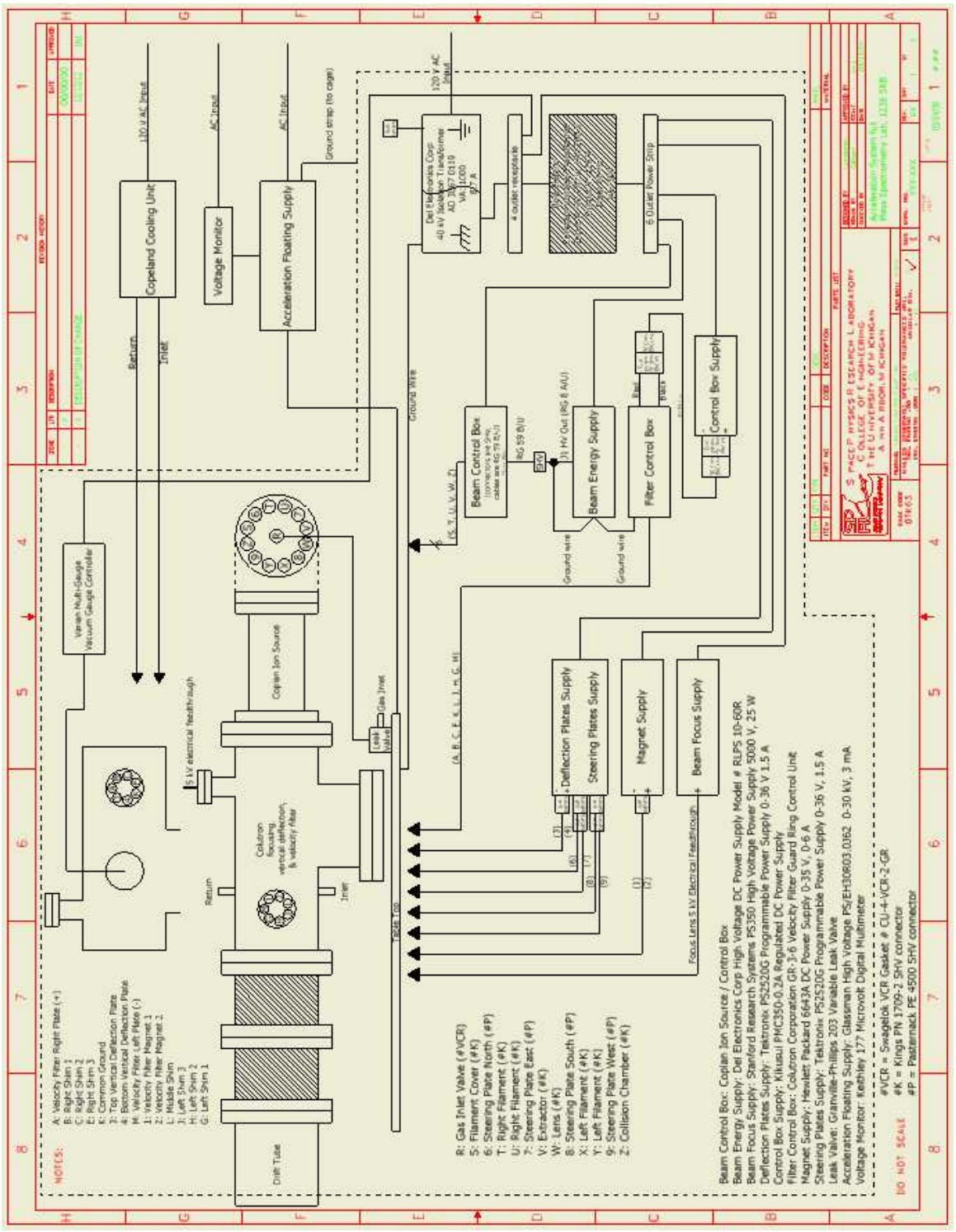

Figure B.17: A block diagram showing the connections and power supplies for the lab test system.

APPENDIX C

IonSpec Deflection Test Logs

The IonSpec measurements were performed over the course of 3 separate days. After the first day of tests, the collimator slit was widened to allow the instrument to be moved to the side for a test of fringe fields. The third day consisted of a larger, more detailed set of measurements than the other two so that the integrated energy-angle response could be calculated. The goal of these tests was to sweep through the entire E/q and angular range of the instrument. The columns for Vertical, Horizontal, and Angle indicate the settings on the motion control stages used in the test setup. The Upper and Lower voltages refer to the electrostatic deflection plates.

IonSpec Laboratory Tests, 20 May 2008								
Time	Count Rate	Vertical	Horizontal	Angle	Upper Voltage	Lower Voltage	Filename	Scaled Energy
12:30 PM	~10	27	0	20	-400	33.3	20080520-2.mpa	30
12:41 PM	~5	27	0	22	-400	33.3	20080520-3.mpa	30
12:57 PM	~5	27	0	24	-400	33.3	20080520-4.mpa	30
3:50 PM	~10	27	0	26	-400	33.3	20080520-5.mpa	30
4:00 PM	~10	27	0	28	-400	33.3	20080520-6.mpa	30
4:10 PM	0	27	0	30	-400	33.3	20080520-7.mpa	30
4:26 PM	~2	27	0	20	-300	25.0	20080520-8.mpa	40
5:01 PM	~5	27	0	22	-300	25.0	20080520-9.mpa	40
5:19 PM	~4	27	0	24	-300	25.0	20080520-10.mpa	40
5:35 PM	~8	27	0	26	-300	25.0	20080520-11.mpa	40
5:46 PM	~8	27	0	28	-300	25.0	20080520-12.mpa	40
5:56 PM	~5	27	0	29	-300	25.0	20080520-13.mpa	40
6:08 PM	~5	27	0	19.5	-240	20.0	20080520-14.mpa	50
6:23 PM	~17	27	0	21.5	-240	20.0	20080520-15.mpa	50
6:31 PM	~19	27	0	23.5	-240	20.0	20080520-16.mpa	50
6:38 PM	~20	27	0	25.5	-240	20.0	20080520-17.mpa	50
6:45 PM	~20	27	0	27.5	-240	20.0	20080520-18.mpa	50
6:50 PM	~15	27	0	29	-240	20.0	20080520-19.mpa	50
6:56 PM	~12	27	0	19.5	-200	16.7	20080520-20.mpa	60
7:03 PM	~50	27	0	21.5	-200	16.7	20080520-21.mpa	60
7:06 PM	~40	27	0	23.5	-200	16.7	20080520-22.mpa	60
7:08 PM	~40	27	0	25.5	-200	16.7	20080520-23.mpa	60
7:11 PM	~40	27	0	27.5	-200	16.7	20080520-24.mpa	60
7:18 PM	~25	27	0	29	-200	16.7	20080520-25.mpa	60
7:23 PM	~25	27	0	19.5	-171.4	14.3	20080520-26.mpa	70
7:26 PM	~90	27	0	21.5	-171.4	14.3	20080520-27.mpa	70
7:28 PM	~85	27	0	23.5	-171.4	14.3	20080520-28.mpa	70
7:29 PM	~80	27	0	25.5	-171.4	14.3	20080520-29.mpa	70
7:31 PM	~70	27	0	27.5	-171.4	14.3	20080520-30.mpa	70
7:33 PM	~70	27	0	29	-171.4	14.3	20080520-31.mpa	70
7:36 PM	~6	27	0	19.5	-150	12.5	20080520-32.mpa	80
7:44 PM	~20	27	0	21.5	-150	12.5	20080520-33.mpa	80
7:48 PM	~80	27	0	23.5	-150	12.5	20080520-34.mpa	80
7:49 PM	~100	27	0	25.5	-150	12.5	20080520-35.mpa	80
7:51 PM	~90	27	0	27.5	-150	12.5	20080520-36.mpa	80
7:53 PM	~25	27	0	29	-150	12.5	20080520-37.mpa	80
8:25 PM	0	27	0	19.5	-141.2	11.8	20080520-38.mpa	85
8:27 PM	0	27	0	21.5	-141.2	11.8	20080520-39.mpa	85
8:30 PM	~1	27	0	23.5	-141.2	11.8	20080520-40.mpa	85
8:50 PM	~8	27	0	25.5	-141.2	11.8	20080520-41.mpa	85
9:03 PM	~3	27	0	27.5	-141.2	11.8	20080520-42.mpa	85
9:27 PM	0	27	0	29	-141.2	11.8	20080520-43.mpa	85
9:38 PM	0	27	0	19.5	-142.9	11.9	20080520-44.mpa	84
9:41 PM	0	27	0	21.5	-142.9	11.9	20080520-45.mpa	84
9:44 PM	~4	27	0	23.5	-142.9	11.9	20080520-46.mpa	84
9:58 PM	~12	27	0	25.5	-142.9	11.9	20080520-47.mpa	84
10:08 PM	~7	27	0	27.5	-142.9	11.9	20080520-48.mpa	84
10:23 PM	0	27	0	29	-142.9	11.9	20080520-49.mpa	84
10:26 PM	~80	27	0	19.5	-428.6	35.7	20080520-50.mpa	28
10:31 PM	~170	27	0	21.5	-428.6	35.7	20080520-51.mpa	28
10:32 PM	~150	27	0	23.5	-428.6	35.7	20080520-52.mpa	28
10:35 PM	~130	27	0	25.5	-428.6	35.7	20080520-53.mpa	28
10:36 PM	~90	27	0	27.5	-428.6	35.7	20080520-54.mpa	28
10:38 PM	~30	27	0	29	-428.6	35.7	20080520-55.mpa	28

Figure C.1: IonSpec test log for 20 May 2008.

IonSpec Laboratory Tests, 30 May 2008 - Instrument moved to side								
Time	Count Rate	Vertical	Horizontal	Angle	Upper Voltage	Lower Voltage	Filename	Scaled Energy
11:01 AM	0	27	1	19.5	-480.00	40.00	20080530-1.mpa	25
11:04 AM	1.5	27	1	21.5	-480.00	40.00	20080530-2.mpa	25
11:10 AM	1.5	27	1	23.5	-480.00	40.00	20080530-3.mpa	25
11:15 AM	4	27	1	25.5	-480.00	40.00	20080530-4.mpa	25
11:21 AM	0	27	1	27.5	-480.00	40.00	20080530-5.mpa	25
11:27 AM	0	27	1	29.5	-480.00	40.00	20080530-6.mpa	25
11:32 AM	0	27	1	19.5	-342.86	28.57	20080530-7.mpa	35
11:36 AM	6.5	27	1	21.5	-342.86	28.57	20080530-8.mpa	35
11:48 AM	5	27	1	23.5	-342.86	28.57	20080530-9.mpa	35
11:59 AM	8	27	1	25.5	-342.86	28.57	20080530-10.mpa	35
12:07 PM	12	27	1	27.5	-342.86	28.57	20080530-11.mpa	35
12:12 PM	1	27	1	29.5	-342.86	28.57	20080530-12.mpa	35
12:21 PM	0	27	1	19.5	-266.67	22.22	20080530-13.mpa	45
12:26 PM	20	27	1	21.5	-266.67	22.22	20080530-14.mpa	45
12:31 PM	30	27	1	23.5	-266.67	22.22	20080530-15.mpa	45
12:36 PM	40	27	1	25.5	-266.67	22.22	20080530-16.mpa	45
12:42 PM	45	27	1	27.5	-266.67	22.22	20080530-17.mpa	45
12:44 PM	5	27	1	29.5	-266.67	22.22	20080530-18.mpa	45
12:52 PM	0	27	1	19.5	-218.18	18.18	20080530-19.mpa	55
12:57 PM	60	27	1	21.5	-218.18	18.18	20080530-20.mpa	55
1:02 PM	60	27	1	23.5	-218.18	18.18	20080530-21.mpa	55
1:03 PM	55	27	1	25.5	-218.18	18.18	20080530-22.mpa	55
1:07 PM	45	27	1	27.5	-218.18	18.18	20080530-23.mpa	55
1:10 PM	8	27	1	29.5	-218.18	18.18	20080530-24.mpa	55
1:16 PM	0	27	1	19.5	-184.62	15.38	20080530-25.mpa	65
1:21 PM	50	27	1	21.5	-184.62	15.38	20080530-26.mpa	65
1:26 PM	50	27	1	23.5	-184.62	15.38	20080530-27.mpa	65
1:29 PM	40	27	1	25.5	-184.62	15.38	20080530-28.mpa	65
1:30 PM	40	27	1	27.5	-184.62	15.38	20080530-29.mpa	65
1:32 PM	5	27	1	29.5	-184.62	15.38	20080530-30.mpa	65
1:37 PM	0	27	1	19.5	-160.00	13.33	20080530-31.mpa	75
1:40 PM	0	27	1	21.5	-160.00	13.33	20080530-32.mpa	75
1:43 PM	2	27	1	23.5	-160.00	13.33	20080530-33.mpa	75
1:46 PM	0	27	1	25.5	-160.00	13.33	20080530-34.mpa	75
1:50 PM	0	27	1	27.5	-160.00	13.33	20080530-35.mpa	75
1:55 PM	0	27	1	29.5	-160.00	13.33	20080530-36.mpa	75
2:00 PM	0	27	1	19.5	-141.18	11.76	20050530-37.mpa	85
2:04 PM	0	27	1	21.5	-141.18	11.76	20050530-38.mpa	85
2:09 PM	0	27	1	23.5	-141.18	11.76	20050530-39.mpa	85
2:14 PM	0.5	27	1	25.5	-141.18	11.76	20050530-40.mpa	85
2:21 PM	3	27	1	27.5	-141.18	11.76	20050530-41.mpa	85
2:24 PM	0.5	27	1	29.5	-141.18	11.76	20050530-42.mpa	85

Figure C.2: IonSpec test log for 30 May 2008.

IonSpec Laboratory Tests, 5 June 2008								
Time	Count Rate	Vertical	Horizontal	Angle	Upper Voltage	Lower Voltage	Scaled Energy	Filename
2:24 PM	45	25	0	19	-141.176	11.8	85	20080605 - 1 .mpa
2:26 PM	170	25	0	20	-141.176	11.8	85	20080605 - 2 .mpa
2:28 PM	175	25	0	21	-141.176	11.8	85	20080605 - 3 .mpa
2:31 PM	180	25	0	22	-141.176	11.8	85	20080605 - 4 .mpa
2:33 PM	180	25	0	23	-141.176	11.8	85	20080605 - 5 .mpa
2:37 PM	220	25	0	24	-141.176	11.8	85	20080605 - 6 .mpa
2:40 PM	450	25	0	25	-141.176	11.8	85	20080605 - 7 .mpa
2:42 PM	780	25	0	26	-141.176	11.8	85	20080605 - 8 .mpa
2:45 PM	950	25	0	27	-141.176	11.8	85	20080605 - 9 .mpa
2:47 PM	900	25	0	28	-141.176	11.8	85	20080605 - 10 .mpa
2:50 PM	750	25	0	29	-141.176	11.8	85	20080605 - 11 .mpa
copy of -1		25	0	30	-141.176	11.8	85	20080605 - 12 .mpa
2:54 PM	35	25	0	19	-150	12.5	80	20080605 - 13 .mpa
2:56 PM	190	25	0	20	-150	12.5	80	20080605 - 14 .mpa
2:58 PM	230	25	0	21	-150	12.5	80	20080605 - 15 .mpa
3:03 PM	400	25	0	22	-150	12.5	80	20080605 - 16 .mpa
3:06 PM	740	25	0	23	-150	12.5	80	20080605 - 17 .mpa
3:09 PM	1000	25	0	24	-150	12.5	80	20080605 - 18 .mpa
3:12 PM	1100	25	0	25	-150	12.5	80	20080605 - 19 .mpa
3:15 PM	1200	25	0	26	-150	12.5	80	20080605 - 20 .mpa
3:21 PM	1000	25	0	27	-150	12.5	80	20080605 - 21 .mpa
3:25 PM	900	25	0	28	-150	12.5	80	20080605 - 22 .mpa
3:28 PM	500	25	0	29	-150	12.5	80	20080605 - 23 .mpa
copy of -13		25	0	30	-150	12.5	80	20080605 - 24 .mpa
3:33 PM	35	25	0	19	-160	13.3	75	20080605 - 25 .mpa
3:34 PM	1500	25	0	20	-160	13.3	75	20080605 - 26 .mpa
3:37 PM	1550	25	0	21	-160	13.3	75	20080605 - 27 .mpa
3:40 PM	1650	25	0	22	-160	13.3	75	20080605 - 28 .mpa
3:44 PM	1700	25	0	23	-160	13.3	75	20080605 - 29 .mpa
3:48 PM	1675	25	0	24	-160	13.3	75	20080605 - 30 .mpa
3:52 PM	1750	25	0	25	-160	13.3	75	20080605 - 31 .mpa
3:55 PM	1650	25	0	26	-160	13.3	75	20080605 - 32 .mpa
3:59 PM	1650	25	0	27	-160	13.3	75	20080605 - 33 .mpa
4:02 PM	1650	25	0	28	-160	13.3	75	20080605 - 34 .mpa
4:06 PM	1500	25	0	29	-160	13.3	75	20080605 - 35 .mpa
copy of -25		25	0	30	-160	13.3	75	20080605 - 36 .mpa
4:09 PM	35	25	0	19	-171.429	14.3	70	20080605 - 37 .mpa
4:11 PM	1850	25	0	20	-171.429	14.3	70	20080605 - 38 .mpa
4:14 PM	1850	25	0	21	-171.429	14.3	70	20080605 - 39 .mpa
4:19 PM	1700	25	0	22	-171.429	14.3	70	20080605 - 40 .mpa
4:23 PM	1800	25	0	23	-171.429	14.3	70	20080605 - 41 .mpa
4:26 PM	1850	25	0	24	-171.429	14.3	70	20080605 - 42 .mpa
4:30 PM	1900	25	0	25	-171.429	14.3	70	20080605 - 43 .mpa
4:35 PM	1900	25	0	26	-171.429	14.3	70	20080605 - 44 .mpa
4:38 PM	1800	25	0	27	-171.429	14.3	70	20080605 - 45 .mpa
4:41 PM	1800	25	0	28	-171.429	14.3	70	20080605 - 46 .mpa
4:44 PM	1650	25	0	29	-171.429	14.3	70	20080605 - 47 .mpa
4:47 PM	35	25	0	30	-171.429	14.3	70	20080605 - 48 .mpa

Figure C.3: IonSpec test log for 5 June 2008. Continues on next 3 pages.

4:52 PM	35	25	0	19	-184.615	15.4	65	20080605 - 49 .mpa
4:54 PM	1800	25	0	20	-184.615	15.4	65	20080605 - 50 .mpa
4:57 PM	1800	25	0	21	-184.615	15.4	65	20080605 - 51 .mpa
5:00 PM	1900	25	0	22	-184.615	15.4	65	20080605 - 52 .mpa
5:04 PM	1900	25	0	23	-184.615	15.4	65	20080605 - 53 .mpa
5:07 PM	1900	25	0	24	-184.615	15.4	65	20080605 - 54 .mpa
5:12 PM	1850	25	0	25	-184.615	15.4	65	20080605 - 55 .mpa
5:15 PM	1850	25	0	26	-184.615	15.4	65	20080605 - 56 .mpa
5:19 PM	1950	25	0	27	-184.615	15.4	65	20080605 - 57 .mpa
5:22 PM	1800	25	0	28	-184.615	15.4	65	20080605 - 58 .mpa
5:25 PM	1800	25	0	29	-184.615	15.4	65	20080605 - 59 .mpa
5:28 PM	35	25	0	30	-184.615	15.4	65	20080605 - 60 .mpa
5:30 PM	35	25	0	19	-200	16.7	60	20080605 - 61 .mpa
5:30 PM	2000	25	0	20	-200	16.7	60	20080605 - 62 .mpa
5:34 PM	1900	25	0	21	-200	16.7	60	20080605 - 63 .mpa
5:38 PM	1950	25	0	22	-200	16.7	60	20080605 - 64 .mpa
5:41 PM	2100	25	0	23	-200	16.7	60	20080605 - 65 .mpa
5:43 PM	2200	25	0	24	-200	16.7	60	20080605 - 66 .mpa
5:45 PM	2100	25	0	25	-200	16.7	60	20080605 - 67 .mpa
5:47 PM	2100	25	0	26	-200	16.7	60	20080605 - 68 .mpa
5:50 PM	2000	25	0	27	-200	16.7	60	20080605 - 69 .mpa
5:53 PM	1900	25	0	28	-200	16.7	60	20080605 - 70 .mpa
5:56 PM	1700	25	0	29	-200	16.7	60	20080605 - 71 .mpa
5:59 PM	35	25	0	30	-200	16.7	60	20080605 - 72 .mpa
6:01 PM	35	25	0	19	-218.182	18.2	55	20080605 - 73 .mpa
6:03 PM	2100	25	0	20	-218.182	18.2	55	20080605 - 74 .mpa
6:05 PM	2000	25	0	21	-218.182	18.2	55	20080605 - 75 .mpa
6:07 PM	2100	25	0	22	-218.182	18.2	55	20080605 - 76 .mpa
6:10 PM	2100	25	0	23	-218.182	18.2	55	20080605 - 77 .mpa
6:12 PM	2200	25	0	24	-218.182	18.2	55	20080605 - 78 .mpa
6:15 PM	2300	25	0	25	-218.182	18.2	55	20080605 - 79 .mpa
6:20 PM	2100	25	0	26	-218.182	18.2	55	20080605 - 80 .mpa
6:22 PM	2000	25	0	27	-218.182	18.2	55	20080605 - 81 .mpa
6:25 PM	2000	25	0	28	-218.182	18.2	55	20080605 - 82 .mpa
6:28 PM	1800	25	0	29	-218.182	18.2	55	20080605 - 83 .mpa
6:31 PM	35	25	0	30	-218.182	18.2	55	20080605 - 84 .mpa
6:34 PM	35	25	0	19	-240	20.0	50	20080605 - 85 .mpa
6:36 PM	1800	25	0	20	-240	20.0	50	20080605 - 86 .mpa
6:38 PM	1850	25	0	21	-240	20.0	50	20080605 - 87 .mpa
6:42 PM	1950	25	0	22	-240	20.0	50	20080605 - 88 .mpa
6:44 PM	2000	25	0	23	-240	20.0	50	20080605 - 89 .mpa
6:47 PM	2000	25	0	24	-240	20.0	50	20080605 - 90 .mpa
6:49 PM	1950	25	0	25	-240	20.0	50	20080605 - 91 .mpa
6:51 PM	1850	25	0	26	-240	20.0	50	20080605 - 92 .mpa
6:53 PM	2000	25	0	27	-240	20.0	50	20080605 - 93 .mpa
6:55 PM	1800	25	0	28	-240	20.0	50	20080605 - 94 .mpa
6:58 PM	1800	25	0	29	-240	20.0	50	20080605 - 95 .mpa
7:00 PM	35	25	0	30	-240	20.0	50	20080605 - 96 .mpa

7:02 PM	40	25	0	19	-266.667	22.2	45	20080605 - 97 .mpa
7:04 PM	1450	25	0	20	-266.667	22.2	45	20080605 - 98 .mpa
7:07 PM	1650	25	0	21	-266.667	22.2	45	20080605 - 99 .mpa
7:10 PM	1800	25	0	22	-266.667	22.2	45	20080605 - 100 .mpa
7:12 PM	1700	25	0	23	-266.667	22.2	45	20080605 - 101 .mpa
7:15 PM	1800	25	0	24	-266.667	22.2	45	20080605 - 102 .mpa
7:18 PM	2300	25	0	25	-266.667	22.2	45	20080605 - 103 .mpa
7:20 PM	2100	25	0	26	-266.667	22.2	45	20080605 - 104 .mpa
7:22 PM	2100	25	0	27	-266.667	22.2	45	20080605 - 105 .mpa
7:25 PM	2000	25	0	28	-266.667	22.2	45	20080605 - 106 .mpa
7:28 PM	1900	25	0	29	-266.667	22.2	45	20080605 - 107 .mpa
7:30 PM	40	25	0	30	-266.667	22.2	45	20080605 - 108 .mpa
7:32 PM	40	25	0	19	-300	25.0	40	20080605 - 109 .mpa
7:33 PM	1000	25	0	20	-300	25.0	40	20080605 - 110 .mpa
7:37 PM	1100	25	0	21	-300	25.0	40	20080605 - 111 .mpa
7:40 PM	1200	25	0	22	-300	25.0	40	20080605 - 112 .mpa
7:43 PM	1500	25	0	23	-300	25.0	40	20080605 - 113 .mpa
7:47 PM	1550	25	0	24	-300	25.0	40	20080605 - 114 .mpa
7:50 PM	1600	25	0	25	-300	25.0	40	20080605 - 115 .mpa
7:53 PM	1800	25	0	26	-300	25.0	40	20080605 - 116 .mpa
7:56 PM	1800	25	0	27	-300	25.0	40	20080605 - 117 .mpa
7:58 PM	1850	25	0	28	-300	25.0	40	20080605 - 118 .mpa
8:01 PM	1880	25	0	29	-300	25.0	40	20080605 - 119 .mpa
8:03 PM	40	25	0	30	-300	25.0	40	20080605 - 120 .mpa
8:06 PM	40	25	0	19	-342.857	28.6	35	20080605 - 121 .mpa
8:07 PM	1600	25	0	20	-342.857	28.6	35	20080605 - 122 .mpa
8:10 PM	1300	25	0	21	-342.857	28.6	35	20080605 - 123 .mpa
8:13 PM	1300	25	0	22	-342.857	28.6	35	20080605 - 124 .mpa
8:17 PM	1100	25	0	23	-342.857	28.6	35	20080605 - 125 .mpa
8:21 PM	980	25	0	24	-342.857	28.6	35	20080605 - 126 .mpa
8:26 PM	950	25	0	25	-342.857	28.6	35	20080605 - 127 .mpa
8:31 PM	1000	25	0	26	-342.857	28.6	35	20080605 - 128 .mpa
8:36 PM	1100	25	0	27	-342.857	28.6	35	20080605 - 129 .mpa
8:40 PM	1400	25	0	28	-342.857	28.6	35	20080605 - 130 .mpa
8:43 PM	1600	25	0	29	-342.857	28.6	35	20080605 - 131 .mpa
8:46 PM	40	25	0	30	-342.857	28.6	35	20080605 - 132 .mpa
8:48 PM	40	25	0	19	-400	33.3	30	20080605 - 133 .mpa
8:49 PM	1800	25	0	20	-400	33.3	30	20080605 - 134 .mpa
8:51 PM	2100	25	0	21	-400	33.3	30	20080605 - 135 .mpa
8:53 PM	1800	25	0	22	-400	33.3	30	20080605 - 136 .mpa
8:55 PM	1900	25	0	23	-400	33.3	30	20080605 - 137 .mpa
8:58 PM	1900	25	0	24	-400	33.3	30	20080605 - 138 .mpa
9:00 PM	1850	25	0	25	-400	33.3	30	20080605 - 139 .mpa
9:03 PM	1800	25	0	26	-400	33.3	30	20080605 - 140 .mpa
9:05 PM	1700	25	0	27	-400	33.3	30	20080605 - 141 .mpa
9:08 PM	1400	25	0	28	-400	33.3	30	20080605 - 142 .mpa
9:12 PM	1100	25	0	29	-400	33.3	30	20080605 - 143 .mpa
9:15 PM	40	25	0	30	-400	33.3	30	20080605 - 144 .mpa

9:18 PM	40	25	0	19	-480	40.0	25	20080605 - 145 .mpa
9:19 PM	500	25	0	20	-480	40.0	25	20080605 - 146 .mpa
9:22 PM	350	25	0	21	-480	40.0	25	20080605 - 147 .mpa
9:24 PM	300	25	0	22	-480	40.0	25	20080605 - 148 .mpa
9:27 PM	300	25	0	23	-480	40.0	25	20080605 - 149 .mpa
9:30 PM	350	25	0	24	-480	40.0	25	20080605 - 150 .mpa
9:33 PM	500	25	0	25	-480	40.0	25	20080605 - 151 .mpa
9:36 PM	600	25	0	26	-480	40.0	25	20080605 - 152 .mpa
9:39 PM	450	25	0	27	-480	40.0	25	20080605 - 153 .mpa
9:41 PM	300	25	0	28	-480	40.0	25	20080605 - 154 .mpa
9:43 PM	750	25	0	29	-480	40.0	25	20080605 - 155 .mpa
9:47 PM	40	25	0	30	-480	40.0	25	20080605 - 156 .mpa

BIBLIOGRAPHY

BIBLIOGRAPHY

Allegrini, F., N. A. Schwadron, D. J. McComas, G. Gloeckler, and J. Geiss (2005), Stability of the inner source pickup ions over the solar cycle, *J. Geophys. Res.-Space*, *110*(A9), 5105–+, doi:10.1029/2004JA010847.

Altschuler, M. D., and G. Newkirk (1969), Magnetic Fields and the Structure of the Solar Corona. I: Methods of Calculating Coronal Fields, *Sol. Phys.*, *9*, 131–149, doi:10.1007/BF00145734.

Andrews, G. B., et al. (2007), The Energetic Particle and Plasma Spectrometer Instrument on the MESSENGER Spacecraft, *Space Sci. Rev.*, *131*, 523–556, doi:10.1007/s11214-007-9272-5.

Anglin, J. D., W. F. Dietrich, and J. A. Simpson (1973), Deuterium and Tritium from Solar Flares at ∼10 MeV Per Nucleon, *ApJ*, *186*, L41–L46.

Arge, C. N., and V. J. Pizzo (2000), Improvement in the prediction of solar wind conditions using near-real time solar magnetic field updates, *J. Geophys. Res.*, *105*, 10,465–10,480, doi:10.1029/1999JA900262.

Arge, C. N., J. G. Luhmann, D. Odstrcil, C. J. Schrijver, and Y. Li (2004), Stream structure and coronal sources of the solar wind during the May 12th, 1997 CME, *J. Atmos. Sol-Terr. Phy.*, *66*, 1295–1309, doi:10.1016/j.jastp.2004.03.018.

Axford, W. I. (1972), The Interaction of the Solar Wind With the Interstellar Medium, in *Solar Wind*, edited by C. P. Sonett, P. J. Coleman, and J. M. Wilcox, pp. 609–+.

Axford, W. I. (1973), Interaction of the Interstellar Medium with the Solar Wind, *Space Sci. Rev.*, *14*, 582–590, doi:10.1007/BF00214764.

Balogh, A., E. J. Smith, B. T. Tsurutani, D. J. Southwood, R. J. Forsyth, and T. S. Horbury (1995), The Heliospheric Magnetic Field Over the South Polar Region of the Sun, *Science*, *268*, 1007–1010.

Balsiger, H., et al. (2007), Rosina – Rosetta Orbiter Spectrometer for Ion and Neutral Analysis, *Space Sci. Rev.*, *128*, 745–801, doi:10.1007/s11214-006-8335-3.

Barnes, C. W., and J. A. Simpson (1976), Evidence for interplanetary acceleration of nucleons in corotating interaction regions, *ApJ*, *210*, L91–L96.

Bürgi, A., et al. (1993), Charge exchange of low energy ions in thin carbon foils. II. Results for ions of B, C, F, Ne, Na, Si, S, Cl, Ar, K, and Fe, *Journal of Applied Physics*, *73*, 4130–4139.

Bzowski, M., and D. Ruciński (1996), Neutral solar wind evolution during solar cycle., in *American Institute of Physics Conference Series*, *American Institute of Physics Conference Series*, vol. 382, edited by D. Winterhalter, J. T. Gosling, S. R. Habbal, W. S. Kurth, and M. Neugebauer, pp. 650–653.

Carlson, C. W., D. W. Curtis, G. Paschmann, and W. Michel (1982), An instrument for rapidly measuring plasma distribution functions with high resolution, *Advances in Space Research*, *2*, 67–70, doi:10.1016/0273-1177(82)90151-X.

Cheng, A. F. (1986), Energetic neutral particles from Jupiter and Saturn, *J. Geophys. Res.*, *91*, 4524–4530.

Crank, J., and P. Nicolson (1947), A practical method for numerical evaluation of solutions of partial differential equations of the heat-conduction type, *P. Camb. Philos. Soc.*, *43*, 50–64.

Crooker, N. U., J. T. Gosling, and S. W. Kahler (2002), Reducing heliospheric magnetic flux from coronal mass ejections without disconnection, *J. Geophys. Res.-Space*, *107*, 1028–1032, doi:10.1029/2001JA000236.

Dahl, D. A. (2000), *SIMION 3D Version 7.0 User's Manual*, Idaho National Engineering and Environmental Laboratory, Idaho Falls, ID.

de Toma, G., C. N. Arge, and P. Riley (2005), Observed and Modeled Coronal Holes, in *Solar Wind 11/SOHO 16, Connecting Sun and Heliosphere*, *ESA Special Publication*, vol. 592.

Decker, R. B., and L. Vlahos (1986), Numerical studies of particle acceleration at turbulent, oblique shocks with an application to prompt ion acceleration during solar flares, *ApJ*, *306*, 710–729, doi:10.1086/164381.

Fahr, H. J., and D. Ruciński (2002), Heliospheric pick-up ions influencing thermodynamics and dynamics of the distant solar wind, *Nonlinear Processes in Geophysics*, *9*, 377–386.

Feldman, U., E. Landi, and N. A. Schwadron (2005), On the sources of fast and slow solar wind, *J. Geophys. Res.-Space*, *110*(A9), 7109–+, doi:10.1029/2004JA010918.

Fisk, L. A. (1986), The anomalous component, its variation with latitude and related aspects of modulation, in *The Sun and the Heliosphere in Three Dimensions*, *Astrophysics and Space Science Library*, vol. 123, edited by R. G. Marsden, pp. 401–411.

Fisk, L. A. (1996), Motion of the footpoints of heliospheric magnetic field lines at the Sun: Implications for recurrent energetic particle events at high heliographic latitudes, *J. Geophys. Res.*, *101*, 15,547–15,554, doi:10.1029/96JA01005.

Fisk, L. A. (2003), Acceleration of the solar wind as a result of the reconnection of open magnetic flux with coronal loops, *J. Geophys. Res.-Space*, *108*, 1157–+, doi:10.1029/2002JA009284.

Fisk, L. A. (2005), The Open Magnetic Flux of the Sun. I. Transport by Reconnections with Coronal Loops, *ApJ*, *626*, 563–573, doi:10.1086/429957.

Fisk, L. A., and G. Gloeckler (2006), The Common Spectrum for Accelerated Ions in the Quiet-Time Solar Wind, *ApJ*, *640*, L79–L82, doi:10.1086/503293.

Fisk, L. A., and G. Gloeckler (2007), Acceleration and Composition of Solar Wind Suprathermal Tails, *Space Sci. Rev.*, *130*, 153–160, doi:10.1007/s11214-007-9180-8.

Fisk, L. A., and M. A. Lee (1980), Shock acceleration of energetic particles in corotating interaction regions in the solar wind, *ApJ*, *237*, 620–626, doi:10.1086/157907.

Fisk, L. A., and N. A. Schwadron (2001a), Origin of the Solar Wind: Theory, *Space Sci. Rev.*, *97*, 21–33.

Fisk, L. A., and N. A. Schwadron (2001b), The Behavior of the Open Magnetic Field of the Sun, *ApJ*, *560*, 425–438, doi:10.1086/322503.

Fisk, L. A., and T. H. Zurbuchen (2006), Distribution and properties of open magnetic flux outside of coronal holes, *J. Geophys. Res.-Space*, *111*(A10), 9115–+, doi:10.1029/2005JA011575.

Fisk, L. A., B. Kozlovsky, and R. Ramaty (1974), An Interpretation of the Observed Oxygen and Nitrogen Enhancements in Low-Energy Cosmic Rays, *ApJ*, *190*, L35–L37.

Fisk, L. A., N. A. Schwadron, and T. H. Zurbuchen (1998), On the Slow Solar Wind, *Space Sci. Rev.*, *86*, 51–60, doi:10.1023/A:1005015527146.

Fisk, L. A., T. H. Zurbuchen, and N. A. Schwadron (1999), Coronal Hole Boundaries and their Interactions with Adjacent Regions, *Space Sci. Rev.*, *87*, 43–54, doi:10.1023/A:1005153730158.

Forbush, S. E. (1954), World-Wide Cosmic-Ray Variations, 1937–1952, *J. Geophys. Res.*, *59*, 525–542.

Forsyth, R. J., A. Balogh, T. S. Horbury, G. Erdoes, E. J. Smith, and M. E. Burton (1996), The heliospheric magnetic field at solar minimum: ULYSSES observations from pole to pole., *A&A*, *316*, 287–295.

Funsten, H. O., and D. J. McComas (1998), Limited Resource Plasma Analyzers: Miniaturization Concepts, in *Measurement Techniques in Space Plasmas – Particles*, edited by R. F. Pfaff, J. E. Borovsky, and D. T. Young, pp. 157–167.

Funsten, H. O., B. L. Barraclough, and D. J. McComas (1993a), Shell effects observed in exit charge state distribution of 1-30 keV atomic projectiles transiting ultrathin carbon foils, *Nuclear Instruments and Methods in Physics Research B*, *80*, 49–52, doi:10.1016/0168-583X(93)96074-M.

Funsten, H. O., D. J. McComas, and B. L. Barraclough (1993b), Ultrathin foils used for low-energy neutral atom imaging of the terrestrial magnetosphere, *Optical Engineering*, *32*, 3090–3095.

Funsten, H. O., D. M. Suszcynsky, S. M. Ritzau, and R. Korde (1997), Response of 100% internal quantum efficiency silicon photodiodes to 200 eV-40 keV electrons, *IEEE Transactions on Nuclear Science*, *44*, 2561–2565, doi:10.1109/23.650863.

Geiss, J., G. Gloeckler, and U. Mall (1994a), Origin of the O(+) pick-up ions in the hehiosphere, *A&A*, *289*, 933–936.

Geiss, J., G. Gloeckler, U. Mall, R. von Steiger, A. B. Galvin, and K. W. Ogilvie (1994b), Interstellar oxygen, nitrogen and neon in the heliosphere, *A&A*, *282*, 924–933.

Geiss, J., G. Gloeckler, L. A. Fisk, and R. von Steiger (1995a), C^+ pickup ions in the heliosphere and their origin, *J. Geophys. Res.*, *100*, 23,373–23,378, doi: 10.1029/95JA03051.

Geiss, J., G. Gloeckler, and R. von Steiger (1995b), Origin of the Solar Wind From Composition Data, *Space Sci. Rev.*, *72*, 49–60, doi:10.1007/BF00768753.

Gilbert, J. A., R. A. Lundgren, M. H. Panning, S. A. Rogacki, and T. H. Zurbuchen (2007a), New Operational Modes of Linear-Electric-Field Time of Flight Telescopes, *AGU Fall Meeting Abstracts*, pp. B1734+.

Gilbert, J. A., T. H. Zurbuchen, and L. A. Fisk (2007b), A New Technique for Mapping Open Magnetic Flux from the Solar Surface into the Heliosphere, *ApJ*, *663*, 583–591, doi:10.1086/518099.

Gloeckler, G. (1977), A versatile detector system to measure the change states, mass compositions and energy spectra of interplanetary and magnetosphere ions, *Tech. Rep. TR 77-043*, University of Maryland.

Gloeckler, G. (2003), Ubiquitous Suprathermal Tails on the Solar Wind and Pickup Ion Distributions, in *Solar Wind Ten*, *American Institute of Physics Conference Series*, vol. 679, edited by M. Velli, R. Bruno, F. Malara, and B. Bucci, pp. 583–588.

Gloeckler, G., and J. Geiss (1996), Abundance of ^{3}He in the local interstellar cloud, *Nature*, *381*, 210–212, doi:10.1038/381210a0.

Gloeckler, G., and J. Geiss (1998), Interstellar and Inner Source Pickup Ions Observed with SWICS on ULYSSES, *Space Sci. Rev.*, *86*, 127–159, doi: 10.1023/A:1005019628054.

Gloeckler, G., and J. Geiss (2001), Composition of the Local Interstellar Cloud from Observations of Interstellar Pickup Ions, in *Joint SOHO/ACE workshop "Solar and Galactic Composition"*, *American Institute of Physics Conference Series*, vol. 598, edited by R. F. Wimmer-Schweingruber, pp. 281–289.

Gloeckler, G., and D. C. Hamilton (1987), AMPTE Ion Composition Results, *Physica Scripta*, *T18*, 73–84.

Gloeckler, G., J. Geiss, H. Balsiger, L. A. Fisk, A. B. Galvin, F. M. Ipavich, K. W. Ogilvie, R. von Steiger, and B. Wilken (1993), Detection of interstellar pick-up hydrogen in the solar system, *Science*, *261*, 70–73.

Gloeckler, G., J. Geiss, E. C. Roelof, L. A. Fisk, F. M. Ipavich, K. W. Ogilvie, L. J. Lanzerotti, R. von Steiger, and B. Wilken (1994), Acceleration of interstellar pickup ions in the disturbed solar wind observed on ULYSSES, *J. Geophys. Res.*, *99*, 17,637–17,643.

Gloeckler, G., L. A. Fisk, J. Geiss, N. A. Schwadron, and T. H. Zurbuchen (2000a), Elemental composition of the inner source pickup ions, *J. Geophys. Res.*, *105*, 7459–7464, doi:10.1029/1999JA000224.

Gloeckler, G., L. A. Fisk, T. H. Zurbuchen, and N. A. Schwadron (2000b), Sources, Injection and Acceleration of Heliospheric Ion Populations, in *Acceleration and Transport of Energetic Particles Observed in the Heliosphere*, *American Institute of Physics Conference Series*, vol. 528, edited by R. A. Mewaldt, J. R. Jokipii, M. A. Lee, E. Möbius, and T. H. Zurbuchen, pp. 221–228.

Gloeckler, G., T. H. Zurbuchen, and J. Geiss (2003), Implications of the observed anticorrelation between solar wind speed and coronal electron temperature, *J. Geophys. Res.-Space*, *108*, 1158–+, doi:10.1029/2002JA009286.

Gloeckler, G., et al. (1985), The charge-energy-mass spectrometer for 0.3-300 keV/e ions on the AMPTE CCE, *IEEE Transactions on Geoscience and Remote Sensing*, *23*, 234–240.

Gloeckler, G., et al. (1992), The Solar Wind Ion Composition Spectrometer, *A&AS*, *92*, 267–289.

Gloeckler, G., et al. (1995), The Solar Wind and Suprathermal Ion Composition Investigation on the Wind Spacecraft, *Space Sci. Rev.*, *71*, 79–124, doi: 10.1007/BF00751327.

Gloeckler, G., et al. (1998a), Investigation of the composition of solar and interstellar matter using solar wind and pickup ion measurements with SWICS and SWIMS on the ACE spacecraft, *Space Sci. Rev.*, *86*, 497–539, doi:10.1023/A:1005036131689.

Gloeckler, G., et al. (1998b), Interstellar Pathfinder — A Mission to the Inner Edge of the Interstellar Medium, A proposal for a medium-class explorer in response to NASA AO 98-OSS-03.

Gloeckler, G., et al. (2001), Interstellar Pathfinder — A Mission to Explore the Inner Edge of the Interstellar Medium, A proposal for a medium-class explorer in response to NASA AO 01-OSS-03.

Gombosi, T. I. (1998), *Physics of the Space Environment*, 339 pp., Cambridge University Press, Cambridge, UK.

Gosling, J. T., J. R. Asbridge, S. J. Bame, and W. C. Feldman (1978), Effects of a long entrance aperture upon the azimuthal response of spherical section electrostatic analyzers, *Rev. Sci. Instrum.*, *49*, 1260–1268.

Gosling, J. T., J. R. Asbridge, S. J. Bame, W. C. Feldman, G. Borrini, and R. T. Hansen (1981), Coronal streamers in the solar wind at 1 AU, *J. Geophys. Res.*, *86*, 5438–5448.

Gosling, J. T., M. F. Thomsen, and R. C. Anderson (1984), *Cookbook for determining essential transmission characteristics of spherical section electrostatic analyzers*, Los Alamos National Laboratory.

Gosling, J. T., J. Birn, and M. Hesse (1995), Three-dimensional magnetic reconnection and the magnetic topology of coronal mass ejection events, *Geophys. Res. Lett.*, *22*, 869–872.

Hamilton, D. C., G. Gloeckler, F. M. Ipavich, R. A. Lundgren, R. B. Sheldon, and D. Hovestadt (1990), New high-resolution electrostatic ion mass analyzer using time of flight, *Rev. Sci. Instrum.*, *61*, 3104–3106.

Hill, A. G., W. W. Buechner, J. S. Clark, and J. B. Fisk (1939), The Emission of Secondary Electrons Under High Energy Positive Ion Bombardment, *Physical Review*, *55*, 463–470, doi:10.1103/PhysRev.55.463.

Hoeksema, J. T., and S. T. Suess (1990), The outer magnetic field, *Mem. Soc. Astron. Italiana*, *61*, 485–498.

Holzer, T. E. (1989), Interaction between the solar wind and the interstellar medium, *ARA&A*, *27*, 199–234, doi:10.1146/annurev.aa.27.090189.001215.

Holzer, T. E., and E. Leer (1973), Solar Wind Heating Beyond 1 AU, *Ap&SS*, *24*, 335–347, doi:10.1007/BF02637160.

Hörandel, J. R. (2008), Cosmic-ray composition and its relation to shock acceleration by supernova remnants, *Advances in Space Research*, *41*, 442–463, doi: 10.1016/j.asr.2007.06.008.

Hovestadt, D., et al. (1995), CELIAS - Charge, Element and Isotope Analysis System for SOHO, *Sol. Phys.*, *162*, 441–481, doi:10.1007/BF00733436.

Hundhausen, A. J., H. E. Gilbert, and S. J. Bame (1968), Ionization State of the Interplanetary Plasma, *J. Geophys. Res.*, *73*, 5485–5493.

Hurford, G. J., R. A. Mewaldt, E. C. Stone, and R. E. Vogt (1975), Enrichment of heavy nuclei in He-3-rich flares, *ApJ*, *201*, L95–L97.

Ipavich, F. M., A. B. Galvin, G. Gloeckler, D. Hovestadt, B. Klecker, and M. Scholer (1986), Comet Giacobini-Zinner - In situ observations of energetic heavy ions, *Science*, *232*, 366–369.

Ipavich, F. M., et al. (1998), Solar wind measurements with SOHO: The CELIAS/MTOF proton monitor, *J. Geophys. Res.*, *103*, 17,205–17,214, doi: 10.1029/97JA02770.

Isenberg, P. A. (1986), Interaction of the solar wind with interstellar neutral hydrogen - Three-fluid model, *J. Geophys. Res.*, *91*, 9965–9972.

Jackson, B. V., and R. A. Howard (1993), A CME Mass Distribution Derived from SOLWIND Coronagraph Observations, *Sol. Phys.*, *148*, 359–370, doi: 10.1007/BF00645095.

Jackson, J. D. (1999), *Classical Electrodynamics*, 3rd ed., 808 pp., John Wiley & Sons, United States of America.

Kahler, S. W., D. V. Reames, and N. R. Sheeley, Jr. (2001), Coronal Mass Ejections Associated with Impulsive Solar Energetic Particle Events, *ApJ*, *562*, 558–565, doi: 10.1086/323847.

Kallenbach, R., J. Geiss, G. Gloeckler, and R. von Steiger (2000), Pick-up Ion Measurements in the Heliosphere - A Review, *Ap&SS*, *274*, 97–114.

Klecker, B., E. Möbius, and M. A. Popecki (2006), Solar Energetic Particle Charge States: An Overview, *Space Sci. Rev.*, *124*, 289–301, doi:10.1007/s11214-006-9111-0.

Koehn, P. L., T. H. Zurbuchen, G. Gloeckler, R. A. Lundgren, and L. A. Fisk (2002), Measuring the plasma environment at Mercury: The fast imaging plasma spectrometer, *Meteoritics and Planetary Science*, *37*, 1173–1189.

Kóta, J., and J. R. Jokipii (1998), Modeling of 3-D Corotating Cosmic-Ray Structures in the Heliosphere, *Space Sci. Rev.*, *83*, 137–145.

Krimigis, S. M., et al. (2004), Magnetosphere Imaging Instrument (MIMI) on the Cassini Mission to Saturn/Titan, *Space Sci. Rev.*, *114*, 233–329, doi: 10.1007/s11214-004-1410-8.

Levine, R. H., M. D. Altschuler, and J. W. Harvey (1977), Solar sources of the interplanetary magnetic field and solar wind, *J. Geophys. Res.*, *82*, 1061–1065.

Liewer, P. C., M. Neugebauer, and T. Zurbuchen (2004), Characteristics of active-region sources of solar wind near solar maximum, *Sol. Phys.*, *223*, 209–229, doi: 10.1007/s11207-004-1105-z.

Lionello, R., P. Riley, J. A. Linker, and Z. Mikić (2005), The Effects of Differential Rotation on the Magnetic Structure of the Solar Corona: Magnetohydrodynamic Simulations, *ApJ*, *625*, 463–473, doi:10.1086/429268.

Luhmann, J. G., Y. Li, C. N. Arge, P. R. Gazis, and R. Ulrich (2002), Solar cycle changes in coronal holes and space weather cycles, *J. Geophys. Res.-Space*, *107*, 1154–+, doi:10.1029/2001JA007550.

Luhn, A., B. Klecker, D. Hovestadt, M. Scholer, G. Gloeckler, F. M. Ipavich, C. Y. Fan, and L. A. Fisk (1984), Ionic charge states of N, Ne, Mg, SI and S in solar energetic particle events, *Advances in Space Research*, *4*, 161–164, doi:10.1016/0273-1177(84)90307-7.

Managadze, G. G. (1986), Time-of-Flight Ion Mass Analyzer, US Patent 4,611,118.

Manchester, W. B., T. I. Gombosi, I. Roussev, A. Ridley, D. L. De Zeeuw, I. V. Sokolov, K. G. Powell, and G. Tóth (2004), Modeling a space weather event from the Sun to the Earth: CME generation and interplanetary propagation, *J. Geophys. Res.-Space*, *109*(A18), 2107–+, doi:10.1029/2003JA010150.

McComas, D. J., and J. E. Nordholt (1990), New approach to 3-D, high sensitivity, high mass resolution space plasma composition measurements, *Rev. Sci. Instrum.*, *61*, 3095–3097.

McComas, D. J., J. E. Nordholt, J.-J. Berthelier, J.-M. Illiano, and D. T. Young (1998), The Cassini Ion Mass Spectrometer, in *Measurement Techniques in Space Plasmas – Particles*, edited by R. F. Pfaff, J. E. Borovsky, and D. T. Young, pp. 187–193.

McComas, D. J., et al. (2000), Solar wind observations over Ulysses' first full polar orbit, *J. Geophys. Res.*, *105*, 10,419–10,434, doi:10.1029/1999JA000383.

McComas, D. J., et al. (2003), Interstellar Pathfinder - A Mission to the Inner Edge of the Interstellar Medium, in *Solar Wind Ten*, *American Institute of Physics Conference Series*, vol. 679, edited by M. Velli, R. Bruno, F. Malara, and B. Bucci, pp. 834–837.

Mewaldt, R. A., J. D. Spalding, and E. C. Stone (1984), The isotopic composition of the anomalous low-energy cosmic rays, *ApJ*, *283*, 450–456, doi:10.1086/162324.

Mewaldt, R. A., et al. (2007), On the Differences in Composition between Solar Energetic Particles and Solar Wind, *Space Sci. Rev.*, *130*, 207–219, doi:10.1007/s11214-007-9187-1.

Möbius, E., D. Hovestadt, B. Klecker, M. Scholer, and G. Gloeckler (1985), Direct observation of He(+) pick-up ions of interstellar origin in the solar wind, *Nature*, *318*, 426–429.

Möbius, E., P. Bochsler, A. G. Ghielmetti, and D. C. Hamilton (1990), High mass resolution isochronous time-of-flight spectrograph for three-dimensional space plasma measurements, *Rev. Sci. Instrum.*, *61*, 3609–3612.

Möbius, E., et al. (1998), The Solar Energetic Particle Ionic Charge Analyzer (SEPICA) and the Data Processing Unit (S3DPU) for SWICS, SWIMS and SEPICA, *Space Sci. Rev.*, *86*, 449–495, doi:10.1023/A:1005084014850.

Möbius, E., et al. (1999), Direct evidence of the interstellar gas flow velocity in the pickup ion cut-off as observed with SOHO CELIAS CTOF, *Geophys. Res. Lett.*, *26*, 3181–3184, doi:10.1029/1999GL003644.

Mukherjee, P., M.-G. Kang, T. H. Zurbuchen, L. J. Guo, and F. A. Herrero (2007), Fabrication of high aspect ratio Si nanogratings with smooth sidewalls for a deep UV-blocking particle filter, *Journal of Vacuum Science & Technology B: Microelectronics and Nanometer Structures*, *25*, 2645–2648, doi:10.1116/1.2804612.

Neugebauer, M., B. E. Goldstein, R. Goldstein, A. J. Lazarus, K. Altwegg, and H. Balsiger (1987), The pick-up of cometary protons by the solar wind, *A&A*, *187*, 21–24.

Neugebauer, M., P. C. Liewer, E. J. Smith, R. M. Skoug, and T. H. Zurbuchen (2002), Sources of the solar wind at solar activity maximum, *J. Geophys. Res.-Space*, *107*, 1488–+, doi:10.1029/2001JA000306.

Nordholt, J. E., et al. (2003), Deep Space 1 encounter with Comet 19P/Borrelly: Ion composition measurements by the PEPE mass spectrometer, *Geophys. Res. Lett.*, *30*(9), 090,000–1, doi:10.1029/2002GL016840.

Parker, E. (1959), Extension of the Solar Corona into Interplanetary Space, *J. Geophys. Res.*, *64*, 1675–1681.

Parker, E. N. (1958), Dynamics of the Interplanetary Gas and Magnetic Fields., *ApJ*, *128*, 664–676.

Pesses, M. E., D. Eichler, and J. R. Jokippi (1981), Cosmic ray drift, shock wave acceleration, and the anomalous component of cosmic rays, *ApJ*, *246*, L85–L88, doi:10.1086/183559.

Pizzo, V. (1978), A three-dimensional model of corotating streams in the solar wind. I - Theoretical foundations, *J. Geophys. Res.*, *83*, 5563–5572.

Poduval, B., and X. P. Zhao (2004), Discrepancies in the prediction of solar wind using potential field source surface model: An investigation of possible sources, *J. Geophys. Res.-Space*, *109*(A18), 8102–+, doi:10.1029/2004JA010384.

Reames, D. V. (1999), Particle acceleration at the Sun and in the heliosphere, *Space Sci. Rev.*, *90*, 413–491, doi:10.1023/A:1005105831781.

Riley, P. (2007), Modeling corotating interaction regions: From the Sun to 1 AU, *J. Atmos. Sol-Terr. Phy.*, *69*, 32–42, doi:10.1016/j.jastp.2006.06.008.

Riley, P., J. A. Linker, Z. Mikić, R. Lionello, S. A. Ledvina, and J. G. Luhmann (2006), A Comparison between Global Solar Magnetohydrodynamic and Potential Field Source Surface Model Results, *ApJ*, *653*, 1510–1516, doi:10.1086/508565.

Ritzau, S. M., and R. A. Baragiola (1998), Electron emission from carbon foils induced by keV ions, *Phys. Rev. B*, *58*, 2529–2538, doi:10.1103/PhysRevB.58.2529.

Rogacki, S. A. (2007), A New Approach to Systems Integration of Time-of-Flight Instruments, Final report for NRA 03-OSS-01 PIDDP.

Roussev, I. I., T. I. Gombosi, I. V. Sokolov, M. Velli, W. Manchester, IV, D. L. DeZeeuw, P. Liewer, G. Tóth, and J. Luhmann (2003), A Three-dimensional Model of the Solar Wind Incorporating Solar Magnetogram Observations, *ApJ*, *595*, L57–L61, doi:10.1086/378878.

Schatten, K. H. (1971), Current sheet magnetic model for the solar corona., *Cosmic Electrodyn.*, *2*, 232–245.

Schatten, K. H., J. M. Wilcox, and N. F. Ness (1969), A model of interplanetary and coronal magnetic fields, *Sol. Phys.*, *6*, 442–455, doi:10.1007/BF00146478.

Schrijver, C. J., A. M. Title, K. L. Harvey, N. R. Sheeley, Jr., Y. M. Wang, G. H. J. van den Oord, R. A. D. Shine, T. Tarbell, and N. E. Hurlburt (1998), Large-scale coronal heating by the small-scale magnetic field of the Sun, *Nature*, *394*, 152–154.

Schulz, M., E. N. Frazier, and D. J. Boucher, Jr. (1978), Coronal magnetic-field model with non-spherical source surface, *Sol. Phys.*, *60*, 83–104.

Schunk, R. W., and A. F. Nagy (2000), *Ionospheres*, 570 pp., Cambridge University Press, Cambridge, UK.

Schwadron, N. A., and G. Gloeckler (2007), Pickup Ions and Cosmic Rays from Dust in the Heliosphere, *Space Sci. Rev.*, *130*, 283–291, doi:10.1007/s11214-007-9166-6.

Scime, E. E., D. J. McComas, E. H. Anderson, and M. L. Schattenburg (1995), Extreme-ultraviolet polarization and filtering with gold transmission gratings, *Appl. Opt.*, *34*, 648–654.

Shellard, R. C. (2001), Cosmic Accelerators and Terrestrial Detectors, *Brazilian Journal of Physics*, *31*(2), 247–254.

Siegmund, O. H. W., J. V. Vallerga, and A. S. Tremsin (2003), Advances in MCP Sensors for UV/Visible Astronomy, in *Hubble's Science Legacy: Future Optical/Ultraviolet Astronomy from Space*, *Astronomical Society of the Pacific Conference Series*, vol. 291, edited by K. R. Sembach, J. C. Blades, G. D. Illingworth, and R. C. Kennicutt, Jr., pp. 403–406.

Sittler, E. C., et al. (2006), Cassini observations of Saturn's inner plasmasphere: Saturn orbit insertion results, *Planet. Space Sci.*, *54*, 1197–1210, doi:10.1016/j.pss.2006.05.038.

Smith, E. J., and A. Balogh (1995), Ulysses observations of the radial magnetic field, *Geophys. Res. Lett.*, *22*, 3317–3320, doi:10.1029/95GL02826.

Sternglass, E. J. (1957), Theory of Secondary Electron Emission by High-Speed Ions, *Physical Review*, *108*, 1–12, doi:10.1103/PhysRev.108.1.

Stone, E. C., A. M. Frandsen, R. A. Mewaldt, E. R. Christian, D. Margolies, J. F. Ormes, and F. Snow (1998), The Advanced Composition Explorer, *Space Sci. Rev.*, *86*, 1–22, doi:10.1023/A:1005082526237.

Stone, E. C., A. C. Cummings, F. B. McDonald, B. C. Heikkila, N. Lal, and W. R. Webber (2005), Voyager 1 Explores the Termination Shock Region and the Heliosheath Beyond, *Science*, *309*, 2017–2020, doi:10.1126/science.1117684.

Suess, S. T., and E. J. Smith (1996), Latitudinal dependence of the radial IMF component: Coronal imprint, *Geophys. Res. Lett.*, *23*, 3267–3270, doi:10.1029/96GL02908.

Suess, S. T., E. J. Smith, J. Phillips, B. E. Goldstein, and S. Nerney (1996), Latitudinal dependence of the radial IMF component - interplanetary imprint., *A&A*, *316*, 304–312.

Suess, S. T., A.-H. Wang, S. T. Wu, G. Poletto, and D. J. McComas (1999), A two-fluid, MHD coronal model, *J. Geophys. Res.*, *104*, 4697–4708, doi:10.1029/1998JA900086.

Tan, C., and Y. Yan (2008), Source investigation of impulsive ^{3}He-rich particle events, *Advances in Space Research*, *41*, 992–997, doi:10.1016/j.asr.2007.05.077.

Thomas, G. E. (1978), The interstellar wind and its influence on the interplanetary environment, *Annual Review of Earth and Planetary Sciences*, *6*, 173–204, doi:10.1146/annurev.ea.06.050178.001133.

Tremsin, A. S., D. S. Hussey, R. G. Downing, W. B. Feller, D. F. R. Mildner, D. L. Jacobson, M. Arif, and O. H. W. Siegmund (2007), Neutron Collimation With Microchannel Plates: Calibration of Existing Technology and Near

Future Possibilities, *IEEE Transactions on Nuclear Science*, *54*, 362–366, doi: 10.1109/TNS.2007.891080.

Vasyliunas, V. M., and G. L. Siscoe (1976), On the flux and the energy spectrum of interstellar ions in the solar system, *J. Geophys. Res.*, *81*, 1247–1252.

von Steiger, R., and J. Geiss (1993), Solar wind composition and expectations for high solar latitudes, *Advances in Space Research*, *13*, 63–74, doi:10.1016/0273-1177(93)90392-O.

von Steiger, R., J. Geiss, G. Gloeckler, and A. B. Galvin (1995), Kinetic Properties of Heavy Ions in the Solar Wind From SWICS/Ulysses, *Space Sci. Rev.*, *72*, 71–76, doi:10.1007/BF00768756.

von Steiger, R., N. A. Schwadron, L. A. Fisk, J. Geiss, G. Gloeckler, S. Hefti, B. Wilken, R. F. Wimmer-Schweingruber, and T. H. Zurbuchen (2000), Composition of quasi-stationary solar wind flows from Ulysses/Solar Wind Ion Composition Spectrometer, *J. Geophys. Res.*, *105*, 27,217–27,238, doi:10.1029/1999JA000358.

Wang, Y.-M., and N. R. Sheeley, Jr. (1990), Solar wind speed and coronal flux-tube expansion, *ApJ*, *355*, 726–732, doi:10.1086/168805.

Wang, Y.-M., and N. R. Sheeley, Jr. (1992), On potential field models of the solar corona, *ApJ*, *392*, 310–319, doi:10.1086/171430.

Wang, Y.-M., and N. R. Sheeley, Jr. (1995), Solar Implications of ULYSSES Interplanetary Field Measurements, *ApJ*, *447*, L143+, doi:10.1086/309578.

Wang, Y.-M., J. Lean, and N. R. Sheeley, Jr. (2000), The long-term variation of the Sun's open magnetic flux, *Geophys. Res. Lett.*, *27*, 505–508.

Whang, Y. C., Y.-M. Wang, N. R. Sheeley, and L. F. Burlaga (2005), Global structure of the out-of-ecliptic solar wind, *J. Geophys. Res.-Space*, *110*(A9), 3103–+, doi: 10.1029/2004JA010875.

Wimmer-Schweingruber, R. F. (2003), Solar Wind Composition, in *Solar Wind Ten*, *American Institute of Physics Conference Series*, vol. 679, edited by M. Velli, R. Bruno, F. Malara, and B. Bucci, pp. 577–582.

Wimmer-Schweingruber, R. F., and P. Bochsler (2003), On the origin of inner-source pickup ions, *Geophys. Res. Lett.*, *30*, 49–1.

Woo, R., S. R. Habbal, and U. Feldman (2004), Role of Closed Magnetic Fields in Solar Wind Flow, *ApJ*, *612*, 1171–1174, doi:10.1086/422799.

Wüest, M. (1998), Time-of-Flight Ion Composition Measurement Technique for Space Plasmas, in *Measurement Techniques in Space Plasmas – Particles*, edited by R. F. Pfaff, J. E. Borovsky, and D. T. Young, pp. 141–155.

Yokota, S., Y. Saito, K. Asamura, and T. Mukai (2005), Development of an ion energy mass spectrometer for application on board three-axis stabilized spacecraft, *Rev. Sci. Instrum.*, *76*, 4501–+, doi:10.1063/1.1834697.

Young, D. T., S. J. Bame, M. F. Thomsen, R. H. Martin, J. L. Burch, J. A. Marshall, and B. Reinhard (1988), 2π-radian field-of-view toroidal electrostatic analyzer, *Rev. Sci. Instrum.*, *59*, 743–751.

Young, D. T., et al. (2004a), Solar wind interactions with Comet 19P/Borrelly, *Icarus*, *167*, 80–88, doi:10.1016/S0019-1035(03)00281-1.

Young, D. T., et al. (2004b), Cassini Plasma Spectrometer Investigation, *Space Sci. Rev.*, *114*, 1–112, doi:10.1007/s11214-004-1406-4.

Young, D. T., et al. (2007), Plasma Experiment for Planetary Exploration (PEPE), *Space Sci. Rev.*, *129*, 327–357, doi:10.1007/s11214-007-9177-3.

Zhao, L., and T. H. Zurbuchen (2008), On the Global Distribution of Slow Solar Wind, *ApJ*.

Zhao, X., and J. T. Hoeksema (1994), A coronal magnetic field model with horizontal volume and sheet currents, *Sol. Phys.*, *151*, 91–105.

Zhao, X., and J. T. Hoeksema (1995), Prediction of the interplanetary magnetic field strength, *J. Geophys. Res.*, *100*, 19–33.

Zurbuchen, T. H. (2007), A New View of the Coupling of the Sun and the Heliosphere, *ARA&A*, *45*, 297–338, doi:10.1146/annurev.astro.45.010807.154030.

Zurbuchen, T. H., S. Hefti, L. A. Fisk, G. Gloeckler, and N. A. Schwadron (2000), Magnetic structure of the slow solar wind: Constraints from composition data, *J. Geophys. Res.*, *105*, 18,327–18,336, doi:10.1029/1999JA000427.

Zurbuchen, T. H., et al. (2003), Particle Acceleration in the Turbulent Heliosphere, A proposal to NASA in response to AO 03-OSS-02.